

# Low Temperature Anomalies in Partially Disordered Lateral Spin Valves



Jack Adams

University of Leeds

School of Physics and Astronomy

Submitted in accordance with the requirements for the degree of

*Doctor of Philosophy*

June, 2023

## **Intellectual Property Statement**

The candidate confirms that the work submitted is his own and that appropriate credit has been given where reference has been made to the work of others.

This copy has been supplied on the understanding that it is copyright material and that no quotation from the thesis may be published without proper acknowledgement.

The right of Jack Adams to be identified as Author of this work has been asserted by him in accordance with the Copyright, Designs and Patents Act 1988.

© 2023 The University of Leeds and Jack Adams.

## Acknowledgements

Firstly I would like to thank Paul Mans for providing the funding, without which this project would have been impossible to begin with. I would also like to thank my supervisor Bryan Hickey, for putting up with my regular disappointment at the struggles of experimental physics and for maintaining a constant sense of optimism and enthusiasm towards the research we were conducting.

I would like to thank Georgios Stefanou for teaching me everything I know about lateral spin valves and metal deposition. You were the perfect mentor for someone who was out of their depth. My thanks also goes to Mark Rosamond for performing all of the lithography performed in this project, without whom, the nanoscopic effects observed in this study would have never occurred.

Special thanks go to Leigh Harris, who saved my bacon more times than I can count. Your ability to counteract my talent for breaking things is second to none. Likewise, thank you to Richard Oliver for repeatedly magicking up solutions to my multitude of electrical problems in the lab. Also David Chapman and Adam Foster, thank you for enabling my never ending need for liquid helium, the fact that any measurements were obtained at all are down to both of you.

Thank you dad, for helping me to edit this thesis into something somewhat legible. Kathryn Moran, thank you for keeping me sane. I probably would have given up if you hadn't re-emerged and provided endless support in the final year. Daniel Roe, you made a great a fire marshal.

Lastly and most importantly – Mannan Ali, thank you for everything. This project really would have gone nowhere if you hadn't shown up and saved the day. How you found the time to repeatedly fix all of my problems, I'll never know.

## Abstract

Two sets of lateral spin valves (LSVs) were fabricated – Permalloy (Py)/ Silver (Ag) and Py/ Copper (Cu). Both sets of devices were made with 99.9999 % (six 9s) pure metal, evaporated at a rate that would optimise their crystal structure. However, the deposition of the non-magnetic material in both sets was paused midway, for 25 minutes, before the growth was completed. This was done in order to purposefully introduce ambient impurities from the deposition chamber (such as N<sub>2</sub>) into the central channel of the devices and, as such, act to disrupt the quality of the crystal structure. Both ‘local’ and ‘non-local’ direct current (DC) reversal sweeps ( $\pm 500 \mu\text{A}$ ) were performed at a range of temperatures (3 K up to 290 K) and applied magnetic field strengths ( $\pm 100 \text{ mT}$ ), for devices with a variety of injector-detector separations (550 nm to 2650 nm) in order to extract their thermal, electrical and spintronic properties. A model recently presented by Stefanou et al. [1] was applied to the thermal voltages measured in both sets of devices resulting in a detailed insight to the thermal differences between Cu and Ag nanowires. It was found that Cu’s relatively larger thermal conductivity resulted in a completely different temperature dependence for thermal voltages measured at temperatures below 50 K. The length dependence of the spin signals in both sets of devices were extracted and fitted with a Valet-Fert model for spin diffusion. Careful analysis showed no correlation between the presence of a characteristic Kondo ‘upturn’ in the resistivity measurements and the magnitude of a low temperature ‘downturn’ in the spin diffusion lengths for both the Ag and Cu. The introduction of non-magnetic impurities during deposition and hence the disruption of the crystal structure, appears to have significantly reduced the applicability of the Elliott-Yafet (EY) model for spin-flip scattering when compared to similar devices [2–4]. Additionally, a low temperature deviation from the usual quadratic, non-local, current-voltage relationship (NLIV), was shown to be very strongly correlated to the magnitude of thermal voltages, caused by Joule heating in the devices’ injectors, measured at their detectors [4–6].

# CONTENTS

|          |  |           |
|----------|--|-----------|
| <b>1</b> | <b>Introduction</b>                                | <b>1</b>  |
| <b>2</b> | <b>Background and Theory</b>                       | <b>4</b>  |
| 2.1      | Spin . . . . .                                     | 5         |
| 2.1.1    | Diamagnetism . . . . .                             | 5         |
| 2.1.2    | Paramagnetism . . . . .                            | 6         |
| 2.1.3    | Ferromagnetism . . . . .                           | 7         |
| 2.2      | Electron Transport . . . . .                       | 9         |
| 2.2.1    | Band Theory of Solids . . . . .                    | 10        |
| 2.2.2    | Conductivity . . . . .                             | 12        |
| 2.2.3    | Scattering . . . . .                               | 13        |
| 2.3      | Spin Transport . . . . .                           | 15        |
| 2.3.1    | Spin Dependent Scattering . . . . .                | 15        |
| 2.3.2    | Spin Injection . . . . .                           | 19        |
| 2.3.3    | Spin Diffusion . . . . .                           | 20        |
| 2.3.4    | Ferromagnetic/Non-Magnetic Interfaces . . . . .    | 22        |
| 2.3.5    | Pure Spin Currents and Non-Local Devices . . . . . | 24        |
| 2.3.6    | Spin-flip Scattering . . . . .                     | 29        |
| 2.4      | Thermoelectric Effect . . . . .                    | 31        |
| 2.4.1    | Joule Heating . . . . .                            | 31        |
| 2.4.2    | Peltier Effect . . . . .                           | 33        |
| 2.4.3    | Seebeck Effect . . . . .                           | 33        |
| <b>3</b> | <b>Methods</b>                                     | <b>37</b> |
| 3.1      | Sample Fabrication . . . . .                       | 38        |

|          |   |            |
|----------|---|------------|
| 3.1.1    | Substrate Preparation . . . . .                     | 39         |
| 3.1.2    | e-Beam Lithography . . . . .                        | 39         |
| 3.1.3    | Electrical Contacts . . . . .                       | 41         |
| 3.1.4    | Shadow Deposition . . . . .                         | 46         |
| 3.2      | Electrical Measurements . . . . .                   | 47         |
| 3.2.1    | Setup . . . . .                                     | 47         |
| 3.2.2    | Local Measurements . . . . .                        | 52         |
| 3.2.3    | Non-Local Measurements . . . . .                    | 54         |
| 3.3      | Sample Characterisation . . . . .                   | 55         |
| <b>4</b> | <b>Thermal Signals In Non-local IVs</b>             | <b>56</b>  |
| 4.1      | Non-Local IVs . . . . .                             | 57         |
| 4.2      | Spin Signal . . . . .                               | 60         |
| 4.3      | Quadratic Term . . . . .                            | 64         |
| 4.4      | Baseline Resistance . . . . .                       | 67         |
| 4.5      | Thermal Diffusion . . . . .                         | 68         |
| 4.6      | Thermal Conductance . . . . .                       | 73         |
| 4.7      | Conclusions . . . . .                               | 78         |
| <b>5</b> | <b>Spin-Flip Scattering in ‘Dirty’ Noble Metals</b> | <b>81</b>  |
| 5.1      | A Literature Review . . . . .                       | 82         |
| 5.2      | Non-Magnetic Impurities In Py/Ag LSVs . . . . .     | 85         |
| 5.3      | Non-Magnetic Impurities In Py/Cu LSVs . . . . .     | 93         |
| 5.4      | Conclusions . . . . .                               | 98         |
| <b>6</b> | <b>Novel Deviations to Low Temperature DC NLIVs</b> | <b>102</b> |
| 6.1      | Gaussian Peaks Centred At Zero Current . . . . .    | 103        |
| 6.2      | Measurement Artefacts . . . . .                     | 109        |
| 6.3      | Non-Equilibrium Heating . . . . .                   | 112        |
| 6.4      | Conclusions . . . . .                               | 114        |
| <b>7</b> | <b>Final Conclusions</b>                            | <b>118</b> |
| 7.1      | Outlook . . . . .                                   | 121        |
|          | <b>References</b>                                   | <b>123</b> |

# LIST OF FIGURES

- 2.1 (a) The distribution of energy ( $E$ ) for electrons in a paramagnet at a temperature of absolute zero, with the x-axis showing the number of allowed states at each possible energy, per unit volume (called the density of states) -  $g(E)$ . The electrons have been shown separately for the two different spin alignments (red for up spins and blue for down spins) and all possible states below the Fermi energy ( $E_F$ ) are filled. (b) The response to an applied magnetic field ( $B$ ) that is pointed upwards in the  $z$  direction. The electrons that have spins parallel to the magnetisation have their energy reduced by an amount equal to  $\mu_B B$ , while the opposite is true for the anti-parallel spins. The spins of electrons above  $E_F$  (represented by the dashed blue lines) will flip direction so as to occupy the available lower energy states (represented by the dashed red lines) with the opposite spin. As a result, the populations of each spin direction will no longer be equal in number and the material becomes magnetic. . . . 8

2.2 The distribution of electrons and their energies for 3 different types of solid at absolute zero: **(a)** shows the band structure for a metal;  $E_F$  lies within one of the energy bands which means that electrons can very easily move into higher energy states. As a result, when an electrical field ( $\vec{E}$ ) is applied, electrons will gain kinetic energy and begin to move with the field. **(b)** on the other hand, shows a semiconductor. Here,  $E_F$  lies within a band gap meaning that electrons cannot easily be given more energy. A semiconductor will conduct when a large  $\vec{E}$  is applied or at very high temperatures. **(c)** shows the structure for an insulator. Here, the band gap is very large because of properties within the crystal structure and so it is almost impossible to give electrons enough energy to conduct freely. . . . . 11

2.3 A more realistic band diagram of the density of states for two metals. **(a)** shows Ag, which is a paramagnet, after a magnetic field pointing upwards along the z-axis has been applied. The energies of the bands have both shifted by  $\mu_B B$  and the populations of spins have adjusted accordingly.  $E_F$  lies in the very narrow part of the structure (called the s-band) for both spin directions, which has a very high conductivity due to its low  $g(E)$ . **(b)** shows Ni, a ferromagnet, after spontaneous magnetisation in the up direction. The up spins'  $E_F$  has shifted and lies in the highly conductive s-band. For the down spins, on the other hand,  $E_F$  has shifted into the more densely populated part of the structure (called the d-band) where the conductivity is much lower because of the high  $g(E)$  as well as the large number of empty states that can be occupied just above  $E_F$ . . . . . 17

2.4 A diagram of a spin valve structure, where the blue and red layers represent the ferromagnets while the grey layer is a non-magnetic, conductive spacer. The golden panels are electrical contacts. Underneath is a simple resistor schematic for each scenario, with the spin-dependent currents split into parallel current paths. **(a)** shows the device in its parallel state: up spin electrons will experience less scattering than down spins in both magnetic layers and, as such, will flow more readily through the device. **(b)** shows the anti-parallel alignment: here the up spins will experience more scattering in the 2nd magnetic layer while the down spin electrons experience more scattering in the 1st – thus resulting in an overall equal current for both spins. It should be noted that in reality the layers of the spin valve are instead arranged vertically due to the nature of the device fabrication. . . . . 18

2.5 An energy diagram of the solutions for a ferromagnet/non-magnet interface undergoing spin injection along the x-axis. The dashed black line shows the spin averaged  $\mu$ , which is sloped because of the application of  $\tilde{E}$ . At distances far from the interface, the spin-dependent  $\mu$  are equal but they separate at the interface because of the imbalanced spin-dependent  $\sigma$ . The length over which the imbalance in spins protrudes into the two materials is based on their respective  $l_{sf}$ . There is a discontinuity in  $\mu$  at the interface despite the fact that each spin sub-band is continuous. . . . . 25

|     |   |    |
|-----|---|----|
| 2.6 | A scanning electron microscope (SEM) image of an LSV. The ferromagnetic injector can be seen as a thin strip beneath the thicker (and lighter in colour) non-magnetic material on the left. Meanwhile the ferromagnetic detector, with its large nucleation pad, can be seen beneath the right hand side. The non-magnetic channel connects the two ferromagnetic electrodes with a separation of 200 nm. In order to produce a pure spin current, a charge current must be passed from the injector into the spanning nanowire (indicated by the white arrow). Spin accumulation at the injection interface leads to the propagation of a pure spin current along the device (red and blue arrows). The detector allows for the spin accumulation to be measured as a potential difference, non-locally to the injected current. The devices can be fabricated with the detector positioned at different distances along the non-magnetic channel, which will result in smaller potentials analogous to a stylophone where, by moving the stlyus to different points along the current path, different pitched noises can be made. . . . . | 26 |
| 2.7 | The energy diagram for an LSV. On the left hand side, the spin injection from the injector (FM1) is shown as it was in Fig.2.5. However, in this diagram the part of the non-magnet (NM) that is shown instead, is the central bridge – void of the injection charge current; therefore, $\mu$ is flat. The spin accumulation at $x = 0$ diffuses throughout the non-magnet and its polarisation decays exponentially with distance because of spin-flip scattering. At the detector (FM2), positioned L distance away, two scenarios are shown: when FM1 and FM2 are magnetised parallel to each other, the spin-dependent potentials are shown by solid lines; for the anti-parallel alignment, on the other hand, the potentials are represented by dashed lines. In the parallel state, a positive $\mu_P$ is formed with respect to the non-magnet, while the anti-parallel state results in a respectively negative $\mu_{AP}$ . . . . .  | 28 |
| 2.8 | A simple schematic of an LSV with the non-magnetic channel (lighter grey) bridging the gap between two ferromagnetic electrodes (darker grey). The dimensions of each of the components have been marked. . .   | 29 |

- 3.1 A simple schematic of the process of e-beam lithography and then deposition onto a bi-layer of resists. **(a)** The bottom dark blue layer is the SiO<sub>2</sub> surface, above which are the two different layers of resists stacked on top of each other. The black arrow represents exposure to the focused e-beam. **(b)** The resist is immersed in a ‘developer’, a solvent that only acts on resist with weakened bonds. A larger volume of the bottom layer of resist is dissolved because it is more sensitive to the e-beam. **(c)** The patterned bi-layer is then exposed to the evaporation of a desired material. The undercut in the bilayer results in a ‘shadow’ from the depositing material. **(d)** Afterwards, the metal (dark grey here) will have coated the top of the template, as well as depositing into the exposed area. There is often also material lining the side of channels cut into the resist – referred to as ‘sidewall deposition’. **(e)** The template is then removed by exposing it to a strong solvent. The material on top will be removed along with it, leaving behind only the desired pattern of metal. . . . . 40
- 3.2 An SEM image of a fully fabricated LSV. The non-magnetic material shows up as the lightest coloured wires in the image. The Au inner contacts are the wider features positioned beneath each of the device’s four ends. The separation between the injector and detector has been marked. The inset shows a closer, angled inspection of one of the arms overlapping the thinner Au inner contact - including the width of the contact’s end. . . . . 43
- 3.3 An SEM image of an array of four LSVs, each device with four contacts. The inner contacts form the narrow ends which converge at the devices while the outer contacts can be seen overlapping them further out. One of the points of overlap has been highlighted in yellow in the bottom left to give a better sense of the contact area. The large crosses seen at the left and right-hand sides of the image are guide marks for the JEOL to align to. On the bottom right device, it can be seen that a large flake of material has landed on top – rendering it immeasurable. This is just one of the many pitfalls that arises during fabrication. . . . . 44

3.4 A crude sketch of the bespoke deposition chamber used to perform the shadow deposition required to fabricate the LSVs. The blue and red lines are the water-in and water-out lines for the water cooling system. The thin black lines represent electrical connections to the control system. . . . . 48

3.5 A simple illustration of the process of shadow deposition – here shown as a cut-away cross section at the site of the injector. **(a)** The pre-prepared template on top of the substrate (dark blue). The bottom layer of resist (light blue) has been removed to a greater degree during development forming an undercut below the top layer (mid-blue). **(b)** The ferromagnetic material (dark grey) is deposited at an angle of  $45^\circ$  to the substrate. Because of the geometry of the template it cannot reach the substrate in the central channel and deposits onto the top and side of the resist. To compensate, an extra slot is included to the right, which allows the ferromagnetic material to deposit in a thin strip where the injector is desired. **(c)** The substrate is then rotated perpendicular to the evaporation source and the non-magnetic material (light grey) is deposited, allowing it to form in the central channel. The gap between the two non-magnetic structures forces electrical current to pass through the ferromagnetic layer which allows for the spin injection. **(d)** Finally, the substrate is submerged in a strong solvent which removes all the resist and any material deposited on top, leaving only the desired metal nanostructure. The connecting Au electrical contacts have not been included in this diagram for simplicity. . . . . 49

3.6 Figures taken from [5]. **(a)** shows a schematic of the cryostat used during the measurements in this study. **(b)** An illustration of the ‘measurement stick’ used to insert samples into the cryostat. The various BNC connections displayed at the top allow for the separation of electrical connections to the nanovoltmeter and DC sourcemeter. . . . . 51

3.7 An SEM image of an LSV, overlaid with an electric circuit diagram for a local measurement. The DC current (red) is passed through the non-magnetic channel, while the change in voltage is measured between the two ferromagnets (blue). . . . . 53

- 3.8 An SEM image of an LSV, overlaid with an electric circuit diagram for a non-local measurement. The DC current (red) is passed through the injector into the non-magnetic channel, while the change in voltage is measured across the detector's interface (blue). The orientation of the applied magnetic field (parallel and in-plane to the long axis of the ferromagnetic electrodes) with respect to the devices is marked in yellow. 54
- 4.1 **(a)** shows the non-local voltages measured at specific injection currents for the Py/Ag device with an injector-detector separation of 650 nm, at 4 K. The blue dots are the voltages measured when the two Py electrodes were magnetically aligned parallel to each other, while the red dots were measured when they were aligned anti-parallel. The dashed lines are quadratic fits to Eq(4.1), but only the data for  $|I| > 250 \mu\text{A}$  were used when fitting because of a non-quadratic deviation close to 0  $\mu\text{A}$ . **(b)** shows the same two NLIVs, but decomposed into their constituent terms. The black data has had everything but the quadratic term subtracted, the blue and red data have had everything but the linear term removed (blue for the parallel IV, red for the anti-parallel) and the magenta data has had the entire quadratic fit removed, leaving only the small Gaussian shaped deviation. It should be noted that the deviation is not necessarily a truly Gaussian peak and has only been labelled as such because of its apparent appearance – it is analysed further in chapter 6. . . . . 58
- 4.2 **(a)** Two non-local IVs for the Py/Cu LSV with a separation of 550 nm at 5 K, for its parallel (blue) and anti-parallel (red) alignments. The dashed lines are quadratic fits to the voltages for  $|V| > 350 \mu\text{A}$ . **(b)** A comparison of the anti-parallel NLIVs from the Ag device (black) in Fig.4.1**(a)** and the Cu device (red) in **(a)**. The current independent term has been subtracted from both data sets to allow for a better comparison to be made between the two. The dashed lines are fits to Eq(4.1). . . . 59

- 4.3 **(a)** shows the non-local resistance from the fits to Eq(4.1) across the full range of applied magnetic field strengths, for the Py/Ag device with a separation of 650 nm at 4 K. The two magnetic alignments have been colour-coded as before, with the blue data representing the parallel state and the red data, the anti-parallel. The difference between the two states has been marked with the spin signal ( $\Delta R_S$ ) while the average value of the two states is indicated by the dashed magenta line and labelled with the baseline resistance ( $R_{BL}$ ). The black vertical lines between the two states have been added to indicate more clearly where the spin-switchings occurred. **(b)** shows the average value of  $R_{NL}$  for the parallel (blue) and anti-parallel (red) spin states of the 650 nm Py/Ag device, for a range of temperatures up to 275 K. The lines connecting the data points are added as a guide for the eye. The dashed black line is the value of  $R_{BL}$  at each temperature. . . . . 60
- 4.4 **(a)** compares the spin-switching for the 650 nm Py/Ag device at 4 K (black data) and at 290 K (red data). The red y-axis on the right has been shifted down for the data at 290 K to enable a better comparison between the two datasets. The black and red vertical lines have been added as a guide to indicate spin-switching. **(b)** compares the spin-switching for two different Ag devices at 4 K - one with a separation of 650 nm (black data) and the other with a separation of 2150 nm (blue data). Again, the y-axis for the second device has been shifted to more easily compare. . . . . 62
- 4.5 **(a)** compares the spin-switching for the 650 nm Py/Ag device at 4 K (black data) and the 550 nm Py/Cu device at 5 K (red data). The red y-axis on the right has been shifted down for the Cu's data to enable a better comparison between the two datasets. The black and red vertical lines have been added as a guide to indicate spin-switching. **(b)** compares the temperature dependence for the two ferromagnetic alignments for both the Ag (black) and Cu (red) devices with separations of 650 and 550 nm respectively. The black and red dashed lines show the value of  $R_{BL}$  for the two different devices at the full range of temperatures measured. . . . . 63

4.6 Figure taken from Stefanou’s study [1]. **(a)** shows the temperature map of a Py/Ag LSV at room temperature whilst spin injection takes place. **(b)** is a two-dimensional splice of the temperature data running across the width of the Py injector. The red line is a fit to Eq(2.59). **(c)** instead shows the temperature gradient down the length of the Ag channel, moving away from the site of current injection. **(d)** shows the cross sectional data in the region where the Ag channel overlaps the Py detector. 65

4.7 **(a)** The amount of heat generated by Joule heating, per unit length, for a current of 500  $\mu\text{A}$  in both a Ag nanowire (black) and a Py injector (red) - based on measurements of their electrical resistance. **(b)** shows the value of the quadratic parameter (A) from fitting Eq(4.1) to the NLIVs of the 650 nm Ag device in black. The values of A from each of the measurements during the magnetic field sweep have been averaged together at each temperature. In red, is the resistivity of a Py nanowire with the same dimensions as the injector, taken from Dr Stefanou’s PhD thesis [4]. The lines connecting the data points are merely a guide to the eye. . . . . 66

4.8 **(a)** The average value of the quadratic parameter at each temperature for each of the Py/Ag devices with their respective separations. The lines connecting the data points are guides for the eye. **(b)** The same graph but for the Py/Cu devices. . . . . 67

4.9 **(a)** shows the baseline resistance for each of the Py/Ag devices with their respective separations, at each temperature measured. The lines connecting the data are simply a guide for the eye. **(b)** The same graph but for the Py/Cu devices. . . . . 68

|      |  |    |
|------|--|----|
| 4.10 | <p><b>(a)</b> The right-hand axis shows the total voltage measured across the detectors of the Py/Ag devices at 5 K, that can be attributed to Joule heating in the injector. The left axis shows those same voltages converted into the effective temperatures that would be required to produce them. The dashed red line is a fit to Eq(2.59). <b>(c)</b> is the same graph but for the voltages extracted from the baseline resistance instead. The data points in red have not been included in the exponential fit due to their significant deviation from the trend. Additionally, the 800 and 900 nm devices have not been included because of their unique temperature dependence with respect to the rest of the Ag devices. <b>(b)</b> and <b>(d)</b> are the same two graphs but for the Cu devices. . . . .</p> | 69 |
| 4.11 | <p>Seebeck coefficients for Ag (red), Cu (blue) and Py (black) nanowires for the full range of temperatures. The effective Seebeck combinations for both Py/Ag and Py/Cu interfaces are shown in light red and light blue respectively. The lines connecting the data points are guides to the eye.</p>  | 70 |
| 4.12 | <p><b>(a)</b> The thermal diffusion length of the Ag channels from fits with Eq(2.59) to the signals produced by Joule (red) and Peltier (blue) heating at the detector. <b>(c)</b> shows the calculated temperature increase at the site of current injection, from the same fits. <b>(b)</b> and <b>(d)</b> show the same two graphs but for the Cu devices. . . . .</p>   | 72 |
| 4.13 | <p><b>(a)</b> The resistivity of each of the Ag channels calculated using Eq(2.48) and their respective dimensions. <b>(c)</b> shows the average resistivity of the Ag in blue. The dashed red line is a fit to Eq(2.9). <b>(b)</b> and <b>(d)</b> show the same two graphs but for the Cu devices. . . . .</p>  | 75 |
| 4.14 | <p><b>(a)</b> The reduced Lorenz number for both the Ag (red) and Cu (blue) as calculated using Eq(4.3). On the right-hand axis is the factor multiplied by the Sommerfeld value. <b>(b)</b> The thermal conductivity of both the Ag (red) and the Cu (blue) calculated using Eq(4.2). The thermal conductivity data is discrete compared to the more continuous Lorenz number plot because it has only been calculated for temperatures where fits to the thermal data were made. . . . .</p>   | 76 |

|      |   |    |
|------|---|----|
| 4.15 | (a) The thermal conductance of the Ag/SiO <sub>2</sub> interface underneath the central channel as calculated from fits to the Joule heating signal (red) and the baseline resistance (blue). (b) The same graph for the Cu devices.  | 77 |
| 5.1  | The values of $\rho$ for three of the Py/Ag devices, normalised to their minimum resistivity ( $\rho_0$ ), which was found by fitting the data with Eq(2.9). The inset shows a much closer inspection of the low temperature data.  | 87 |
| 5.2  | (a) The difference in $R_{NL}$ for the parallel and anti-parallel states ( $\Delta R_S$ ), for each of the devices with different separations, at each temperature measured. The lines connecting the data points are guides for the eye. (b) shows the spin signal of the devices plotted against their separations at three different temperatures. The dashed lines are fits to Eq(2.41) at each of the corresponding temperatures.  | 88 |
| 5.3  | (a) The spin diffusion length of the Ag (black), calculated from fits to Fig.5.2(b) using Eq(2.41). In red is the electrical mean free path of the Ag, calculated using Eq(5.1) and the resistivity shown in Fig.4.13(c), multiplied by 15.14 to allow for a better comparison of the temperature dependence. (b) The spin diffusion length from (a) divided by the mean free path. The dashed blue line is a linear fit to the data below 50 K, while the red dashed line is a linear fit to the data above 50 K. The gradients of the two lines have been marked. | 89 |
| 5.4  | (a) The spin-flip scattering rate at each temperature calculated using Eq(5.2) versus the electron-phonon scattering rate calculated using Eq(5.3). The dashed red line is a linear fit to the data above 5000 ns <sup>-1</sup> . (b) shows the difference between the spin-flip scattering rate from (a) minus the EY-predicted spin-flip scattering rate from Eq(5.4) – as a function of temperature. The red line is a linear fit to the data below 50 K, while the blue line is the same data fitted with $\ln(T_K/T)$ from Eq(2.10).                           | 91 |
| 5.5  | The approximate spin-flip probability as a percentage chance, for scattering events in the Ag devices at each temperature as calculated using Eq(5.5). The dashed red line is to mark the previously calculated value ( $a = 0.145\%$ ).  | 93 |

|     |  |     |
|-----|--|-----|
| 5.6 | The values of $\rho$ for three of the Py/Cu devices, normalised to their minimum resistivity ( $\rho_o$ ), which was found by fitting the data with Eq(2.9). The inset shows a much closer inspection of the low temperature data. . . . .   | 95  |
| 5.7 | <b>(a)</b> The spin signals for each of the Py/Cu devices plotted against temperature. The lines connecting the data points are guides for the eye. <b>(b)</b> shows the spin signal for each injector-detector separation for four different temperatures. The dashed lines are fits to Eq(2.41). . . . .   | 96  |
| 5.8 | <b>(a)</b> shows the spin diffusion length for the Py/Cu LSVs in black, as determined by fitting Eq(2.41) at each temperature. In red is the mean free path of the Cu, determined by converting the average resistivities from Fig.5.6(a) using Eq(5.1), multiplied by 7.5. <b>(b)</b> The ratio of the spin diffusion length and mean free path. The red dashed line is a linear fit to the data above 75 K while the blue dashed line is a linear fit to the data below 75 K. . . . .  | 97  |
| 6.1 | <b>(a)</b> Two non-local IVs for the 650 nm Py/Ag device at 4 K (black) and the 550 nm Py/Cu device at 5 K (red), both in the anti-parallel spin state. The dashed black and red lines are fits to Eq(4.1). Both signals have had the current-independent term from those fits subtracted to allow for a closer comparison of the two. <b>(b)</b> shows the same two IVs, but with the entire quadratic fit subtracted. The dashed lines are fits to Eq(6.1). Beneath, are the regular residuals to both the fits in the same colours. . . . . | 104 |
| 6.2 | <b>(a)</b> The deviation from the quadratic model for the 650 nm Ag device at 4 K, for both the parallel (blue) and anti-parallel (red) spin states. The dashed blue and red lines are fits to Eq(6.1). <b>(b)</b> shows the signal for both the Cu and Ag devices for a selection of their respective device separations (the Ag at 4 K, the Cu at 5 K). . . . .  | 105 |
| 6.3 | <b>(a)</b> The Gaussian signal for a range of temperatures for the Ag device with a separation of 650 nm. The dashed black and blue lines are fits to Eq(6.1), while the 30 K data could not be properly fitted. <b>(b)</b> is the same graph but for the Cu device with a separation of 550 nm. . . . .   | 106 |

6.4 **(a)** shows the height of the Gaussian peak for each of the Ag devices, as calculated from fits to Eq(6.1) for temperatures up to 45 K. The lines connecting the data points are simply guides for the eye. **(b)** is the same graph but for the Cu devices. . . . . 107

6.5 The average height of the Gaussian peak as found from fits to Eq(6.1), for each device at 5 K. The black data are the Ag devices and the red data the Cu. The blue circle highlights the two outliers from the Ag dataset. . . . . 107

6.6 **(a)** Four NLIVs for the 700 nm copper device at 7 K. Config A is the same wiring configuration as the rest of the NLIV measurements from this study. The current is passed from the injector into the Cu channel, while the voltage is measured across the detector’s interface. Config B is the same measurement, but with the positive and negative terminals of the voltmeter switched. Since this results in a negative voltage, the signal has been multiplied by -1 for comparison. Config C is the same as Config A, except that the current has been injected into the Cu from the detector (which is larger than the injector), while the voltage was measured across the injector’s interface. Config D is the same as Config A, except that larger currents were injected; the current was swept between  $\pm 700 \mu\text{A}$ . For all four measurements, the voltage at zero current has been subtracted to provide better comparison. **(b)** here, quadratic fits to the four IVs in **(a)** have been subtracted, leaving only the Gaussian signal. . . . . 110

6.7 **(a)** The quadratic parameter from fits to Eq(4.1) for each of the four configurations outlined in Fig.6.6**(a)**, for the full range of applied magnetic field strengths. **(b)** The values of the linear parameter from the same quadratic fits. . . . . 111

- 6.8 **(a)** Four NLIVs of the 700 nm copper device at 7 K. For the black data, a measurement was made every second for the full 51 current-value sweep. For the red, a measurement was made every 3 s. The blue data were taken at the same speed as the black data, but the sweep was looped four times for a total of 204 measurements. The magenta data were measured at individual current values, rather than sweeping through a range. At each current value, 51 measurements were made (once every 3 s). The device was then allowed to thermally settle for one minute, before the next measurement at the next current was made. For all of the NLIVs, the voltage at zero applied current has been subtracted to allow for better comparison. **(b)** shows the voltage as a function of time, during the measurement at 350  $\mu\text{A}$  from the magenta dataset. The dashed red line is a straight-line fit to the data and its gradient has been marked in the top-left. . . . . 113
- 6.9 Four NLIVs of the 700 nm copper device at 7 K. For the black, red, blue and magenta data, the current sweeps were applied between  $\pm 200$ ,  $\pm 750$ ,  $\pm 1750$  and  $\pm 5350$   $\mu\text{A}$  respectively. During the 5350  $\mu\text{A}$  measurement, electrical contact was lost with the device and the negative part of the sweep could not be completed. The dashed red line is a fit to Eq(4.1) for the 750  $\mu\text{A}$  data. The inset shows a closer look at the signals measured for low currents. For each of the NLIVs, the voltage at zero applied current has been subtracted. . . . . 115

# LIST OF TABLES

|     |  |    |
|-----|--|----|
| 5.1 | A table of the partial pressure measurements taken during the deposition of the Ag from the mass spectrometer. The molecules responsible for the peaks at each molecular weight have been assumed, based on the most common naturally occurring gases . The pressures represent an average over the entire deposition. . . . . | 86 |
| 5.2 | A table of calculated parameters for Ag and Cu [7], which are required for some of the calculations made in this study. $m_e$ ( $9.1094 \times 10^{-31}$ kg) is the mass of a free electron. . . . .   | 90 |
| 5.3 | A table of the partial pressure measurements taken during the deposition of the Cu, from the mass spectrometer. The values of the pressures have been averaged over the entire deposition. . . . .   | 94 |

## Abbreviations

|      |                           |      |                              |
|------|---------------------------|------|------------------------------|
| AC   | Alternating Current       | PMMA | Poly(Methyl-Methacrylate)    |
| DC   | Direct Current            | Py   | Permalloy                    |
| EY   | Elliott-Yafet             | RBL  | Baseline Resistance          |
| HMDS | Hexa-Methyldisilazone     | RF   | Reactive-Ion                 |
| IPA  | Isopropyl Alcohol         | RNL  | Non-Local Resistance         |
| IV   | Current-Voltage           | SEM  | Scanning Electron Microscopy |
| LSV  | Lateral Spin Valve        | SOC  | Spin Orbit Coupling          |
| MAA  | Methacrylic Acid          | SThM | Scanning Thermal Microscopy  |
| MMA  | Methyl-Methacrylate       | UHV  | Ultra-High Vacuum            |
| NLIV | Non-local Current-Voltage | UV   | Ultra-Violet                 |
| NMP  | Methyl-2-Pyrrolidone      | XRR  | X-Ray Reflectivity           |

---

# CHAPTER 1

---

Introduction

---

At its core, this body of work explores the motion of electrons within metallic structures and, more specifically, the way in which that motion is affected by magnetic fields and temperature.

The field of condensed matter, which describes the physics of solids, has arguably become one of the most influential in today's society. Driven by the powerful capabilities of semiconductors and society's large consumption of data, the ability to process and store stable forms of information has led to widespread investment in its research.

Over the last century, the use of transistors, which allow for the conversion of electronic charge into binary signals, has resulted in a readily accessible form of data processing. Despite this, one of the electron's other properties – its spin – lends itself more naturally to binary systems because of the fact that it is quantised into two possible orientations; in its most reduced form, only one electron is required to store a bit of information.

Within condensed matter the study of spintronics, which aims to better understand the manipulation of spins, has become one of the fastest growing areas of research in physics [8]. Spintronics consists of three core concepts:

- Spin generation
- Spin transport
- Spin detection

Development of spintronic devices called spin valves, in the 1980s [9, 10], led to the production of magnetic read-heads, which revolutionised the data storage industry. The manipulation of spins allowed for incredibly small, stable and readily re-writable magnetic structures that could be used to store vast numbers of bits.

One of the key issues facing the data industry is that, as the devices it utilises become smaller and smaller, temperature stability becomes more and more difficult to manage. Keeping data storage cool requires large amounts of energy and so it is in society's interest to find ways to circumvent the inevitable heating in spintronic devices.

In the early 2000s, laterally arranged spintronic devices called lateral spin valves were developed [11–13]. They have the unique ability to isolate the transfer of spins from the flow of the electron's charge [14, 15] – in a phenomenon called 'pure spin currents'.

---

Some studies have hypothesised that LSVs may unlock the key to transferring data without the accompanying heat generation that currently plagues the industry [16–18], although this has not yet been demonstrated experimentally.

In chapter 2, the physical descriptions required, in order to understand the origins of LSVs and the mechanisms at play within them, are outlined. A detailed derivation of the overarching model that describes spin transport is also covered. Additionally, a relatively recent model for the transport of thermal signals within LSVs is outlined.

Chapter 3 describes the techniques used to produce the LSVs used in this study and outlines the exact methodology behind the experiments performed. Chapter 4 details a step by step process by which, through thorough measurement and careful analysis, the different phenomena that occur within LSVs can be deconstructed and tests the suitability of the recently introduced thermal model.

In the last 20 years, there has been an ongoing dispute surrounding the fact that in some LSVs, the efficiency of spin transport differs at low temperatures from that previously expected [3, 4, 19, 20]. The argument centres around the role that magnetic impurities play in the transfer of spins in lateral spintronic devices. Chapter 5 directly investigates this observed discrepancy by exploring the methods used to produce LSVs, as well as by assessing the different arguments put forward by various studies.

Additionally, a signal has been recently observed in the voltages measured across some LSVs [4, 6], that deviates from the previously understood model, which has, as yet, not been comprehensively studied or explained. An attempt is made to amend this in chapter 6 by comparing different fabrication methods and measurement techniques.

Finally, chapter 7 summarises the findings from this study, highlight issues found within the conclusions made and then explores the implications on the field of spintronics moving forwards.

---

# CHAPTER 2

---

Background and Theory

Firstly, an appreciation of the electron's properties is required in order to understand the assumptions made within this study. That includes both an understanding of the way that the movement of the electron's charge behaves within solids (through a description of current), and a good grasp on the nature of the electron's spin. The flow of electrons with spin is referred to as a 'spin current' [21].

## 2.1 Spin

Spin is a quantum property of particles that is well understood but unfortunately lacks an easily intuitive description. Emerging from solutions to a relativistic alteration to Schrödinger's equation, called Dirac's equation [21], spin results in many particles (including electrons) possessing an intrinsic, as opposed to an imposed, angular momentum. It is important to clarify, however, that a particle's spin does not describe any physical angular rotation.

Electrons, which are fermions, have a spin value ( $m_s$ ) equal to  $\pm 1/2$ , representing clockwise and anti-clockwise spin angular momentum respectively. It should be noted that the axis around which the angular momentum is described can be pointed in any direction. However, when the system the electrons occupy becomes observed, only one spatial dimension (that being the z-component) of their spin-axis is maintained resulting in two possible orientations: up ( $m_s = +1/2$ ) and down ( $m_s = -1/2$ ).

The combination of the electron's charge and its spin angular momentum results in it behaving like a small bar magnet, whose magnetic moment is described by the Bohr magneton [22] ( $\mu_B = 9.27 \times 10^{-24} \text{ J T}^{-1}$ ). The magnetism of electrons in materials gives rise to many effects of which three are particularly useful to understand with regards to this study.

- Diamagnetism
- Paramagnetism
- Ferromagnetism

### 2.1.1 Diamagnetism

For the case where electrons are orbiting a positively charged nucleus, a relativistic phenomena arises. In the rest frame of the nucleus, an orbiting electron moves with

a circular path through the nucleus' electric field. As such, the electron possesses a secondary form of angular momentum, separate to its spin, called 'orbital angular momentum'.

Within the electron's rest-frame, it is instead the nucleus that moves in a circular motion. As such, because of the nucleus' positive charge, the electron experiences a magnetic field emanating from the nucleus itself. Another interpretation of this is that, when switching between the two rest-frames, the Lorentz transformation of the gradient in the nucleus' electric field induces a magnetic field called the 'spin-orbit field' that interacts with the electron's magnetic moment. This interaction is called the 'spin-orbit interaction' (also known as spin-orbit coupling (SOC))[23, 24]. Because the Lorentz transformation is dependent on the mass of the particles in question, heavier nuclei exhibit stronger SOC.

The additional energy provided to the Hamiltonian (a quantum description of the energy possessed by a system) of the electron in the case of SOC is described by  $s \cdot L$  where  $s$  is the spin angular momentum of the electron and  $L$  is its orbital angular momentum. However, for electrons with relativistic velocities (common in metals), the Lorentz factor ( $\gamma$ ) must also be taken into account. There are also other cases that can contribute to SOC (other than the nuclear potential); for example, molecular interactions such as Lennard-Jones potentials can also have an effect on electrons moving relativistically.

This effect gives rise to the most prevalent form of magnetism in materials – diamagnetism. When a body is exposed to an externally produced magnetic field, the orbital motions of its electrons adjust in such a way as to induce an opposing magnetic field, which acts to diminish the applied field [25]. All materials experience a diamagnetic response to some degree but it is often overshadowed by other, stronger effects. A famous example of diamagnetism can be seen in the video of an experiment wherein a frog is levitated by a very strong magnetic field gradient [26].

### 2.1.2 Paramagnetism

While diamagnetism is observed in all electronic orbitals, paramagnetism is an effect only associated with those that contain unpaired electrons; since pairs will always have oppositely aligned spins, their net magnetic moment is zero [25]. Unpaired electrons, on the other hand, experience a force upon them when an external magnetic field is

applied.

When a particle with spin is placed in a magnetic field, its spin can either be aligned parallel or anti-parallel to that field. The effect of the applied field is to increase the potential energy held by particles aligned anti-parallel, while decreasing the energy of parallel aligned particles. Consequently, when a magnetic field is applied to a metal containing unpaired electrons, the energies of the respective spin orientations are shifted (see Fig.2.1) and the equilibrium in the spin populations is broken [22, 25]. The resulting imbalance generates a net magnetic moment which acts to enhance the applied field. If the external field is removed however, then the electrons return to their original states and the paramagnetism ceases.

### 2.1.3 Ferromagnetism

Although paramagnetism is an important property of most metals, it fails to explain the permanent magnetism observed in some elements such as Fe. In such ferromagnetic materials there must be some mechanism by which spontaneous and sustained magnetisation can occur.

The mechanism in question is called the exchange interaction – an effect that occurs between any electrons within the same quantum system. Electrons, like all fermions, obey a statistical rule called the Pauli exclusion principle, which forces them to occupy non-identical quantum states. As a result, electrons must either possess oppositely aligned spins OR occupy separate orbitals. Electrons which occupy different orbitals but have parallel spins are naturally positioned further apart and, because of the Coulomb repulsion between like charges, have less potential energy than those in the same orbital [22, 24, 25, 27].

Since particles act in a way to minimise their energy, in most metals there is a force prevalent upon the electrons that attempts to align their spins. In order for such spontaneous magnetisation to occur, the change in energy brought about by the exchange interaction must be able to overcome the kinetic energy that the electrons possess. Since the exchange interaction is dependent on the Coulomb repulsion between electrons, the density of the electron orbitals (i.e. the density of states) has a large impact on the likelihood of spontaneous magnetisation.

The balancing point between the energy gained by an alignment of spins and the electrons' kinetic energy is described by the Stoner criterion [28]

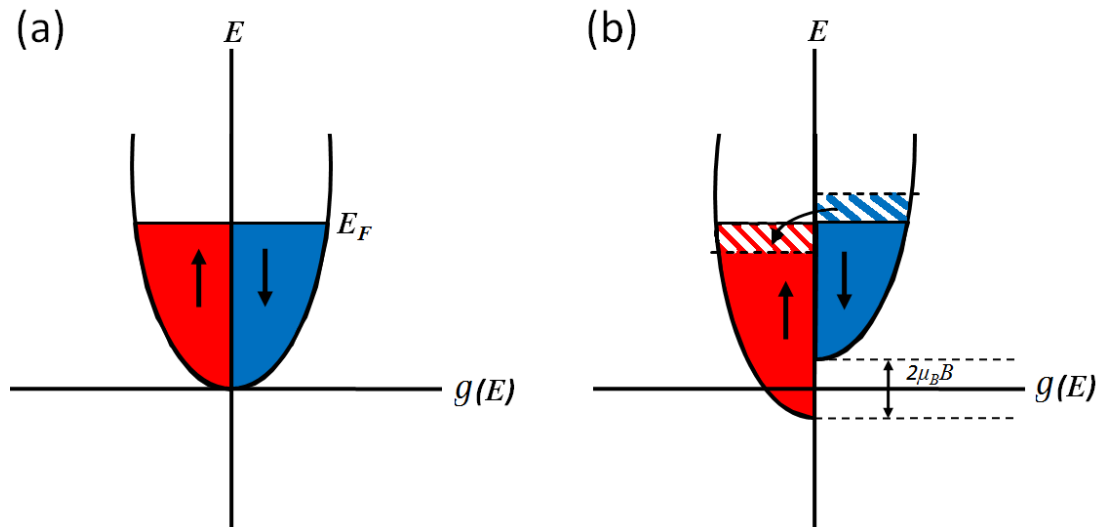


Figure 2.1: **(a)** The distribution of energy ( $E$ ) for electrons in a paramagnet at a temperature of absolute zero, with the x-axis showing the number of allowed states at each possible energy, per unit volume (called the density of states) -  $g(E)$ . The electrons have been shown separately for the two different spin alignments (red for up spins and blue for down spins) and all possible states below the Fermi energy ( $E_F$ ) are filled. **(b)** The response to an applied magnetic field ( $B$ ) that is pointed upwards in the  $z$  direction. The electrons that have spins parallel to the magnetisation have their energy reduced by an amount equal to  $\mu_B B$ , while the opposite is true for the anti-parallel spins. The spins of electrons above  $E_F$  (represented by the dashed blue lines) will flip direction so as to occupy the available lower energy states (represented by the dashed red lines) with the opposite spin. As a result, the populations of each spin direction will no longer be equal in number and the material becomes magnetic.

$$I g(E_F) > 1 \tag{2.1}$$

where  $I$  is the Stoner parameter. If the above inequality is reached within a material, then the spins within it will tend to align and spontaneous magnetisation is likely to occur. The Stoner criterion is only overcome by three elements in the upper periodic table at room temperature: Fe, Co and Ni.

In ferromagnets, spontaneous magnetisation will occur below a critical temperature ( $T_C$  - its Curie temperature), resulting in a net polarisation of spins. The energy distribution of the material after magnetisation is similar to that of a paramagnet under the application of an external field (See Fig.2.1(b)). As the temperature ( $T$ ) increases from absolute zero, the magnetisation ( $M$ ) of a ferromagnet drops because of the increase in thermal energy, the reduction of which is described by Bloch's law [7]

$$M = M_0(1 - (T/T_C)^{3/2}) \tag{2.2}$$

where  $M_0$  is the magnetisation as  $T \rightarrow 0$  K. Hereafter, whenever the word 'magnetic' is used, it is referring to ferromagnetism as opposed to diamagnetism or paramagnetism.

## 2.2 Electron Transport

It may seem initially intuitive, but the fact that metals conduct electricity so easily, while other materials do not, is actually a complex and integral part of the field of condensed matter. Electrons are most commonly found 'bound' orbiting around positive nuclei; however, despite the apparent parallels that can be drawn with planets gravitationally orbiting the sun, quantum mechanics introduces a key difference to the equation – electrons have distinct quantised energy levels and as such, cannot simply be 'nudged' into marginally larger orbits.

Consequently, the quantum nature of orbiting electrons does not lend itself naturally to the concept of them freely travelling through conductive materials. The disagreement can be resolved by the fact that in a regularly repeating structure, such as the crystal lattices of most solids, boundary conditions are imposed which alter the electrons' orbitals in such a way that the allowed energy levels become 'split' [25].

### 2.2.1 Band Theory of Solids

For sufficiently large structures, with many orders of atomic nuclei, the energy levels are split so many times that the gaps between them become insignificant and a continuous band of allowed energies is formed. As a direct consequence, some electrons can be very easily given additional kinetic energy and hence move further away from the atomic nuclei. Additionally, because the quantum states of the atomic orbitals interact with each other, the electrons are free to move between them and are no longer considered bound. This reveals how electrical conductivity in solids is possible but it does not explain the special nature of metals.

Although the crystal structure of some solids results in the formation of continuous energy bands, it also yields solutions to Schrödinger's equation that describe standing waves for very specific electron momenta. Since standing wave states possess a group velocity of zero, the dispersion relation (energy vs momentum relationship) of the electrons is disrupted.

A group velocity of zero, by definition means that the rate of change in energy for a wave with respect to its wavevector is zero and so the continuous nature of the electrons' dispersion relation is broken at points called van Hove singularities. These singularities occur at the boundaries of the Brillouin zones, which describe the primitive cells of the crystal lattice in reciprocal space, with wavevector values of  $\pm \frac{\pi}{a}$  – where  $a$  is the distance between neighbouring nuclei (the lattice constant).

Electrons that occupy states near to the van Hove singularities have a much larger effective mass ( $m^*$ ) than that of a free electron ( $9.11 \times 10^{-31}$  kg) and hence much more energy is required to change their momentum. Additionally the density of states near the Brillouin zone boundaries is usually very large. Because of the asymptotic nature of the singularities in the dispersion relation, a gap in the possible energy values appears – referred to as a 'band gap'. As such, gaps of forbidden states for the electrons form, corresponding to each harmonic of standing wave [25].

There are an infinite number of band gaps in the possible energies of any given crystal structure but it is their relation to  $E_F$  that defines the electrical behaviour of the solid (see Fig.2.2). Because of the Pauli exclusion principle, only two electrons (with oppositely-aligned spins) can possess the same energy and so in a system with many electrons, states with higher energies become occupied.

At a temperature of zero Kelvin, when the electrons possess no thermal energy, all

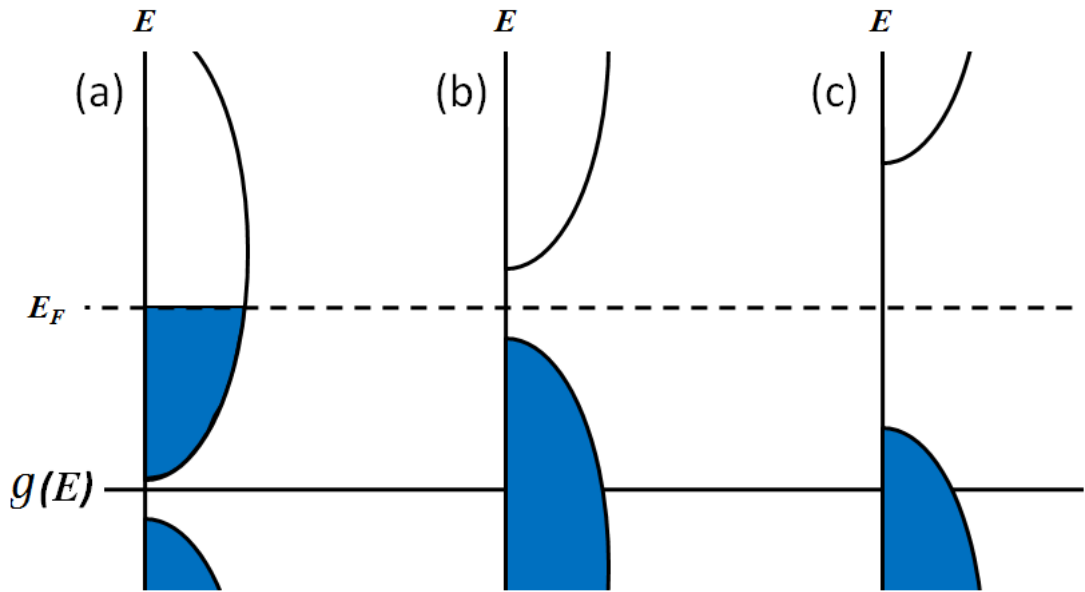


Figure 2.2: The distribution of electrons and their energies for 3 different types of solid at absolute zero: **(a)** shows the band structure for a metal;  $E_F$  lies within one of the energy bands which means that electrons can very easily move into higher energy states. As a result, when an electrical field ( $\vec{E}$ ) is applied, electrons will gain kinetic energy and begin to move with the field. **(b)** on the other hand, shows a semiconductor. Here,  $E_F$  lies within a band gap meaning that electrons cannot easily be given more energy. A semiconductor will conduct when a large  $\vec{E}$  is applied or at very high temperatures. **(c)** shows the structure for an insulator. Here, the band gap is very large because of properties within the crystal structure and so it is almost impossible to give electrons enough energy to conduct freely.

of the lowest possible energy states are filled - in a system with no excited electrons, the uppermost filled energy state is defined as  $E_F$ . The position of the most energetic electrons in relation to a material's band gaps determines how easily they can be given kinetic energy. In Fig.2.2 it can be seen that metals contain freely conducting electrons because of the fact that  $E_F$  does not lie close to one of the gaps.

Because of the large number of electrons in macroscopic materials, the allowed states are very closely packed together and are said to have a large 'degeneracy'. The density of these states with respect to their energy can be approximated, at  $E_F$ , to be [25]

$$g(E_F) = \frac{3n}{2E_F} \quad (2.3)$$

where  $n$  is the number of electrons per unit volume. As the temperature of a material is increased from absolute zero, some of the electrons near  $E_F$  gain energy of the order of  $k_B T$ , where  $k_B$  is the Boltzmann constant ( $1.3806 \times 10^{-23} \text{ J K}^{-1}$ ). As fermions, electrons obey the Fermi-Dirac distribution which results in a gradient of the occupied states at  $E_F$ .

### 2.2.2 Conductivity

When a force (such as that imposed by an electric field) is applied to a particle, its energy increases with time. Therefore, in electrical conductors, there must be some mechanism by which electrons can dissipate some of their kinetic energy while they are accelerated. Otherwise, their velocity would steadily tend towards the speed of light over time. The mechanism by which the required dissipation occurs is through collisions called 'scattering events' which act to either absorb or impart momentum from or on to the moving electrons.

Scattering within electrical conductors results in a steady-state equilibrium, in which the flow of charges settles into a constant current - proportional to the number of electrons and their velocity [7]

$$\vec{j}_c = -ne\vec{v}_d = \frac{ne^2\tau\vec{E}}{m^*} \quad (2.4)$$

where  $\vec{j}_c$  is the flow of charge per unit volume (current density),  $e$  is the charge of an electron,  $\vec{v}_d$  is the drift velocity of the electrons,  $\tau$  is the average time between scattering events,  $\vec{E}$  is the applied electric field strength.

The efficiency with which an applied electric field generates a flow of electrons within a material is defined as the material's electrical conductivity ( $\sigma$ ), which is described by Ohm's law

$$\sigma = \frac{\vec{j}_c}{\vec{E}} = \frac{ne^2\tau}{m^*} = \frac{1}{\rho} \quad (2.5)$$

where  $\rho$  is the resistivity and is defined as the inverse of  $\sigma$ .

It is important to clarify the difference between two different forms of velocity that the electrons possess. Their drift velocity describes the average motion of the entire population of electrons over time. Because of large numbers of scattering events, the drift velocity is usually fairly low (the order of a few nanometres per second). The motion of individual electrons, on the other hand, is described by their Fermi velocity ( $V_F$ ), which is function of their kinetic energy [25].  $V_F$  is much larger (usually a few thousand kilometres per second) than  $\vec{v}_d$  but the direction with which the velocity is associated is generally random. It is only through the application of electric fields that small, net changes to the Fermi velocities lead to an overall flow of charge.  $V_F$  is related to the Fermi energy via the kinetic energy equation

$$E_F = \frac{1}{2}m^*V_F^2 \quad (2.6)$$

Another important property, the mean free path ( $\lambda$ ), is dependent on the amount of scattering. It describes the average distance each individual electron travels between scattering events and is directly related to the average scattering time as well as the electrons' speed.

$$\lambda = \tau V_F \quad (2.7)$$

### 2.2.3 Scattering

It might appear intuitive that the obvious source of scattering for electrons would be with the atomic nuclei themselves; however, the electrons' interactions with the repeating nuclei are entirely taken into account by the standing wave states (referred to as Bloch states) that form between them. Consequently, the amount of scattering events between the electrons and the nuclei can be treated as negligible.

One of the main contributions to the amount of scattering comes from thermal excitations which disrupt the crystal lattice; such oscillations can be modelled as quasi-particles called phonons that act to transfer heat energy throughout the structure.

Electrons interact with phonons while they both move through the crystal structure, transferring momentum between each other. Electron-phonon interactions account for most of the scattering within metals at high temperatures [25].

At low temperatures, when the amount of thermal excitations is greatly diminished, scattering still occurs. The electrons can interact with more permanent imperfections in the crystal structure such as impurities, grain boundaries and the material's surface. Such defects in the crystal lattice disrupt its repeating nature and act to interfere with the wave states of the electrons. Scattering with imperfections is temperature independent and thus leads to a minimum value of  $\rho$  at low temperatures ( $\rho_0$ ).

The electrons can also scatter with each other, but the rate at which they do so is much smaller than one might imagine. The main reason is that two electrons can only collide if there are two available energy/momenta states for them to scatter into (although, inelastic scattering can occur where excess momentum is transferred to the lattice in the form of a phonon). As  $T$  increases, the Fermi-Dirac distribution at  $E_F$  causes an increase in the number of available states and, as such, the number of electron-electron scattering events increases with temperature [25].

By assuming that the main scattering mechanisms within metals are independent of each other, then the rate at which each type of scattering occurs can be simply summed together. This is known as Matthiessen's rule

$$\frac{1}{\tau} = \frac{1}{\tau_0} + \frac{1}{\tau_e} + \frac{1}{\tau_{ph}} \quad (2.8)$$

where  $\tau_0$ ,  $\tau_e$  and  $\tau_{ph}$  are the times between electron-defect, electron-electron and electron-phonon scattering events respectively. Eq(2.8) can instead be written in terms of  $\rho$  using Eq(2.5) such as in the Bloch-Grüneisen formula [29] for the temperature dependence of  $\rho$  in metals

$$\rho = \rho_0 + \rho_e + \rho_{ph} = \rho_0 + R_e T^2 + R_{ph} \left(\frac{T}{\theta_D}\right)^5 \int_0^{\frac{\theta_D}{T}} \frac{x^5}{(e^x - 1)(1 - e^{-x})} dx \quad (2.9)$$

where  $\rho_e$  and  $\rho_{ph}$  are the resistivities resulting from interactions with electrons and phonons respectively,  $R_e$  and  $R_{ph}$  are material dependent constants and  $\theta_D$  is a characteristic temperature called the Debye temperature.

The  $T^2$  contribution originates with the electron-electron interactions (one power of  $T$  for each of the colliding electrons), while the term on the far right increases according to  $T^5$  at lower temperatures and then linearly with temperature as  $T$  becomes larger than  $\theta_D$  (and the integral approximates to  $T^{-4}$ ).

Another form of scattering in metals of significance to this study is the Kondo effect, which arises when the crystal of a non-magnetic metal contains isolated impurities that have magnetic moments (for example Fe impurities in Cu). The result is an increase in  $\rho$  as  $T$  approaches 0 K, because of SOC between the conducting electrons and the unpaired electrons bound to the impurity [27, 30]. The coupling gets logarithmically stronger at low temperatures; although for very low  $T$ , the impurities become fully screened by a cloud of coupled conducting electrons and  $\rho$  does not diverge to infinity. The Kondo effect can be added as an extra term to Eq(2.9)

$$\rho_k = k \cdot \ln\left(\frac{T_K}{T}\right) \quad (2.10)$$

where  $k$  is a constant and  $T_K$  is the temperature at which the effect becomes non-negligible (called the Kondo temperature). Eq(2.10) does not include the correction required for screening and so diverges as  $T$  approaches 0 K; as a result it becomes inaccurate at very low temperatures.

## 2.3 Spin Transport

Now that basic descriptions of magnetism and electron transport have been outlined, the concept of spin currents, which describe the flow of angular momentum, can be addressed [21].

### 2.3.1 Spin Dependent Scattering

One of the most significant properties of magnetic materials, when considering the transport of spins, is the difference in  $\sigma$  that arises for electrons with different alignments. In most metals, the two spin populations ( $n_\uparrow$  and  $n_\downarrow$ ) are equal, as are the spin-dependent scattering times ( $\tau_\uparrow$  and  $\tau_\downarrow$ ), meaning that

$$\sigma_\uparrow = \sigma_\downarrow = \frac{ne^2\tau}{2m^*} = \frac{1}{2}\sigma \quad (2.11)$$

where  $\sigma_\uparrow$  and  $\sigma_\downarrow$  are the conductivities of the up and down spin electrons respectively. However, in ferromagnets, because the two spin populations are no longer equal in size, the previous equivalences cannot be assumed and

$$\sigma_\uparrow = \frac{n_\uparrow e^2 \tau_\uparrow}{m^*} \quad \sigma_\downarrow = \frac{n_\downarrow e^2 \tau_\downarrow}{m^*} \quad (2.12)$$

The discrepancy in the conductivities of the two spin orientations can also be explained by the fact that in a ferromagnet, the two spin sub-bands have been split in energy by the exchange interaction (see Fig.2.3(b)) and, consequently,  $E_F$  lies at a different point within the up and down bands respectively [22]. The amount of scattering that an electron experiences (and hence  $\tau$ ) is described by Fermi's golden rule [31].

$$\frac{1}{\tau} = \sum_f W_{i \rightarrow f} = \sum_{f,i} \left( \frac{2\pi}{\hbar} |V_{fi}| \delta(\epsilon_f - \epsilon_i) \right) = \sum_f \frac{2\pi}{\hbar} |V_{fi}| g(E_f) \quad (2.13)$$

where  $W_{i \rightarrow f}$  is the transition rate from an initial state  $i$  to a final state  $f$ ,  $V_{fi}$  is the transition-coupling potential between them and  $\delta(\epsilon_f - \epsilon_i)$  is a delta function that constrains the energies of the transition.

Fermi's golden rule defines the transition probability between any two quantum states. It is dependent on the coupling between the initial and final states as well as the number of final states that can be transitioned into. For electron scattering, the coupling is defined by the cross-section of the scattering event (governed by the interaction potential) and the number of available transition states is determined by the density of states at the Fermi energy. Effectively, a large  $g(E_F)$  results in more scattering and, as such, a lower electrical conductivity.

The result is that when  $E_F$  lies within a d-band (which it tends to do in ferromagnets) which has rapidly varying density of states, the amount of scattering that the two spin populations experience can be significantly different. In general, materials in which  $E_F$  lies in the s-band (such as the noble metals as in Fig.2.3(a)) are better electrical conductors than the ferromagnets [32].

Electrical devices called spin valves demonstrate the effect of spin dependent conductivities very clearly. They were developed separately by two teams in the 1980s, for which Fert and Grünberg [33, 34] were both awarded the Nobel prize in recognition of their significance. Spin valves consist of two ferromagnetic layers separated by a non-magnetic spacer (see Fig.2.4) and are named for their ability to generate clear binary electrical signals when small, applied magnetic fields are varied (a valve can either be 'on' or 'off').

The devices are engineered in such a way that the two ferromagnetic layers can be magnetically realigned independently. This can be achieved by either giving the two layers different thicknesses or by using two different ferromagnetic materials. The non-magnetic spacer is required so that the magnetisations of the two layers do not

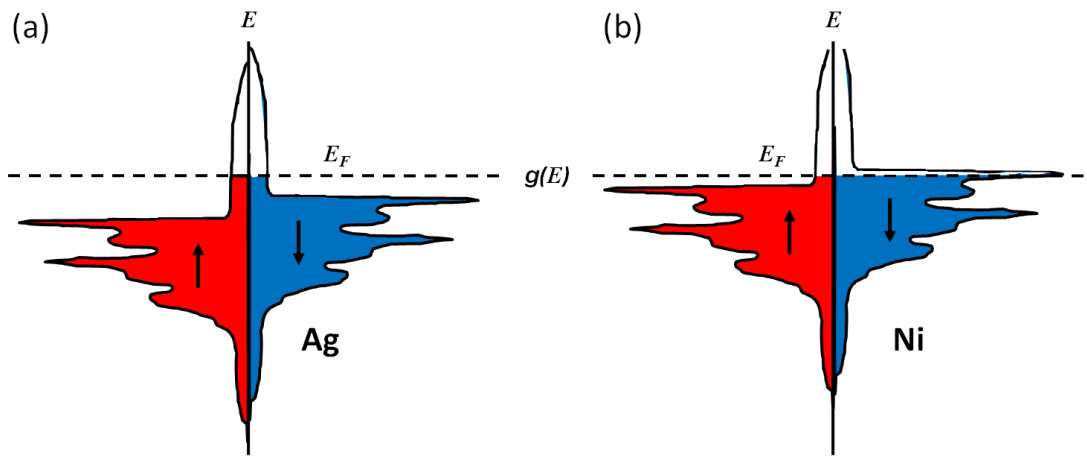


Figure 2.3: A more realistic band diagram of the density of states for two metals. **(a)** shows Ag, which is a paramagnet, after a magnetic field pointing upwards along the  $z$ -axis has been applied. The energies of the bands have both shifted by  $\mu_B B$  and the populations of spins have adjusted accordingly.  $E_F$  lies in the very narrow part of the structure (called the  $s$ -band) for both spin directions, which has a very high conductivity due to its low  $g(E)$ . **(b)** shows Ni, a ferromagnet, after spontaneous magnetisation in the up direction. The up spins'  $E_F$  has shifted and lies in the highly conductive  $s$ -band. For the down spins, on the other hand,  $E_F$  has shifted into the more densely populated part of the structure (called the  $d$ -band) where the conductivity is much lower because of the high  $g(E)$  as well as the large number of empty states that can be occupied just above  $E_F$ .

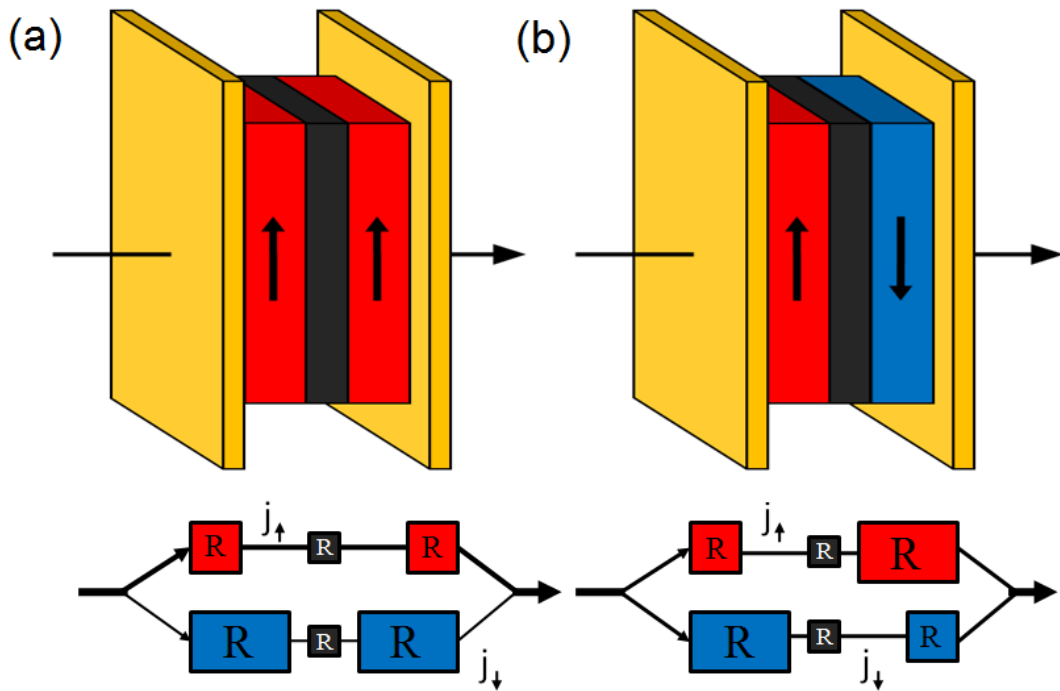


Figure 2.4: A diagram of a spin valve structure, where the blue and red layers represent the ferromagnets while the grey layer is a non-magnetic, conductive spacer. The golden panels are electrical contacts. Underneath is a simple resistor schematic for each scenario, with the spin-dependent currents split into parallel current paths. **(a)** shows the device in its parallel state: up spin electrons will experience less scattering than down spins in both magnetic layers and, as such, will flow more readily through the device. **(b)** shows the anti-parallel alignment: here the up spins will experience more scattering in the 2nd magnetic layer while the down spin electrons experience more scattering in the 1st – thus resulting in an overall equal current for both spins. It should be noted that in reality the layers of the spin valve are instead arranged vertically due to the nature of the device fabrication.

interact with each other. The result is that, by varying an applied magnetic field, the two magnetic layers can be switched between a parallel or anti-parallel alignment.

If the two spin populations are modelled as two separate currents flowing in parallel circuits, then the two ferromagnetic layers can be thought of as resistors in series with each other [35], as shown in Fig.2.4. In the magnetically parallel state (Fig.2.4(a)), the up-spin current path has a lower resistance than the down-spin current path, which for a parallel circuit results in a lower overall resistance. Conversely, in the anti-parallel magnetic state (Fig.2.4(b)), both current paths contain a large and a small resistance resistor. As a result, there is no low resistance path for the current to take and the overall device is significantly more resistive.

Fert’s team named the magnetic dependence in their devices ‘giant magnetoresistance’ (GMR) and its discovery led to the development of magnetic read heads which revolutionised the data storage industry.

### 2.3.2 Spin Injection

Also in the 1980s, the process of ‘spin injection’ was discovered by Johnson and Silsbee [9, 10, 36]. Spin injection occurs when current passes from a ferromagnet directly into a non-magnet and is caused by the magnet’s propensity to polarise currents that pass through it.

As was shown previously with spin valves, electrons with spins aligned parallel to the magnetisation of a ferromagnet will conduct more easily than those aligned anti-parallel, resulting in an unbalanced flow of spins. Therefore, a ferromagnet will confer angular momentum upon any charge current ( $\vec{j}_c$ ) that passes through it – resulting in a spin current ( $\vec{j}_s$ ).  $\vec{j}_c$  is given by the total flow of electrons while  $\vec{j}_s$  describes the difference in flow between the two spin alignments [21]

$$\vec{j}_c = \vec{j}_\uparrow + \vec{j}_\downarrow \quad \vec{j}_s = \vec{j}_\uparrow - \vec{j}_\downarrow \quad (2.14)$$

where  $\vec{j}_\uparrow$  and  $\vec{j}_\downarrow$  are the current densities of the up and down spin electrons respectively.

In a ferromagnet, the imbalance in the spin populations is called its polarisation (P), which is important to distinguish from a spin current’s polarisation ( $\alpha$ ) [21]

$$P = \frac{\Delta n}{n} = \frac{\sigma_\uparrow - \sigma_\downarrow}{\sigma_\uparrow + \sigma_\downarrow} \quad \text{whereas} \quad \alpha = \frac{\vec{j}_s}{\vec{j}_c} = \frac{\vec{j}_\uparrow - \vec{j}_\downarrow}{\vec{j}_\uparrow + \vec{j}_\downarrow} \quad (2.15)$$

where  $\Delta n$  is the difference in spin populations.

The result of passing a current through a ferromagnet into a non-magnet is that, because of the spin-polarised current, an excess of up-spins begins to accumulate at the interface between the two. This creates an imbalance in the population of the two spins within the non-magnet – effectively injecting magnetism directly into it. Because of the Pauli exclusion principle, the up-spin electrons are forced to occupy higher energy levels while vacant down-spin states are left by the reduced number of incoming down-spin electrons.

When there is gradient in the occupancy of energy levels across a material, electrons will diffuse along it in order to minimise their energies. A detailed derivation of the process by which the diffusion of spins takes place is foundational to this study.

### 2.3.3 Spin Diffusion

Valet and Fert developed a 1-dimensional model for the diffusion of spins in the early 1990s [35]. This section will work through a version of their model, presented by Ando and Saitoh [21], in order to support some of the analysis performed in later chapters.

To begin with, a system with spinless electrons in an applied  $\vec{E}$  is considered. The total flow of charges is assumed to consist of currents caused by both their drift velocity ( $\vec{j}_{\text{drift}}$ ) and their diffusion because of a gradient in their distribution ( $\vec{j}_{\text{diff}}$ ).

$$\vec{j}_c = \vec{j}_{\text{drift}} + \vec{j}_{\text{diff}} = \sigma \vec{E} + eD \frac{\partial n}{\partial x} \quad (2.16)$$

where Eq(2.5) is substituted for  $\vec{j}_{\text{drift}}$ , while Fick's law for diffusive motion, which is derived from two equations, a diffusion equation and a continuity equation, has been used for  $\vec{j}_{\text{diff}}$

$$\frac{\partial n}{\partial t} = D \frac{\partial^2 n}{\partial x^2} \quad \text{and} \quad \frac{\partial n}{\partial t} = -\frac{\partial \vec{j}_{\text{diff}}}{\partial x} \quad \text{gives} \quad \vec{j}_{\text{diff}} = -D \frac{\partial n}{\partial x} \quad (2.17)$$

where  $D$  is called the diffusion constant and  $\frac{\partial n}{\partial x}$  represents a spatial gradient in the density of the electron population. Note, the extra factor of  $-e$  in Eq(2.16) is introduced because Fick's law describes the diffusion of chargeless particles while  $\vec{j}_c$  is dependent on the flow of charges.

A spatial gradient in the density of an electron distribution is reflected by a spatial gradient in the chemical potential ( $\mu^c$ ), the uppermost occupied energy level.  $\mu^c$  is

distinct from  $E_F$  by the virtue of that it takes the thermal energy into account as well. The two spatial gradients are related by the density of states

$$\frac{\partial n}{\partial x} = g(E_F) \frac{\partial \mu^c}{\partial x} \quad (2.18)$$

The application of  $\vec{E}$  provides an additional gradient to the energies of the electrons which is combined with  $\mu^c$  to form the electrochemical potential ( $\mu$ )

$$\frac{\partial \mu}{\partial x} = \frac{\partial \mu^c}{\partial x} + e\vec{E} = \frac{1}{g(E_F)} \frac{\partial n}{\partial x} + e\vec{E} \quad (2.19)$$

Rearranging Eq(2.19) in terms of  $\frac{\partial n}{\partial x}$  and substituting it into Eq(2.16) gives

$$\vec{j}_c = \sigma \vec{E} + g(E_F) e D \left( \frac{\partial \mu}{\partial x} - e\vec{E} \right) \quad (2.20)$$

The relation between  $\sigma$  and  $D$  can be found by looking at the specific case where the applied  $\vec{E}$  acts to exactly oppose the diffusion of electrons (ie.  $\frac{\partial \mu}{\partial x} = \vec{j}_c = 0$ ). This is called Einstein's relation

$$D = \frac{\sigma}{e^2 g(E_F)} \quad (2.21)$$

which can then be substituted back into Eq(2.20) in place of  $\sigma$  to give

$$\vec{j}_c = e^2 g(E_F) D \vec{E} + e g(E_F) D \left( \frac{\partial \mu}{\partial x} - e\vec{E} \right) = \frac{\sigma}{e} \frac{\partial \mu}{\partial x} \quad (2.22)$$

which shows that the motion of electrons in such a system is dependent entirely on the gradient in the electrochemical potential.

In order to describe the mechanics behind spin diffusion, the spin of the electrons must now be reintroduced to the model. At this point, the electrochemical potential needs to be considered separately for up and down spins ( $\mu_\uparrow$  and  $\mu_\downarrow$ ) and so Eq(2.22) becomes

$$\vec{j}_\uparrow = \frac{\sigma_\uparrow}{e} \frac{\partial \mu_\uparrow}{\partial x} \quad \vec{j}_\downarrow = \frac{\sigma_\downarrow}{e} \frac{\partial \mu_\downarrow}{\partial x} \quad (2.23)$$

which, when combined with the definitions of charge and spin currents from Eq(2.14), results in

$$\vec{j}_c = \frac{1}{e} \frac{\partial}{\partial x} (\sigma_\uparrow \mu_\uparrow + \sigma_\downarrow \mu_\downarrow) \quad \vec{j}_s = \frac{1}{e} \frac{\partial}{\partial x} (\sigma_\uparrow \mu_\uparrow - \sigma_\downarrow \mu_\downarrow) \quad (2.24)$$

Next, the continuity equations for charge and spin relate the change of total charges/spins with the charge/spin currents which, in a state of equilibrium, are

$$e \frac{\partial n}{\partial t} = -\frac{\partial \vec{j}_c}{\partial x} = 0 \quad \frac{\partial M}{\partial t} = -\frac{\partial \vec{j}_s}{\partial x} + \tau_{sf} = 0 \quad (2.25)$$

where  $\tau_{sf}$  is the spin relaxation time.  $\tau_{sf}$  can be described by the single-pole approximation

$$\tau_{sf} = \frac{e(n_{\uparrow} - \bar{n}_{\uparrow})}{\tau_{\uparrow\downarrow}} - \frac{e(n_{\downarrow} - \bar{n}_{\downarrow})}{\tau_{\downarrow\uparrow}} \quad (2.26)$$

where  $n_{\uparrow}$ ,  $n_{\downarrow}$ ,  $\bar{n}_{\uparrow}$ ,  $\bar{n}_{\downarrow}$ ,  $\tau_{\uparrow\downarrow}$  and  $\tau_{\downarrow\uparrow}$  are the electron density, equilibrium electron density and spin-flip scattering times for up and down electrons respectively. By combining Eq(2.24), Eq(2.25), Eq(2.26) and the detailed balance principle, which states that

$$\frac{g(E_F)_{\uparrow}}{\tau_{\uparrow\downarrow}} = \frac{g(E_F)_{\downarrow}}{\tau_{\downarrow\uparrow}} \quad (2.27)$$

where  $g(E_F)_{\uparrow}$  and  $g(E_F)_{\downarrow}$  are the spin-dependent density of states, the spin diffusion equations are obtained

$$\frac{\partial^2}{\partial x^2}(\sigma_{\uparrow}\mu_{\uparrow} + \sigma_{\downarrow}\mu_{\downarrow}) = 0 \quad \frac{\partial^2}{\partial x^2}(\mu_{\uparrow} - \mu_{\downarrow}) = \frac{1}{l_{sf}^2}(\mu_{\uparrow} - \mu_{\downarrow}) \quad (2.28)$$

where  $l_{sf}$  is called the spin diffusion length and is equal to

$$l_{sf} = \sqrt{D\tau_{sf}} \quad (2.29)$$

The spin diffusion length is a characteristic length scale that describes the distance over which a polarised distribution of spins will diffuse before being scattered back into equilibrium. It is dependent on the amount of spin-flip scattering within a material. The effect of spin diffusion is that the spin polarisation decreases with distance from the site of spin accumulation ( $x$ ), which results in a gradient in  $\mu_{\uparrow}$  and in  $\mu_{\downarrow}$ .

### 2.3.4 Ferromagnetic/Non-Magnetic Interfaces

With a mathematical description of spin diffusion in place, the process of spin injection across a ferromagnet/non-magnet interface can now be described by solving Eq(2.28) for a set of given boundary conditions – as presented by Ando and Saitoh [21]. For a system with an interface at  $x = 0$ , the spin-dependent electrochemical potentials are given by the general solutions

$$\mu_{\uparrow}^F(x) = A^F + B^F x + \frac{C^F}{\sigma_{\uparrow}^F} e^{(x/l_{sf}^F)} + \frac{D^F}{\sigma_{\uparrow}^F} e^{-(x/l_{sf}^F)} \quad (2.30)$$

$$\mu_{\downarrow}^F(x) = A^F + B^F x - \frac{C^F}{\sigma_{\downarrow}^F} e^{(x/l_{sf}^F)} - \frac{D^F}{\sigma_{\downarrow}^F} e^{-(x/l_{sf}^F)} \quad (2.31)$$

$$\mu_{\uparrow}^N(x) = A^N + B^N x + \frac{2C^N}{\sigma^N} e^{(x/l_{sf}^N)} + \frac{2D^N}{\sigma^N} e^{-(x/l_{sf}^N)} \quad (2.32)$$

$$\mu_{\downarrow}^N(x) = A^N + B^N x - \frac{2C^N}{\sigma^N} e^{(x/l_{sf}^N)} - \frac{2D^N}{\sigma^N} e^{-(x/l_{sf}^N)} \quad (2.33)$$

where A, B, C and D are coefficients to be determined by the boundary conditions. Here, the superscripts F and N have been used to denote whether the variable is for the ferromagnet or non-magnet respectively. Additionally,  $\sigma_{\uparrow}^N = \sigma_{\downarrow}^N = \sigma^N / 2$  has been used, since the scattering is spin-independent in the non-magnetic material.

The first boundary condition that can be applied is that the two spins' electrochemical potentials are equal far away from the interface: so at  $x = -\infty$ ,  $\mu_{\uparrow}^F = \mu_{\downarrow}^F$ . Likewise at  $x = +\infty$ ,  $\mu_{\uparrow}^N = \mu_{\downarrow}^N$ . As a result,  $C^N = D^F = 0$ .

The second boundary condition is that the total charge current passing through both materials must be the same. Therefore,  $j_c = j_{\uparrow}^F + j_{\downarrow}^F = j_{\uparrow}^N + j_{\downarrow}^N$ . which in combination with Eq(2.23) gives  $B^F = ej_c / \sigma^F$  and  $B^N = ej_c / \sigma^N$ . It should be noted that  $\sigma^F = \sigma_{\uparrow}^F + \sigma_{\downarrow}^F$  has been used here.

The final boundary condition is that at the interface, the electrochemical potentials of each spin direction must be continuous, as well as the flow of each spin; which, when setting  $A^F = 0$ , yields the following solutions

$$\mu_{\uparrow}^F(x) = \frac{ej_c}{\sigma^F} x - \frac{ej_c P l_{sf}^N (1 - P^2) \sigma^F}{2\sigma_{\uparrow}^F \sigma^N \left(1 + (1 - P^2) \frac{\sigma^F l_{sf}^N}{\sigma^N l_{sf}^F}\right)} e^{(x/l_{sf}^F)} \quad (2.34)$$

$$\mu_{\downarrow}^F(x) = \frac{ej_c}{\sigma^F} x + \frac{ej_c P l_{sf}^N (1 - P^2) \sigma^F}{2\sigma_{\downarrow}^F \sigma^N \left(1 + (1 - P^2) \frac{\sigma^F l_{sf}^N}{\sigma^N l_{sf}^F}\right)} e^{(x/l_{sf}^F)} \quad (2.35)$$

$$\mu_{\uparrow}^N(x) = \frac{ej_c P^2 l_{sf}^N}{\sigma^N \left(1 + (1 - P^2) \frac{\sigma^F l_{sf}^N}{\sigma^N l_{sf}^F}\right)} + \frac{ej_c}{\sigma^N} x - \frac{ej_c P l_{sf}^N}{\sigma^N \left(1 + (1 - P^2) \frac{\sigma^F l_{sf}^N}{\sigma^N l_{sf}^F}\right)} e^{-(x/l_{sf}^N)} \quad (2.36)$$

$$\mu_{\downarrow}^N(x) = \frac{ej_c P^2 l_{sf}^N}{\sigma^N \left(1 + (1 - P^2) \frac{\sigma^F l_{sf}^N}{\sigma^N l_{sf}^F}\right)} + \frac{ej_c}{\sigma^N} x + \frac{ej_c P l_{sf}^N}{\sigma^N \left(1 + (1 - P^2) \frac{\sigma^F l_{sf}^N}{\sigma^N l_{sf}^F}\right)} e^{-(x/l_{sf}^N)} \quad (2.37)$$

and the polarisation of the spin current at the interface is given by

$$\alpha = \frac{P}{1 + (1 - P^2) \frac{\rho^N l_{sf}^N}{\rho^F l_{sf}^F}} \quad (2.38)$$

The solutions to Eq(2.34), Eq(2.35), Eq(2.36) and Eq(2.37) are shown in Fig.2.5 where the region of up-spin accumulation can be seen at the interface. It is observed that, as a result of the unequal spin conductivities within the two materials, as well as the constraint that the spin-dependent electrochemical potentials must be continuous across the interface, a drop in the spin-averaged potential forms ( $\Delta\mu$ ). It can be normalised using  $\vec{j}_c$  to give the spin-coupled interfacial resistance ( $R_S$ ) of the interface

$$R_S = \frac{\Delta\mu}{ej_c} = \frac{P^2 l_{sf}^N \rho^N}{1 + (1 - P^2) \frac{\rho^N l_{sf}^N}{\rho^F l_{sf}^F}} \quad (2.39)$$

### 2.3.5 Pure Spin Currents and Non-Local Devices

The method by which spin diffusion can be induced in a non-magnetic material by spin injection from a ferromagnet was previously shown. One application of this phenomenon occurs in LSVs which work in a similar, albeit significantly distinct, fashion to Fert and Grünberg's spin valves from the 1980s.

LSVs were developed in the early 2000s by two separate teams [12, 13], who took advantage of improvements in the resolution of lithographic techniques to produce new, lateral arrangements of nanoscale wires – as opposed to the vertical stacks built by Fert and Grünberg. Consisting of two horizontal ferromagnetic electrodes bridged by a non-magnetic nanowire (see Fig.2.6), LSVs allow for the generation of clear binary signals which can be manipulated through the application of a small magnetic field. What sets them apart from the original spin valves however, is that the propagation of spins occurs non-locally (that is, separately) to the injected current via a pure spin current.

Because of the lateral arrangement, the charge current required for the spin injection can be directed away from the device's detector. Consequently, the injected current does not pass through the central non-magnetic bridge. However, the spin accumulation at the injection interface still results in an imbalanced spin population (see Fig.2.7), which drives a diffusive spin current throughout the channel and past the detector. Since the

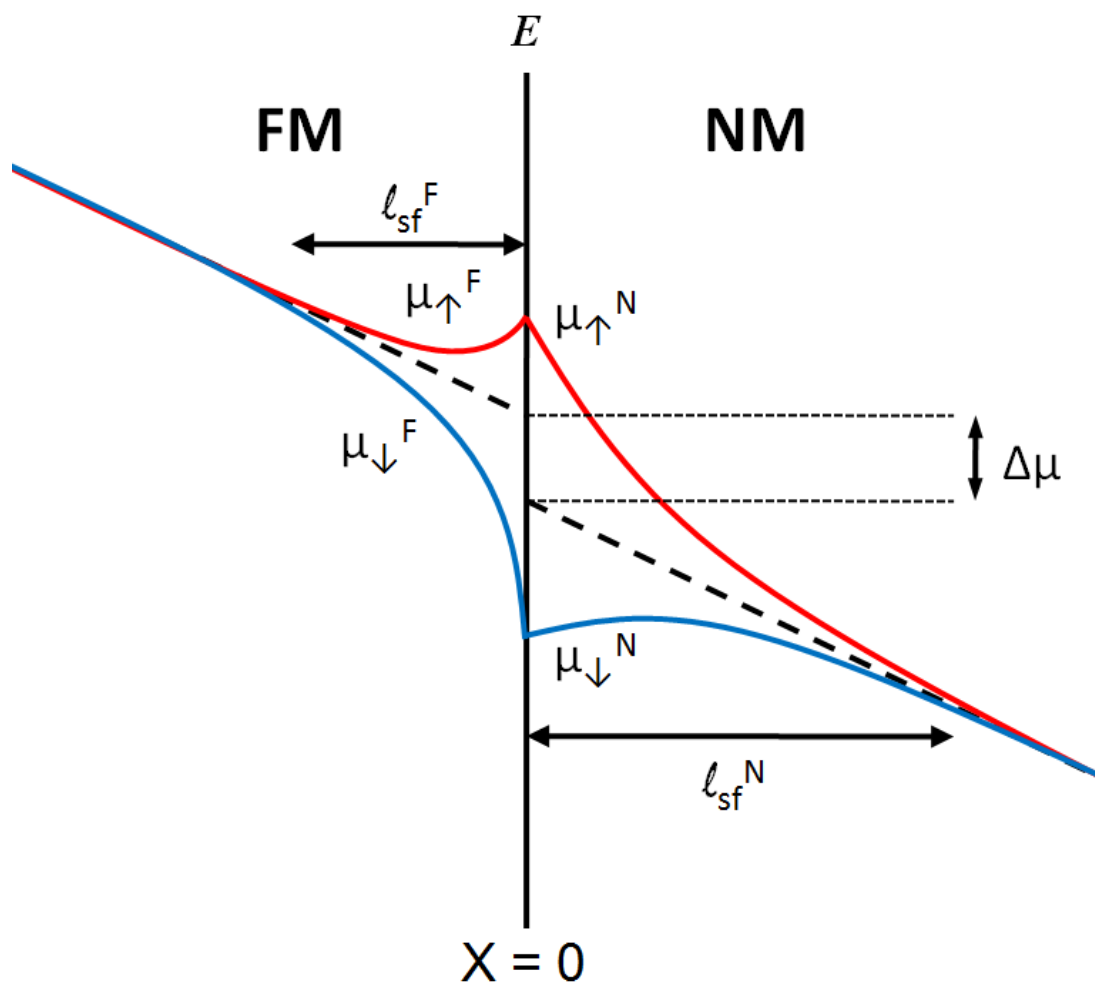


Figure 2.5: An energy diagram of the solutions for a ferromagnet/non-magnet interface undergoing spin injection along the  $x$ -axis. The dashed black line shows the spin averaged  $\mu$ , which is sloped because of the application of  $\tilde{E}$ . At distances far from the interface, the spin-dependent  $\mu$  are equal but they separate at the interface because of the imbalanced spin-dependent  $\sigma$ . The length over which the imbalance in spins protrudes into the two materials is based on their respective  $l_{sf}$ . There is a discontinuity in  $\mu$  at the interface despite the fact that each spin sub-band is continuous.

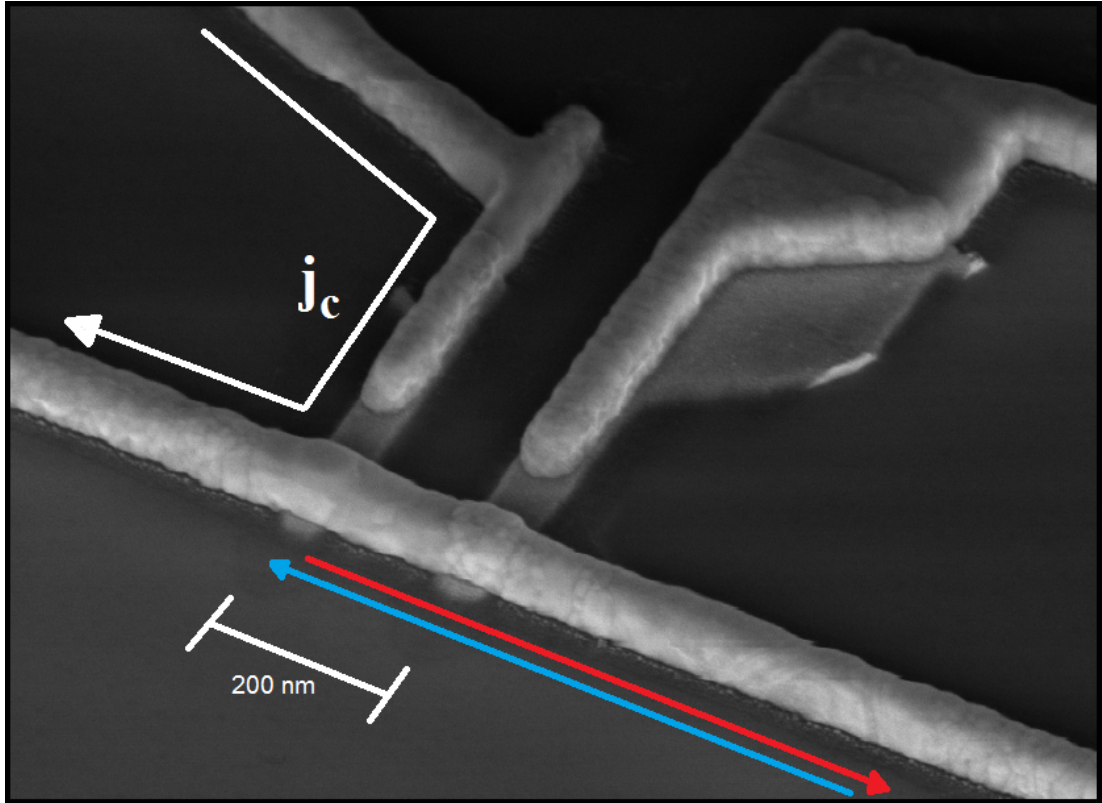


Figure 2.6: A scanning electron microscope (SEM) image of an LSV. The ferromagnetic injector can be seen as a thin strip beneath the thicker (and lighter in colour) non-magnetic material on the left. Meanwhile the ferromagnetic detector, with its large nucleation pad, can be seen beneath the right hand side. The non-magnetic channel connects the two ferromagnetic electrodes with a separation of 200 nm. In order to produce a pure spin current, a charge current must be passed from the injector into the spanning nanowire (indicated by the white arrow). Spin accumulation at the injection interface leads to the propagation of a pure spin current along the device (red and blue arrows). The detector allows for the spin accumulation to be measured as a potential difference, non-locally to the injected current. The devices can be fabricated with the detector positioned at different distances along the non-magnetic channel, which will result in smaller potentials analogous to a stylophone where, by moving the stylyus to different points along the current path, different pitched noises can be made.

overall flow of charge in the central bridge of the non-magnet is zero, while the flow of spins is non-zero, the spin current is said to be ‘pure’ – i.e. it has a polarisation of  $\infty$  (see Eq(2.15)).

As up spins diffuse towards the detector and down spins vice-versa, angular momentum is transferred along the length of the non-magnetic wire without the associated net movement of charges. Pure spin currents offer the unique ability to separate the electron’s spin from its charge [14, 15].

The second ferromagnetic electrode is called the detector because the accumulation of diffusing spins forms a potential difference across its interface with the non-magnet, which can be ‘detected’ as a voltage. The size of the potential difference is dependent on the polarisation of the two spin populations within the non-magnet, at the point of contact with the detector. Therefore, the measured voltage decays exponentially with separation between the two ferromagnets.

Additionally,  $\Delta\mu$  is dependent on the respective direction of magnetisation between the detector and the injector. When aligned parallel to each other, a positive voltage is measured and vice-versa for an anti-parallel alignment (see Fig.2.7). This is because the spin dependent conductivities of the detector are based on its direction of magnetisation. In this regard, LSVs behave similarly to vertically-stacked spin valves. The key difference between the two is that rather than a large change in the measured voltage, its sign is completely flipped in an LSV [11].

In order to be able to magnetically align the two ferromagnets independently, the detector is fabricated with a large nucleation pad included (see Fig.2.6), which allows it to be re-magnetised at smaller magnetic field strengths than the injector [37].

The difference in the signals measured between the two alignments, when normalised to the injection current, is called the spin signal ( $\Delta R_S$ ) and is dependent on: the injection efficiency at the injection interface, the spin diffusion length of the non-magnet relative to the device’s separation and, finally, the detection efficiency at the detection interface.

$$\Delta R_S = \frac{\mu_P - \mu_{AP}}{j_c} \quad (2.40)$$

where  $\mu_P$  and  $\mu_{AP}$  are the potential differences between the detector and the non-magnet for the parallel and anti-parallel states respectively. Solving Eq(2.40) with: Eq(2.34), Eq(2.35), Eq(2.36), Eq(2.37), Eq(2.38) and Eq(2.39) for an injector (F1) and

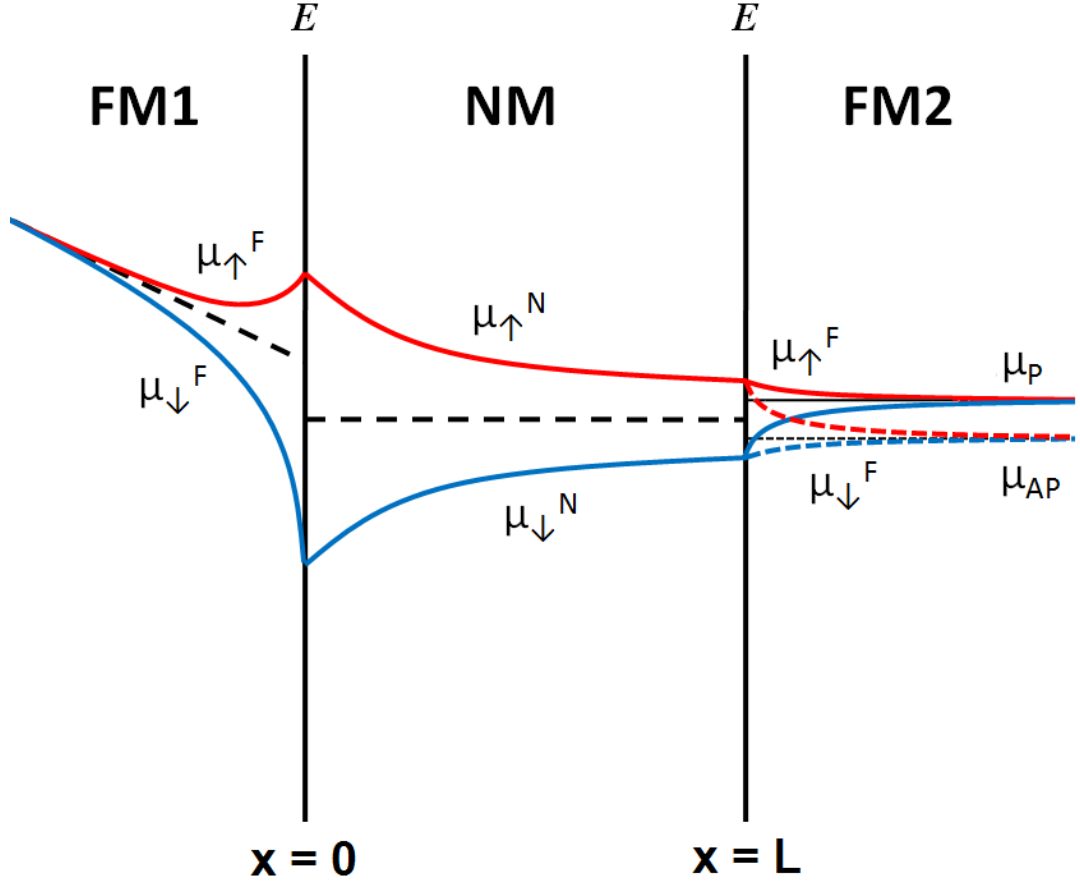


Figure 2.7: The energy diagram for an LSV. On the left hand side, the spin injection from the injector (FM1) is shown as it was in Fig.2.5. However, in this diagram the part of the non-magnet (NM) that is shown instead, is the central bridge – void of the injection charge current; therefore,  $\mu$  is flat. The spin accumulation at  $x = 0$  diffuses throughout the non-magnet and its polarisation decays exponentially with distance because of spin-flip scattering. At the detector (FM2), positioned  $L$  distance away, two scenarios are shown: when FM1 and FM2 are magnetised parallel to each other, the spin-dependent potentials are shown by solid lines; for the anti-parallel alignment, on the other hand, the potentials are represented by dashed lines. In the parallel state, a positive  $\mu_P$  is formed with respect to the non-magnet, while the anti-parallel state results in a respectively negative  $\mu_{AP}$ .

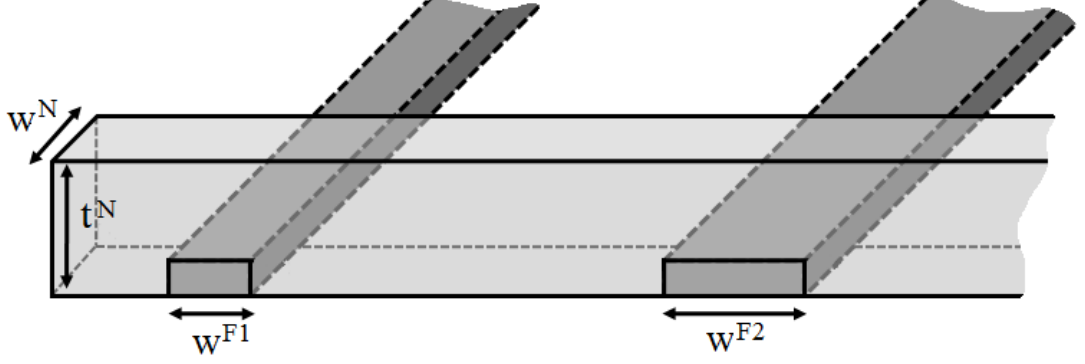


Figure 2.8: A simple schematic of an LSV with the non-magnetic channel (lighter grey) bridging the gap between two ferromagnetic electrodes (darker grey). The dimensions of each of the components have been marked.

detector (F2) positioned a distance  $L$  apart gives the equation that predicts the spin signal measured across an LSV [3, 4, 6]

$$\Delta R_S = \frac{4P^2 R^{F1} R^{F2}}{(1-P^2)^2 R^N} \frac{e^{-L/l_{sf}^N}}{\left(1 + \frac{2R^{F1}}{(1-P^2)R^N}\right) \left(1 + \frac{2R^{F2}}{(1-P^2)R^N}\right) - e^{-2L/l_{sf}^N}} \quad (2.41)$$

where  $R^{F1}$ ,  $R^{F2}$  and  $R^N$  are the ‘spin resistances’ of the injector, detector and bridging channel respectively, given by

$$R^{F1} = \frac{\rho^{F1} l_{sf}^{F1}}{w^{F1} w^N} \quad R^{F2} = \frac{\rho^{F2} l_{sf}^{F2}}{w^{F2} w^N} \quad R^N = \frac{\rho^N l_{sf}^N}{w^N t^N} \quad (2.42)$$

where  $w^{F1}$ ,  $w^{F2}$  and  $w^N$  are the widths of the injector, detector and non-magnetic channel respectively and  $t^N$  is the thickness of the non-magnet (see Fig.2.8).

### 2.3.6 Spin-flip Scattering

The transport of spins within a material is determined by its  $l_{sf}$  which, in turn, is driven by the amount of spin-flip scattering. Every time an electron experiences a scattering event, there is some probability for its spin to be flipped by SOC. One model which describes this mechanism is the Elliott-Yafet model (EY) [23, 38–41], which predicts that the amount of spin-flip scattering is directly proportional to the number of electron scattering events.

$$\frac{1}{\tau_{sf}} = \frac{a}{\tau} \tag{2.43}$$

where  $a$  is the spin-flip probability.

Each of the scattering mechanisms at play within electron transport can contribute to the number of spin-flip events; however, each source of scattering has a different associated spin-flip probability. In combination with Matthiesen’s rule, this gives [2]

$$\frac{1}{\tau_{sf}} = \frac{a_0}{\tau_0} + \frac{a_e}{\tau_e} + \frac{a_{ph}}{\tau_{ph}} \tag{2.44}$$

where  $a_0$ ,  $a_e$  and  $a_{ph}$  are the spin-flip probabilities for non-magnetic impurity, electron-electron and electron-phonon scattering events respectively. It should be noted that it is customary to combine the electron-electron and electron-phonon interactions into one term –  $a_{ph}$ .

The EY model assumes that within a material there is: i) inversion symmetry, ii) weak SOC and iii) a low phonon scattering rate [42]. Effectively, the relationship usually holds for well ordered metals [2, 38, 43] however, the model can begin to break down when the amount of scattering increases.

Elliott-Yafet scattering is based on the idea that when an electron experiences SOC in a material, the lattice potential leads to mixing between the separate spin-state wave functions. Because of inversion symmetry, the two different spin-states of the electron can easily transition between each other during the scattering events outlined before with regards to Fermi’s golden rule (with a transition probability of  $W_{\uparrow \rightarrow \downarrow}$  or  $W_{\downarrow \rightarrow \uparrow}$ ). As such, each electron scattering event provides a set probability for the spin-state to change. Elliott predicted that for  $L/\delta(\epsilon_f - \epsilon_i) \ll 0.1$ , the spin-flip probability would remain temperature independent, where  $L$  is the orbital angular momentum of an electron.

If inversion symmetry is broken within the material, then other spin-flip scattering mechanisms such as D’Yakonov-Perel take over in which the electrons’ spins fall out of phase with each other. In semiconductors, other spin-flip mechanisms such as the Bir-Aharonov-Pikus effect become prominent.

An important distinction to make with regards to spin-flip scattering is that the  $l_{sf}$  is not the same as the average distance individual electrons can travel before their spins are flipped [35], which is described by the spin-flip length ( $\lambda_{sf}$ ) – related to  $\lambda$  through the EY relationship

$$\lambda_{sf} = \frac{\lambda}{a} \quad (2.45)$$

$l_{sf}$  is instead better thought of as the length scale over which non-equilibrium spin populations can generally diffuse, before spin-flip scattering renders them equilibrated.

For example, in previous studies of Ag,  $l_{sf}$  has been measured to be between 500 and 1000 nm [4, 44] while the electrical mean free path of the Ag was found to be of the order of 100 nm [4]. With reported values of a spin-flip probability of 0.2% [44], the spin-flip length for the individual electrons is predicted to be of the order of 50,000 nm – over 100 times further than the spin diffusion length of the electron population. In Cu, similar length scales have been observed, with reported  $l_{sf}$  values between 300 and 1000 nm [2, 3, 6] and spin-flip probabilities of 0.1% [2].

## 2.4 Thermoelectric Effect

As well as voltages arising from the diffusion of spins through an LSV, there are also a number of thermal effects at play which can contribute to the signals measured at the detector. It is important to the understanding of pure spin currents to be able to distinguish these thermal voltages from the spin related signals and multiple studies have attempted to do so [1, 4, 6, 45–48].

Whenever an electrical current is passed through more than one type of adjacent metal, a thermocouple (electrical thermometer) is created, with various contributions to the overall thermoelectric effect. The two main phenomena that affect the temperature within an electrical circuit are Joule heating and the Peltier effect, which both produce thermal gradients that generate potential differences via the Seebeck effect.

### 2.4.1 Joule Heating

When an electric field is applied across a material and current begins to flow, the conducting electrons experience two distinct types of scattering events: elastic and inelastic collisions. Elastic scattering describes events in which the overall kinetic energy of the two colliding parties remains the same after their interaction.

Picture two particles in an idealised situation, colliding head-on and then rebounding with the same speeds at which they initially collided. Because of the principle of

the conservation of energy, there can have been no energy transferred to the environment. Likewise, for elastically scattering electrons, kinetic energy supplied by the applied electric field is not transferred to the crystal structure of the material.

With inelastic scattering however, some of the kinetic energy of the electrons is lost to the crystal lattice in the form of heat – known as Joule heating [25]. The more inelastic scattering, the more heat dissipation; hence, when an electrical current is passed through a resistive element, it heats up. The average amount of energy dissipated by each electron as it passes through a resistor is approximated by the voltage drop along the current path. To calculate the rate of energy dissipation the flow rate of the charges needs to be taken into consideration giving

$$\dot{Q} = I\Delta V \quad (2.46)$$

where  $\dot{Q}$  is the rate of heat transfer to the crystal lattice,  $I$  is the current and  $\Delta V$  is the change in potential across the material. For a purely Ohmic resistor (a valid assumption for most metals) this becomes [49]

$$\dot{Q} = I^2 R \quad (2.47)$$

where  $R$  is the electrical resistance experienced along the current's path.  $R$  is related to  $\rho$  geometrically

$$\rho = \frac{AR}{L} \quad (2.48)$$

where  $L$  is the length of the current path and  $A$  is its cross-sectional area.

For small enough currents, the amount of Joule heating reaches equilibrium via heat dissipation to the surrounding environment and thus the temperature of the material does not increase indefinitely. In an LSV, Joule heating occurs everywhere the injection current passes through. Because the pure spin current in the central bridge possesses a net flow of charge equal to zero, it has been hypothesised that Joule heating does not arise in the region of spin diffusion between the injector and detector [16–18].

As can be seen in Eq(2.48),  $R$  is largest for features with small cross sectional areas. The narrowest part of the current path in an LSV is within the thin ferromagnetic injector; hence, the most Joule heating occurs there, creating a hotspot at the spin injection interface. This was confirmed experimentally by Stefanou et al. when they thermally imaged an LSV during spin injection, using a specially converted scanning thermal microscope (SThM)[4].

### 2.4.2 Peltier Effect

Electrons flowing through a metal possess kinetic energy which they can dissipate as heat into the surrounding structure through inelastic scattering. If a current is passed from one conductor into another, an additional mechanism occurs at the interface between the two [25], called the Peltier effect [50].

It was previously described how electrons close to  $E_F$  in a conductive metal receive small amounts of kinetic energy from an applied electric field, which allows them to move freely. Different metals however, have different Fermi energies. As a result, when electrons flow from one material into another they either possess more kinetic energy than the surrounding electron population, or less – depending on the relative  $E_F$ . Consequently, they will, statistically speaking, experience many more inelastic scattering events in the region of the interface, in order to bring their kinetic energy in line with that of the new material's  $E_F$ .

For electrons passing into a material with a lower Fermi energy, their extra kinetic energy will be dissipated into the lattice as heat and the interface will warm up. Conversely, for those flowing into a material with a larger Fermi energy, energy will be absorbed from collisions with the surrounding energetic phonons, cooling the crystal's structure – a phenomenon that is exploited widely in Peltier coolers. For a current passing from material A into material B, the rate of energy change at the interface is given by

$$\dot{Q} = I(\Pi_A - \Pi_B) \quad (2.49)$$

where  $\Pi_A$  and  $\Pi_B$  are the Peltier coefficients for the two respective materials, which are a measure of the amount of kinetic energy held, on average, by each conducting electron. In an LSV, the Peltier effect can effectively be assumed to only occur significantly in one region (assuming interfaces between the device and its electrical contacts are too far away to have any meaningful effect) – at the injection interface.

### 2.4.3 Seebeck Effect

When an electrical circuit warms up, the electrochemical potential of the conducting electrons is increased via inelastic scattering with phonons. It follows that, along any temperature gradient across a material, a potential difference will also form. This is

known as the Seebeck (or thermoelectric) effect [25] and it is found in the electrical measurements of any device with thermal gradients across it. It is described by

$$\nabla V = -S\nabla T \quad (2.50)$$

where  $\nabla V$  is the gradient in potential,  $S$  is the Seebeck coefficient of the material and  $\nabla T$  is the gradient in temperature.

In a paper by Stefanou et al. a simple model was introduced to explain the magnitude of the thermoelectric effect measured at the detector within LSVs, that was caused by both Peltier and Joule heating at the injection interface [1]. It is of importance to this study to present a step-by-step work-through of the model so that a comparison can be made to the thermal signals presented in later chapters.

Initially, the model outlines the temperature gradient across an element of the central channel in an LSV of length  $dx$ . For a volume of wire between lengths  $x$  and  $x + dx$ , with a width  $w$  and thickness  $t$ , in thermal equilibrium, the flow of heat into the element ( $\dot{Q}_{in}$ ) is equal to the sum of the flows of heat out of the element.

$$\dot{Q}_{in} = \dot{Q}_{sub} + \dot{Q}_{out} \quad (2.51)$$

where  $\dot{Q}_{sub}$  represents the heat lost to the substrate and  $\dot{Q}_{out}$  is the flow of heat into the wire beyond  $x + dx$ . It is assumed that the heat flow into the atmosphere surrounding the wire is negligible because the thermal conductivity of the gas is significantly lower than that of the condensed matter.

The heat flow into the element is given by the conductivity equation:

$$\dot{Q}_{in} = -2\kappa wt \frac{dT}{dx} \quad (2.52)$$

where  $\kappa$  is the thermal conductivity of the material making up the wire,  $dT/dx$  is the gradient in temperature with respect to distance along the wire and the factor of two comes from the fact that the heat generated at the injector propagates in two directions away from the junction.

Heat loss to the substrate is described by the thermal conductance of the wire/substrate interface ( $K$ ) and the area of contact between the two ( $w \times dx$ ).

$$\dot{Q}_{sub} = (T(x) - T_{sub}) K w dx \quad (2.53)$$

where  $T(x)$  is the temperature of the wire element and  $T_{sub}$  is the temperature of the substrate.

$\dot{Q}_{out}$  is equal to the heat flowing into the next volume element along the wire and so can be written as

$$\dot{Q}_{out} = \dot{Q}_{in}(x + dx) = \dot{Q}_{in} + \frac{d\dot{Q}_{in}}{dx}dx \quad (2.54)$$

which, in combination with Eq(2.51) and Eq(2.53) gives

$$\dot{Q}_{in} = \dot{Q}_{in} + \frac{d\dot{Q}_{in}}{dx}dx + (T(x) - T_{sub})Kwdx \quad (2.55)$$

Eq(2.52) can be differentiated with respect to  $x$  and substituted into Eq(2.55) to give

$$\frac{d^2T}{dx^2} = \frac{Kw}{2\kappa wt}(T(x) - T_{sub}) \quad (2.56)$$

which can be rewritten as

$$\frac{d^2T'}{dx^2} - \frac{1}{l_{th}^2}T' = 0 \quad (2.57)$$

where  $T(x) - T_{sub}$  has been replaced with  $T'$  and  $l_{th}$  is the thermal diffusion length along the wire, equal to

$$l_{th} = \sqrt{\frac{2\kappa t}{K}} \quad (2.58)$$

By introducing boundary conditions to Eq(2.57), general solutions can be obtained. It is assumed that at  $x = \infty$ ,  $T = T_{sub}$ . Additionally, the temperature at  $x = 0$  is labelled as  $T_{inj}$  (the injector's temperature) giving the temperature at each point along the central channel as

$$T(x) = T_{inj}e^{-x/l_{th}} + T_{sub} \quad (2.59)$$

When measuring LSVs the temperature cannot be directly observed (Stefanou's SThM experiment being the exception [4]). Instead, the Seebeck voltages measured across the detector need to be converted into effective temperatures using Eq(2.50).

Stefanou demonstrated with their thermal imagery of an LSV in operation, that the temperature at the end of the detector furthest from the central channel was negligibly

different to that of the substrate. Therefore the Seebeck voltage across the detector can be assumed to arise in the difference between  $T_{\text{sub}}$  and the temperature of the central channel at the detector's interface ( $T_{\text{det}}$ ).

A voltage measurement is performed by attaching the positive and negative terminals of a voltmeter to either end of the ferromagnetic detector, which can be represented by

$$\mu^+ - \mu^- = |e| \left( \int_{T_{\text{det}}}^{T_{\text{sub}}} S^N dT + \int_{T_{\text{sub}}}^{T_{\text{det}}} S^{F2} dT + \int_{T_{\text{sub}}}^{T_{\text{sub}}} S^N dT \right) \quad (2.60)$$

where  $\mu^+$  and  $\mu^-$  are the potentials at the positive and negative terminals of the voltmeter respectively,  $e$  is the charge of an electron and  $S^N$  and  $S^{F2}$  are the Seebeck coefficients for the respective nonmagnetic and ferromagnetic materials.

The first integral in Eq(2.60) represents the Seebeck voltage arising due to the temperature gradient between the detector's interface and the positive terminal of the voltmeter (through the nonmagnetic material). The second describes the Seebeck effect due to the temperature gradient across the ferromagnetic detector itself and finally, the third term represents the voltage generated between the far end of the detector and the negative terminal of the voltmeter.

Eq(2.60) can be simplified to

$$\Delta V = (S^N(T_{\text{sub}}) - S^F(T_{\text{sub}}))(T_{\text{det}} - T_{\text{sub}}) \quad (2.61)$$

or more simply

$$\Delta T = \frac{\Delta V}{\Delta S(T)} \quad (2.62)$$

where  $\Delta T$  is the difference in temperature between the substrate and the detector's interface with the central channel,  $\Delta V$  is the total Seebeck voltage measured across the detector and  $\Delta S(T)$  is the difference in Seebeck coefficient between the nonmagnetic and ferromagnetic materials at the temperature of the substrate.

---

# CHAPTER 3

---

Methods

The following sections describe the processes required to fabricate, then measure the LSVs studied in this thesis. The distances over which spin diffusion takes place are typically very small (of the order of 1  $\mu\text{m}$ ); hence, it is necessary to produce LSVs at the nanoscopic scale. One of the most reliable methods to produce such small, precise metal features is to evaporate material onto a finely detailed stencil (called a template) placed on top of a substrate material. By carefully removing the template through a suitable process, the desired pattern of metal can be achieved.

LSVs need to be connected electrically to the relevant measurement instruments in order for their spin and thermal transport properties to be studied. Furthermore, the measurements need to be performed for a wide range of controlled variables so that a greater understanding of the mechanisms at play within them can be achieved; these measurements will also be explained in the coming sections.

### 3.1 Sample Fabrication

Three key problems confront the fabrication of LSVs that can produce large, low-noise spin signals. Firstly, a large amount of spin injection is necessary which requires that the size of the injection interface be as small as possible (see Eq(2.42)). This can only be achieved with very advanced lithographic techniques to produce a template with nanoscopic features.

Secondly, the interfaces within the devices themselves need to be very ‘clean’. That is, they should be as void of oxides and other impurities as possible. The most effective way to ensure a non-oxidised surface between two metals is to deposit them on top of each other under ultra-high vacuum (UHV) conditions. When fabricating stacked devices this is a relatively simple process but for lateral configurations it becomes significantly more difficult. One solution, called ‘shadow deposition’, involves varying the angle at which the metals are evaporated relative to the template [51].

Finally, because of the exponential decay of  $\Delta R_S$  with distance, a non-magnetic channel with a long  $l_{sf}$  is desirable. Therefore, the deposition of the non-magnet needs to be performed in such a way as to minimise sources of scattering within. This is achieved by combining a high-quality source material (six 9s) with extremely low background pressures during deposition ( $\sim 1 \times 10^{-9}$  mbar). As a result, the production of LSVs is a complicated and time-consuming process and the fabrication and methodology need to be strictly controlled.

### 3.1.1 Substrate Preparation

The following methodology was developed by: Dr Joe Batley [5], Dr Mark Rosamond, Dr Gavin Burnell, Dr Georgios Stefanou [4] and Dr Kathryn Moran [6]. Si wafer disks with a thermally oxidised surface ( $\text{SiO}_2$ ) were chosen as the substrates for the devices because of their electrically and thermally insulating properties. The wafers were initially cleaned by sonication: firstly in acetone and then in isopropyl alcohol (IPA). Afterwards, they were blown dry with  $\text{N}_2$  gas and, finally, baked dry at  $180^\circ\text{C}$  on a hotplate.

The entire fabrication process up until the final shadow deposition was undertaken in a clean room environment (ISO 5 - Class 100) in order to minimise the risk of contaminants adhering to the samples during preparation. Furthermore, carbon-tipped tweezers were used whenever handling of the wafers was required, to prevent magnetic contamination of the samples.

The first step in preparing the wafers for the addition of LSVs was to add electrical contacts which would allow for connection to external measurement instruments. The two crucial characteristics for the electrical contacts were that they needed to be highly conductive and capable of bridging the nanoscale LSVs with the macroscopic electrical equipment. Because of its great conductivity and resistance to oxidation, Au was chosen.

In order to overcome the difficulty of connecting the nanoscale devices to the much larger electrical equipment, the contacts were fabricated in two separate stages: smaller inner contacts and large outer ones. One of the main reasons for separating the process into two steps was that the lithography required for the nanoscopic end of the contacts would have taken days to complete the larger ends.

### 3.1.2 e-Beam Lithography

e-beam lithography is the process of using finely-tuned beams of electrons, with very specific energies, to weaken the chemical bonds within organic molecules at a nanoscopic scale. The organic molecules used are called ‘resists’, which are stored in solution and then ‘spun’ onto the substrate to form a layer of constant thickness. The speed of the spinning process, as well as the viscosity of the resist’s solvent, can be finely tuned to control the thickness of the organic layer. e-beam lithography is the most reliable way to produce the required nanoscopic templates for LSV fabrication.

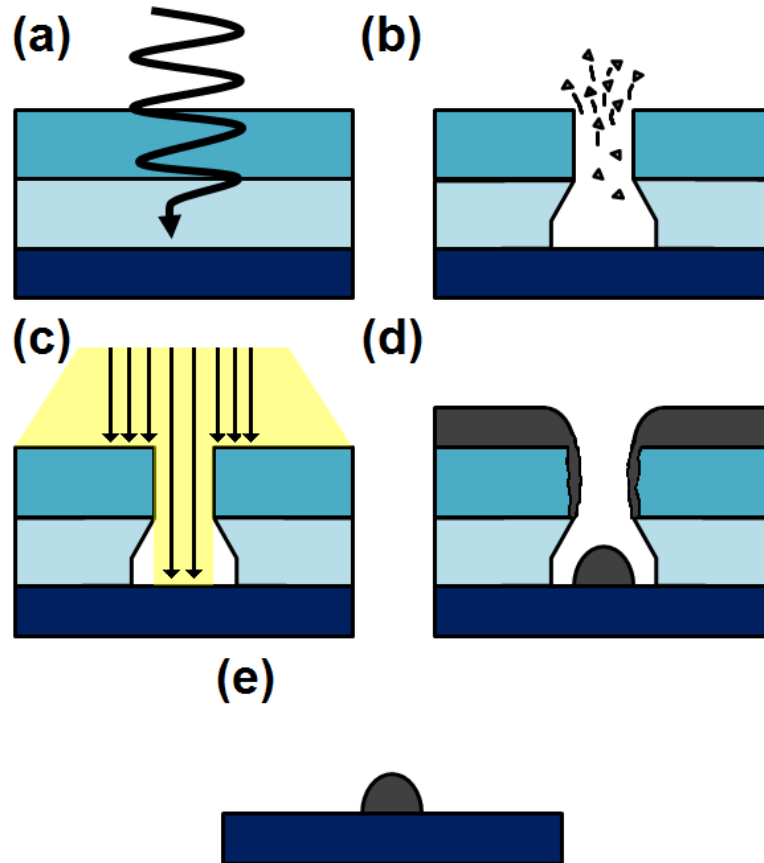


Figure 3.1: A simple schematic of the process of e-beam lithography and then deposition onto a bi-layer of resists. **(a)** The bottom dark blue layer is the  $\text{SiO}_2$  surface, above which are the two different layers of resists stacked on top of each other. The black arrow represents exposure to the focused e-beam. **(b)** The resist is immersed in a ‘developer’, a solvent that only acts on resist with weakened bonds. A larger volume of the bottom layer of resist is dissolved because it is more sensitive to the e-beam. **(c)** The patterned bi-layer is then exposed to the evaporation of a desired material. The undercut in the bilayer results in a ‘shadow’ from the depositing material. **(d)** Afterwards, the metal (dark grey here) will have coated the top of the template, as well as depositing into the exposed area. There is often also material lining the side of channels cut into the resist – referred to as ‘sidewall deposition’. **(e)** The template is then removed by exposing it to a strong solvent. The material on top will be removed along with it, leaving behind only the desired pattern of metal.

For this study, e-beam lithography was performed on a bi-layer of resists: methyl-methacrylate (MMA) beneath poly(methyl-methacrylate) (PMMA). Prior to the addition of the bi-layer, hexa-methyldisilazone (HMDS) was spun onto the baked Si substrate at 4000 rpm for 40 s to help improve the adhesion with the other resists. Any excess primer was then rinsed off with IPA followed by N<sub>2</sub> gas and then the wafer was baked at 180°C for 1 minute resulting in a hydrophobic monolayer of primer on top of the SiO<sub>2</sub>.

Following the primer, the MMA (which was dissolved in methacrylic acid [MAA] at a ratio of 40/60) was spun onto the substrate at the same rotational speed and for the same amount of time. It was then baked at the same temperature, for the same amount of time as the HMDS. Afterwards, the PMMA (PMMA 950k A4) was added using identical parameters. Each layer of resist was spun in such a way as to achieve approximate thicknesses of 500 nm and 250 nm – for the bottom and top layers respectively [4, 6].

The resist was then patterned in a JEOL JBX-6300FS e-beam lithographer, using a template designed in K-Layout graphical software. The operation of the JEOL was performed by Dr Rosamond [52].

A bi-layer was used because the MMA is about ten times more sensitive to the e-beam than the PMMA, which results in an undercut forming in the patterned regions. An undercut allows for a much more reliable deposition because it creates a physical disconnect between material evaporated into the desired area and the stencil itself (see Fig.3.1(d)). When the template is afterwards removed, it is less likely to ‘rip’ the deposited material off with it.

After patterning, the resists were developed in a solution of IPA/H<sub>2</sub>O (at a ratio of 70/30) which dissolved the weakened regions of resist, revealing the patterned design. The wafer was then washed in pure IPA to prevent over-development, ensuring the features remained small and defined. Finally, the wafer was placed in an O<sub>2</sub> plasma asher for 40 s at a power of 50 W to remove any last remaining islands of undissolved resist.

#### 3.1.3 Electrical Contacts

Once e-beam lithography was performed to produce the template for the inner contacts, the wafer was loaded into a Oerlikon Univex 350 e-beam evaporator. The chamber was

pumped down for one hour in order to reach a pressure of  $\sim 1 \times 10^{-6}$  mbar. The pressure during deposition of the electrical contacts is less critical than for the spin valve's materials because any scattering within the Au is discounted from the final measurement.

e-beam evaporation works by accelerating a stream of high-energy electrons with an electric field and then directing it into a target mass of metal using magnetic fields to control the beam. The electrons impart their kinetic energy onto the target, rapidly increasing its temperature. With enough applied power, the source material melts which, in the confines of a vacuum, results in a constant but gradual evaporation of the material into the chamber. Because of the low pressures involved, the evaporated material is assumed to travel in a straight line in all directions emanating from the melted source; coating most surfaces within the evaporation chamber.

For the contacts, 5 nm of Cr was initially evaporated because it adheres to the SiO<sub>2</sub> surface much better than Au. Following this, 30 nm of Au was e-beam evaporated; the very small thicknesses were required so that when the actual devices were added later, the nanowires could overlap the ends of the contacts for good electrical continuity (see Fig.3.2).

Post-deposition, the resist template and excess metal (see Fig.3.1(d)) were removed with acetone through a process called 'lift-off' – which dissolves the bi-layer of resists. The material coating the top and sides of the bi-layer was removed when the resist dissolved, leaving behind only the material in the patterned regions (Fig.3.1(e)). The acetone was then rinsed away with IPA and the wafer was blown dry with N<sub>2</sub> gas.

Occasionally, during lift-off, some of the sidewall deposition can fall away from the resist and land on top of patterned material below. This can subsequently lead to issues with the devices later down the line and a key challenge to LSV fabrication is in the reduction of such sidewall re-deposition.

Once the inner contacts were fabricated, the template for the larger outer contacts was added; because of the amount of time it takes the JEOL to pattern even nanoscale designs, optical lithography was used instead. The wafer was again placed in the O<sub>2</sub> plasma asher removing any remaining resist from the previous lift-off. Afterwards, the sample was dehydrated on a hotplate at 200°C.

For the optical lithography, photosensitive resists were instead required for the bi-layer. The underlayer was made from a resist called LOR 3A which was spun on at

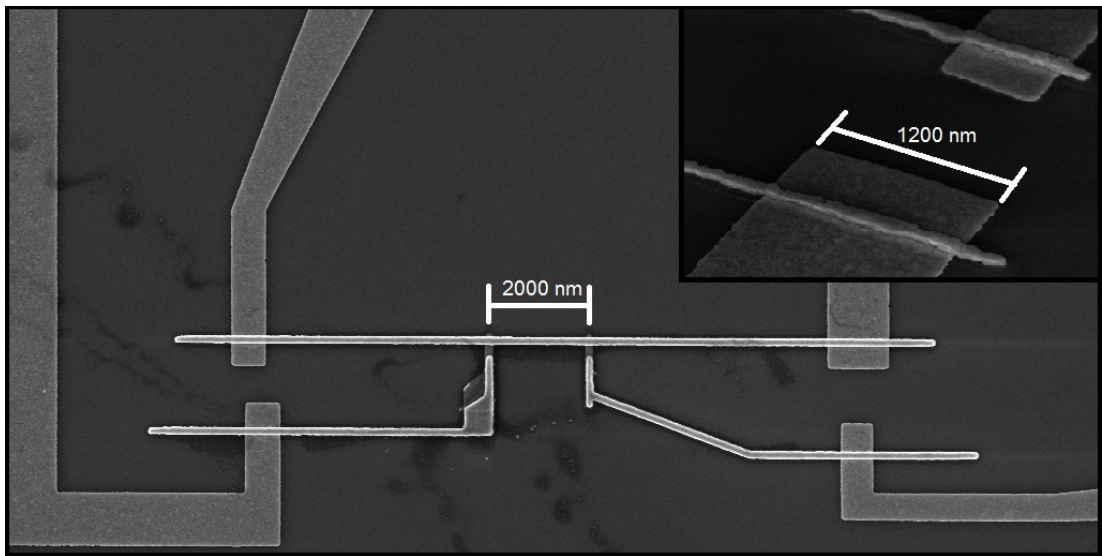


Figure 3.2: An SEM image of a fully fabricated LSV. The non-magnetic material shows up as the lightest coloured wires in the image. The Au inner contacts are the wider features positioned beneath each of the device's four ends. The separation between the injector and detector has been marked. The inset shows a closer, angled inspection of one of the arms overlapping the thinner Au inner contact - including the width of the contact's end.

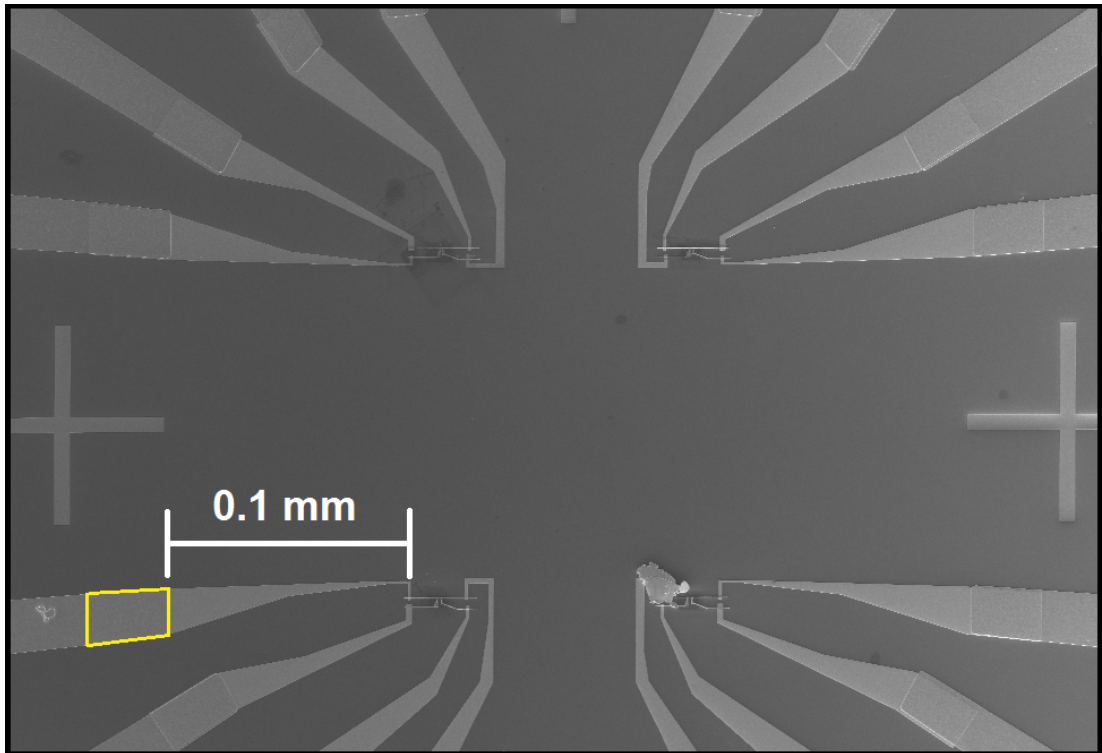


Figure 3.3: An SEM image of an array of four LSVs, each device with four contacts. The inner contacts form the narrow ends which converge at the devices while the outer contacts can be seen overlapping them further out. One of the points of overlap has been highlighted in yellow in the bottom left to give a better sense of the contact area. The large crosses seen at the left and right-hand sides of the image are guide marks for the JEOL to align to. On the bottom right device, it can be seen that a large flake of material has landed on top – rendering it immeasurable. This is just one of the many pitfalls that arises during fabrication.

the same speed and for the same time as in previous steps. The LOR 3A was then baked at 200°C for 5 minutes to remove any remaining solvent. Finally, S1813 resist was spun on top of the LOR at the same speed and for the same amount of time, in order to complete the bi-layer with similar approximate thicknesses as those achieved for the e-beam lithography; it was also baked, but only at 111°C for 3 minutes.

After the addition of the optically sensitive bi-layer, the wafer was placed into a Karl Suss optical mask aligner and exposed to ultra-violet (UV) radiation with a dose of  $26.2 \pm 0.1 \text{ mJ cm}^{-2}$  for 3.5 s. A specially made glass mask (designed by Dr Stefanou) was positioned between the UV source and the bilayer, ensuring that only the desired regions of resist were exposed to UV light. The advantage of optical lithography is that the entire pattern is exposed at once – drastically decreasing the time required; however, because the wavelength of UV light is so much longer than that of the electrons typically used in lithography, the size of the smallest features that can be patterned are an order of magnitude larger.

After exposure to UV light the mask was removed and the resists were developed in a solvent called MF319 to remove the exposed material, thus revealing the channels for the outer contacts. The wafer was rinsed in de-ionised water and then blown dry to avoid over-development. It was then, again, placed into the O<sub>2</sub> plasma asher to remove any lingering resist from the developed regions.

Because they were so much larger, the outer contacts were deposited through a process called sputtering instead of evaporation. Sputtering is a much faster process than evaporation but can result in ‘blotchy’ edges on nanoscale features. It involves bombarding a target plate of material with high energy plasma, which causes ‘chunks’ of the target to be ejected and, because of the low pressure in the sputtering chamber, move unimpeded towards the patterned template.

For the outer contacts, a Kurt J. Lesker PVD75 sputter coater was used. It was pumped down to a vacuum of  $\sim 1 \times 10^{-5}$  mbar before a pre-deposition etch was performed using the Ar plasma at a power of 50 W for 1 minute. 5 nm of Cr was then sputtered, followed by 50 nm of Au, thus completing the outer contacts. They were made thicker so that they fully overlapped the inner contacts (see Fig.3.3) resulting in a continuous electrical connection.

The lift-off process for the optical lithography was performed with the solvent N-Methyl-2-pyrrolidone (NMP), warmed to 75°C, followed by an additional exposure to

O<sub>2</sub> plasma after which the wafer, with both sets of electrical contacts, was completed.

Finally, e-beam lithography was again performed: this time in order to pattern the actual LSVs themselves. The only difference to the process for the inner contacts was the inclusion of an additional reactive-ion (RF) etch in Ar plasma (done in the sputterer), post-development, to ensure as clean a substrate surface as possible.

It should be noted that batches of prepared templates were produced by, and shared between Dr Stefanou, Dr Moran and the author of this thesis.

### 3.1.4 Shadow Deposition

Once the wafers had been prepared for the deposition of the actual devices, they were transferred into a bespoke shadow deposition chamber (see Fig.3.4) built by Dr Mannan Ali, Dr Burnell and Prof Bryan Hickey, later reconfigured by Dr Batley and then even more recently by the author of this thesis. The substrate was attached to a brass mounting plate with Kapton tape and then loaded into the system via a load-lock which allowed for the base pressure to be maintained. Once the load lock had been pumped down using a turbo pump, the samples were loaded into the main chamber using the transfer arm.

The base pressure on the day of deposition was enhanced by adding liquid nitrogen to a cryotrap positioned just behind the sample stage, which allowed for the diffusion pump to maintain pressures as low as  $1 \times 10^{-10}$  mbar during metallic evaporation. The cryotrap was also heat-sunk to the sample stage with copper braid in an attempt to keep the sample as cool as possible during deposition.

The technique of shadow deposition allows for the evaporation of two different metals onto a single template in such a way that two different patterns are formed. This is vital for LSVs because, otherwise, each metal would have to be grown using a separate template, which would necessitate exposure to atmospheric conditions and, thus, result in an oxidised interface between the two.

The bespoke deposition chamber was built with a 3-axis rotational sample mount which allowed for complete control over the orientation of the substrate with respect to the different evaporation sources, essential for shadow deposition. By carefully altering the angle of evaporation of the two different metals, in combination with a specially designed undercut template, the lateral arrangement required for LSVs could be deposited over the course of a few hours. The process is most easily explained with the aid

of a diagram (Fig.3.5). A comparison can be made with Fig.2.6, where the thin strips of ferromagnet lie beneath the thicker, non-magnetic wires.

Once the template was in place and the lowest possible pressure reached, the ferromagnetic material was evaporated via e-beam evaporation from a water-cooled copper hearth at an angle of  $45^\circ$  to the wafer. The substrate was aligned to the deposition source using a geared sample-stage control and pre-calibrated marks indicating the relative angles between components within the deposition system (see Fig.3.5.C). However this introduced a fair amount of uncertainty to the exact angle of deposition because of the rough teething in some of the alignment grooves.

Because of the angled nature of the deposition, 35 nm of material had to be evaporated in order to achieve the desired 25 nm thick features on the substrate. A previously calibrated crystal monitor (positioned in-situ) was used to ensure the right amount of material was deposited.

Following the deposition of the ferromagnets, the wafer was re-aligned perpendicular to the non-magnetic evaporation source. 100 nm of material was then deposited via thermal evaporation from a BN crucible inside a thermal effusion cell (also known as a Knudsen cell).

Once both evaporations were completed, the wafer was unloaded from the chamber and a lift-off was performed in  $55^\circ\text{C}$  acetone in the clean room. Colder acetone results in a much slower and less reliable lift-off because the resist comes away from the substrate less cleanly. After the lift-off, the samples were then coated in a protective layer of PMMA in order to slow the rate of oxidation in atmospheric conditions. For such small metal features, the surface to volume ratio is very large and as a result, moisture in the air very readily attacks the devices' junctions.

## 3.2 Electrical Measurements

### 3.2.1 Setup

The wafers were designed in such a way that 36 individual LSVs were arranged across the substrate. Each device had a unique injector-detector separation (ranging from 500 nm to 4000 nm) and its own individual set of electrical contacts (see Fig.3.3).

After fabrication, the wafer was stuck down to a brass measurement mount (built by Dr Ali) using conductive Ag lacquer, which electrically and thermally grounds the

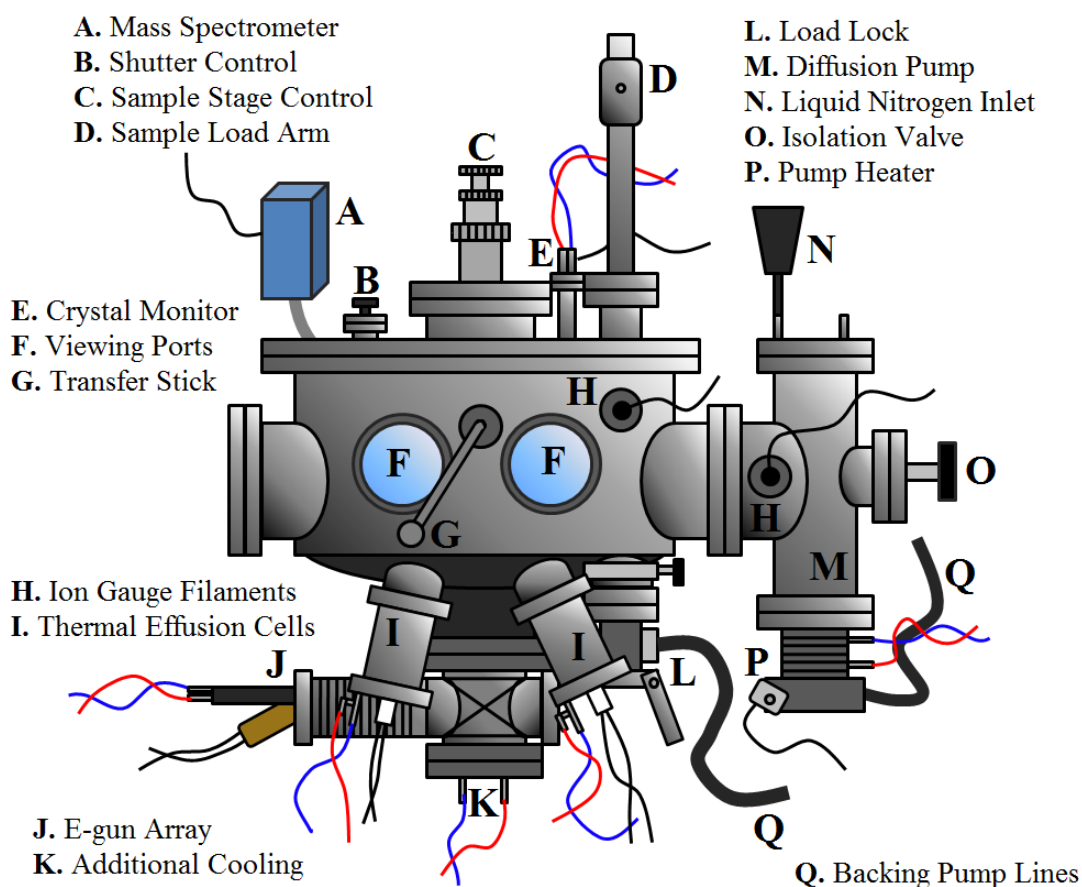


Figure 3.4: A crude sketch of the bespoke deposition chamber used to perform the shadow deposition required to fabricate the LSVs. The blue and red lines are the water-in and water-out lines for the water cooling system. The thin black lines represent electrical connections to the control system.

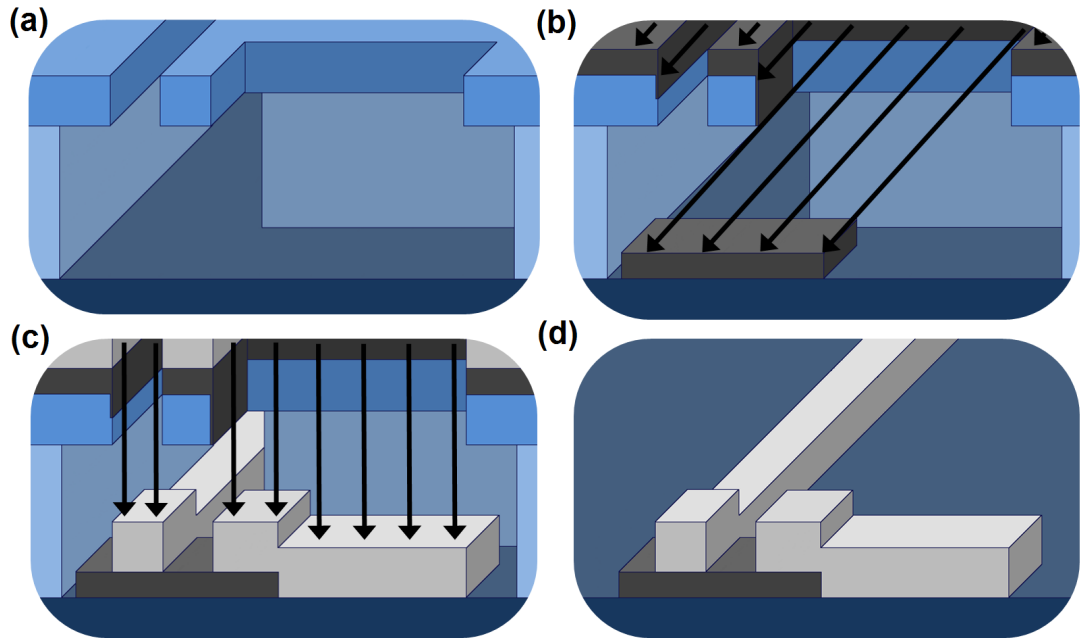


Figure 3.5: A simple illustration of the process of shadow deposition – here shown as a cut-away cross section at the site of the injector. **(a)** The pre-prepared template on top of the substrate (dark blue). The bottom layer of resist (light blue) has been removed to a greater degree during development forming an undercut below the top layer (mid-blue). **(b)** The ferromagnetic material (dark grey) is deposited at an angle of  $45^\circ$  to the substrate. Because of the geometry of the template it cannot reach the substrate in the central channel and deposits onto the top and side of the resist. To compensate, an extra slot is included to the right, which allows the ferromagnetic material to deposit in a thin strip where the injector is desired. **(c)** The substrate is then rotated perpendicular to the evaporation source and the non-magnetic material (light grey) is deposited, allowing it to form in the central channel. The gap between the two non-magnetic structures forces electrical current to pass through the ferromagnetic layer which allows for the spin injection. **(d)** Finally, the substrate is submerged in a strong solvent which removes all the resist and any material deposited on top, leaving only the desired metal nanostructure. The connecting Au electrical contacts have not been included in this diagram for simplicity.

substrate. Brass was used because of its high thermal conductivity and the mount was purposefully made as heavy as possible to increase its thermal mass – for better temperature stability.

The brass mount had 8 low-resistance wires connected to pads that were positioned around the mounting site. As a result only two devices could be electrically connected to the measurement array at the same time (4 contacts each). A calibrated CERNOX resistor was also included on the mount, which enabled real time temperature measurements.

Each device’s outer contacts were connected to the brass pads using a Kulicke & Soffa wedge bonder with Al wire. The advantage of using a wire bonder to connect the devices to the mount was that the bonds could easily be removed with tweezers and so the wafer did not have to be remounted between measurements. Double bonds were made for every electrical connection to reduce the likelihood of thermal contraction ‘ripping’ the bonds away during measurement.

Once two devices had been fully bonded, the mount was attached to the end of a bespoke cryostat ‘stick’ (see Fig.3.6(b)) which contained the corresponding low resistance wires for each of the electrical lines. The stick was designed to enable insertion into the large cryostats that were used to control the devices’ temperature.

The stick was, in turn, connected to a custom-built breakout box, which allowed for each of the lines to be separately connected to either a Keithley 2182 nanovoltmeter or a Keithley 6221 DC sourcemeter with BNC cables. Each of the lines could be separately grounded while changing connections, which helped mitigate the risk of static discharges overloading the nano devices. The equipment was controlled by a script written in LabView by Dr Burnell, which allowed for large, multi-variable measurement runs to be set-up.

It should be noted that it is more common, throughout many studies in this field, to use AC lock-in amplifiers when measuring lateral spin valves to extract various different frequency responses to the injection current. AC measurements allow very quick determination of the spin-related signals observed in such devices with relatively high signal-to-noise ratios.

The method utilised in this thesis, that of DC current reversal, is an equivalent method that makes use of DC measurements instead, which provides the same advantages of an AC lock-in measurement, while also providing a clearer indication of some

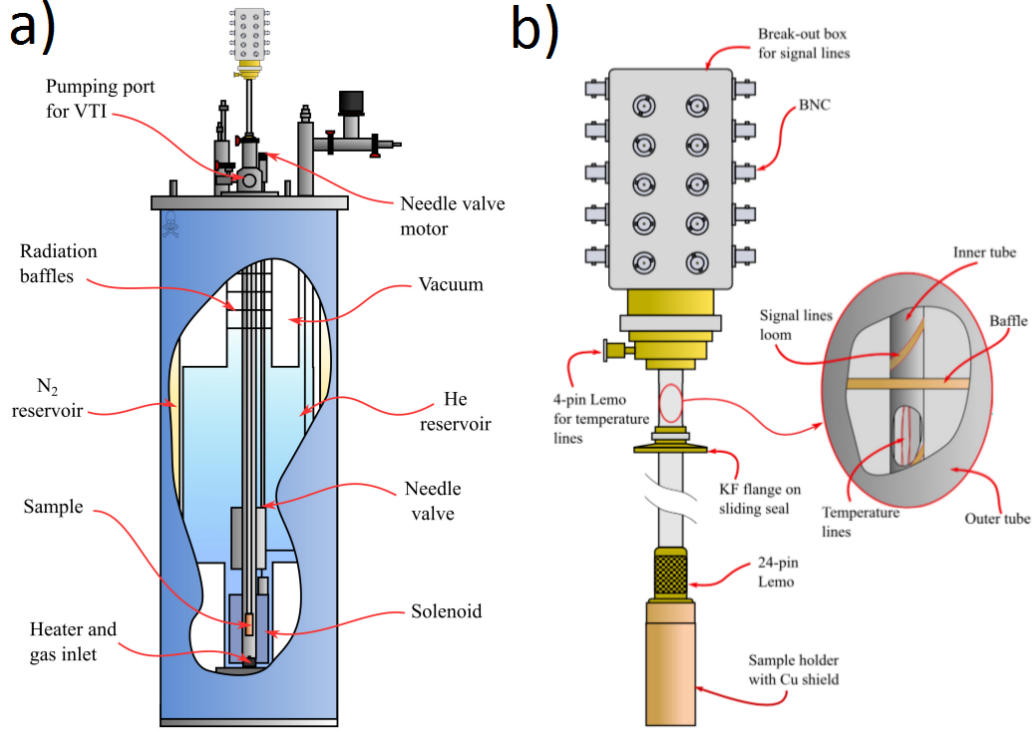


Figure 3.6: Figures taken from [5]. (a) shows a schematic of the cryostat used during the measurements in this study. (b) An illustration of the ‘measurement stick’ used to insert samples into the cryostat. The various BNC connections displayed at the top allow for the separation of electrical connections to the nanovoltmeter and DC sourcemeter.

of the thermal signals hidden during quicker methods [4, 53]. Because of this study’s interest in the thermal properties of lateral spin valves, the slower DC current reversal method was chosen.

Each device was then electrically tested by passing 100  $\mu\text{A}$  along the entire non-magnetic channel, while measuring the voltage drop between the injector and detector (see Fig.3.7). This arrangement is referred to as a ‘local’ measurement. A device was deemed to be worth measuring fully if its electrical resistance was of the order of a few  $\Omega$  (much higher resistances are indicative of incomplete electrical connections).

The stick and mount were then inserted into an Oxford Instruments cryostat (see Fig.3.6(a)) which enables fine control of temperature via the evaporation of liquid He,

using a roughing pump. The He was insulated from the surrounding environment with a jacket of liquid N<sub>2</sub> and could be slowly bled into the main chamber using a needle valve.

By carefully balancing the flow of He with the amount of heat supplied by an in-situ resistive heater, the temperature of the cryostat could be controlled from 300 K down to 2.17 K. At temperatures below 2.17 K, He<sup>4</sup> enters its superfluid state and the thermal properties of the cryostat used in this study become much harder to control. For example, the superfluid helium can begin to flow ‘up’ the sides of the cryostat vessel instead of evaporating at the point of injection. Because of the temperature stability required during this study’s measurements, the temperature of the cryostat was not taken below 3 K.

The cryostat also contained a superconducting magnet positioned beneath the bottom of the chamber, allowing for magnetic fields of up to 3 T to be applied to the samples. Additionally, the mount’s angular alignment was controlled by a stepped motor, which enabled the devices to be rotated within the magnetic field.

### 3.2.2 Local Measurements

Local measurements were performed on the devices to determine the  $\rho$  of the non-magnetic nanowire, while their temperature was lowered from 290 K down to 3 K. Eight voltage readings were made per R measurement by alternating a DC current between  $\pm 500 \mu\text{A}$  every 0.739 s. A prime number was used for the sample rate to prevent the pick-up of other phases of electrical noise (for example from the mains electricity in the lab). The current direction was reversed in order to prevent Peltier heating/cooling during the measurement (since the heat contributions from the two opposite flow directions cancel each other out). From the eight readings, an average R was calculated by dividing the measured voltages by the applied currents; this was performed every two seconds while the temperature was lowered at a rate of about 2 K per minute.

Each R measurement was then converted into  $\rho$  using Eq(2.48), with the injector-detector separation for L and with A being the channels thickness multiplied by its width.

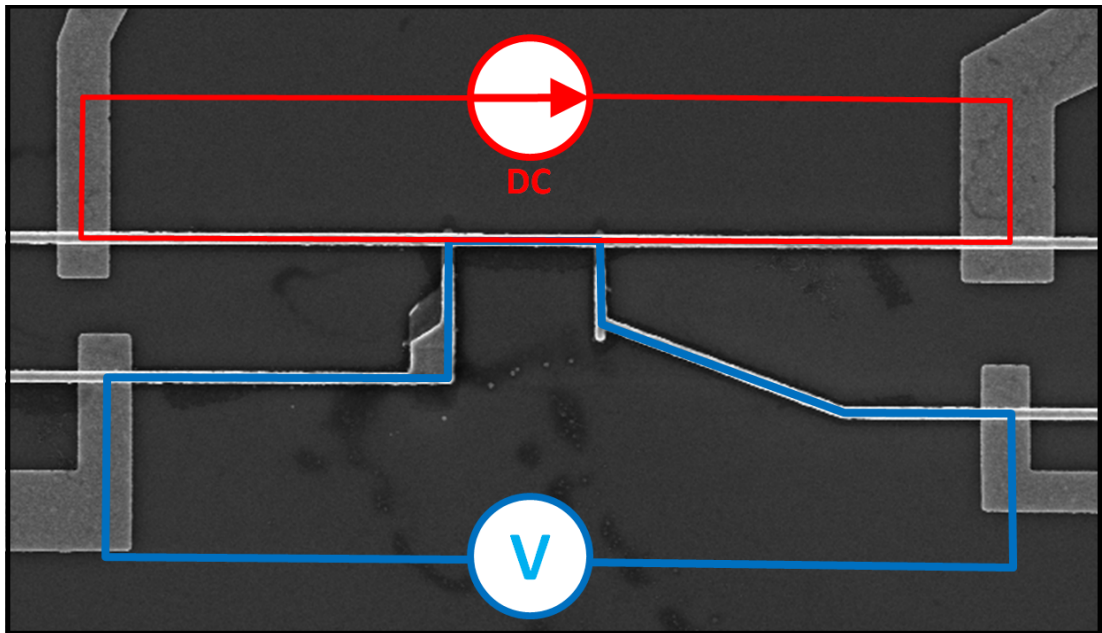


Figure 3.7: An SEM image of an LSV, overlaid with an electric circuit diagram for a local measurement. The DC current (red) is passed through the non-magnetic channel, while the change in voltage is measured between the two ferromagnets (blue).

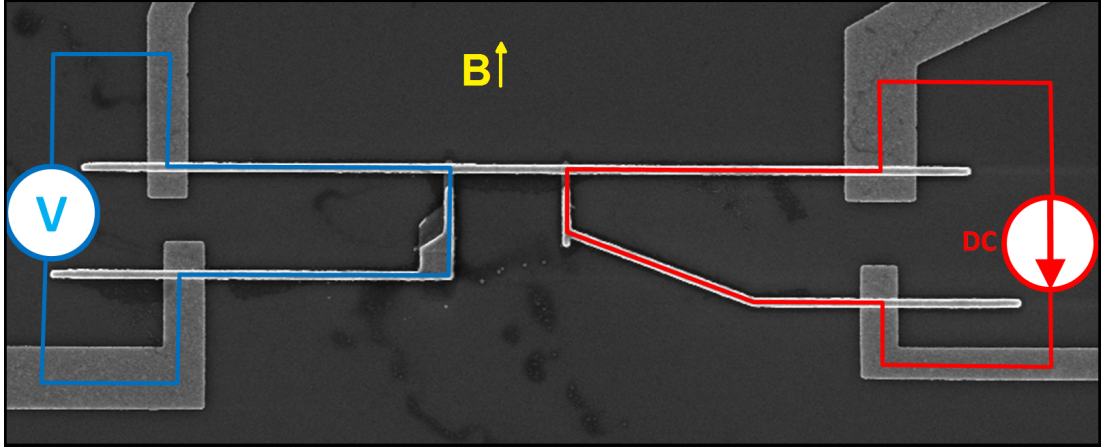


Figure 3.8: An SEM image of an LSV, overlaid with an electric circuit diagram for a non-local measurement. The DC current (red) is passed through the injector into the non-magnetic channel, while the change in voltage is measured across the detector’s interface (blue). The orientation of the applied magnetic field (parallel and in-plane to the long axis of the ferromagnetic electrodes) with respect to the devices is marked in yellow.

### 3.2.3 Non-Local Measurements

Once the local measurements for the device were completed, the BNC cables on the breakout box were switched to form the ‘non-local’ configuration (see Fig.3.8). Fifty-one current values between  $\pm 500 \mu\text{A}$  were applied, again at a rate of once every 0.739 s, so that the relationship between injection current and detector voltage (NLIV) could be examined. The temperature was held stable (within  $\pm 50 \text{ mK}$ ) throughout.

The devices were then rotated so that the applied magnetic field was parallel to the long axis of the ferromagnetic electrodes (see Fig.3.8), enabling them to be remagnetised in a direction perpendicular to the main channel. Constraining the ferromagnets to one axis of magnetisation is an important assumption with regards to the processes within LSVs [54]. Non-local measurements were continually made as the applied field strength was varied between  $\pm 100 \text{ mT}$ , which ensured that the ferromagnetic electrodes fully transitioned from a parallel to anti-parallel alignment and then back to parallel again. In total, around 100 NLIVs were measured at each temperature.

After a full set of non-local measurements was performed at 3 K, the temperature was raised to 4 K and then allowed to settle for two minutes before another set was

measured. Measurements were made at intervals of 1 K up to 50 K, after which the density of measurements was reduced up to 290 K.

### 3.3 Sample Characterisation

It is evident from Eq(2.42) and Eq(2.48) that the dimensions of the LSVs' features are significant when trying to compare their electronic and spintronic properties. It is important to obtain a high degree of accuracy when measuring the physical dimensions of certain parts of the devices.

For measuring the size of such small features, SEM imagery is a very powerful tool. Fig.(2.6) shows that an SEM is easily capable of resolving the different parts of an LSV. A Leo 1530 FEG-SEM was used to characterise the lateral dimensions to a resolution of roughly  $\pm 10$  nm.

The thickness of the non-magnetic channel is also an important dimension. An estimate of the thickness was provided during deposition by the crystal monitor, to a very high precision ( $\pm 0.1$  Å). However, comparisons with test thin-films yielded an accuracy of only around  $\pm 10$  nm with respect to the thickness confirmed using X-Ray reflectivity (XRR).

XRR was performed on a Bruker D8 diffractometer. However, it does not work with nanoscopic devices such as LSVs, since the x-rays have to reflect off a large surface area. Instead, thin films must be measured. In order to facilitate this, a substrate of clean, thermally oxidised Si was situated next to the LSV template during deposition. As a result, a thin film with the same thickness as the LSVs was produced in tandem, which could be measured using XRR. The resulting plots of x-ray count vs angle of reflection were fitted in the BEDE modelling software, in order to obtain the thicknesses of the two different metal layers.

---

# CHAPTER 4

---

Thermal Signals In Non-local IVs

Many investigations into LSVs utilise alternating current (AC) measurements, in order to very rapidly extract the spin signal of the devices [11, 19, 20]. But the result is that a number of other electrical and thermal effects within the device remain hidden. A more thorough technique can yield a better understanding of the physics at play.

By instead measuring DC sweeps [2, 53], the relationship between injection current and non-local voltage can be more closely observed [4–6]. Through careful analysis, a wide range of different signals can be extracted from the NLIVs, helping to build a much more complete picture of the devices themselves [48]. It is advantageous then, if not considerably more time consuming, to measure large numbers of DC NLIVs at many different temperatures and magnetic field strengths, in order to develop a greater understanding of spin transport in general.

A recent study by Stefanou et al. [1] presented a model for thermal diffusion in LSVs that separated out the various thermal signals present at the interface of the detector. However, because of a relatively small number of measurements at low temperatures, it is difficult to make any firm conclusions regarding the processes present in their devices. Additionally, they struggled to apply the model to some of their lower temperature data because of a constrained number of devices to compare. By building up a larger dataset and taking more measurements, the veracity of their model can be put to the test.

## 4.1 Non-Local IVs

For this study, two sets of LSVs was fabricated in which the ferromagnetic electrodes were both made from permalloy (Py: 80 % Ni, 20 % Fe). For one set, the non-magnetic channel was composed of six 9's Ag (99.9999 % purity), while the other was made with six 9's Cu. During fabrication, the deposition of the non-magnetic material was paused after 50 nm for 25 minutes before the remaining 50 nm was added. This was done to facilitate an additional experiment: attempting to create a control for the method often used to intentionally dope metallic nanowires – where impurities are deposited as a very thin, non continuous, ‘delta’ layer during the middle of the main evaporative stage [4].

Two NLIVs of one of the Ag devices can be seen in Fig.4.1(a). The relationship between the injection current and the non-local voltage is roughly quadratic in shape and can be approximated by [5]

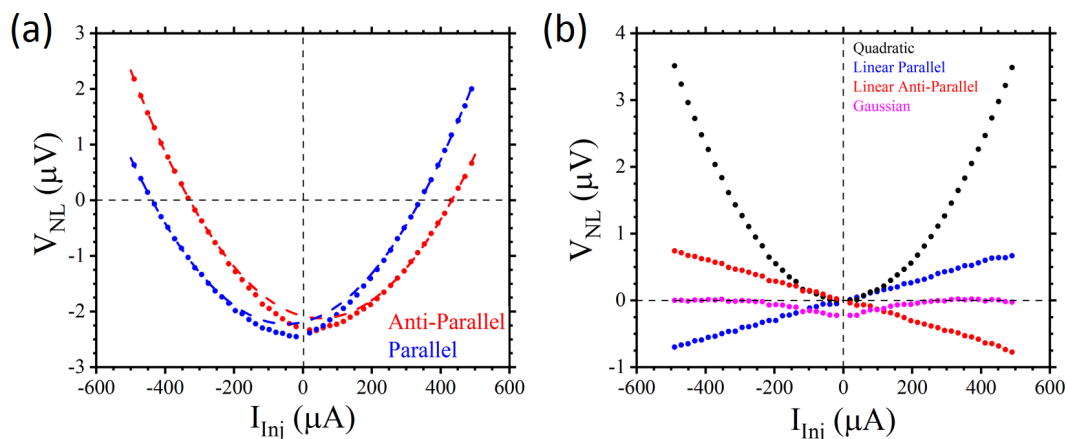


Figure 4.1: **(a)** shows the non-local voltages measured at specific injection currents for the Py/Ag device with an injector-detector separation of 650 nm, at 4 K. The blue dots are the voltages measured when the two Py electrodes were magnetically aligned parallel to each other, while the red dots were measured when they were aligned anti-parallel. The dashed lines are quadratic fits to Eq(4.1), but only the data for  $|I| > 250 \mu\text{A}$  were used when fitting because of a non-quadratic deviation close to  $0 \mu\text{A}$ . **(b)** shows the same two NLIVs, but decomposed into their constituent terms. The black data has had everything but the quadratic term subtracted, the blue and red data have had everything but the linear term removed (blue for the parallel IV, red for the anti-parallel) and the magenta data has had the entire quadratic fit removed, leaving only the small Gaussian shaped deviation. It should be noted that the deviation is not necessarily a truly Gaussian peak and has only been labelled as such because of its apparent appearance – it is analysed further in chapter 6.

$$V = AI^2 + BI + C \quad (4.1)$$

It can be seen in Fig.4.1(a), that when the two ferromagnets magnetically switch from parallel to anti-parallel with respect to each other, the non-local voltage flips across the y-axis. In Fig.4.1(b), where the different terms from Eq(4.1) have been separated out, it becomes more clear that it is the gradient of the linear term that switches. This is in agreement with Eq(2.40) and Fig.2.7, which showed that the potential difference between the detector and the non-magnetic channel, created by spin diffusion, is linear with respect to current and also that its sign is dependent on the relative magnetic

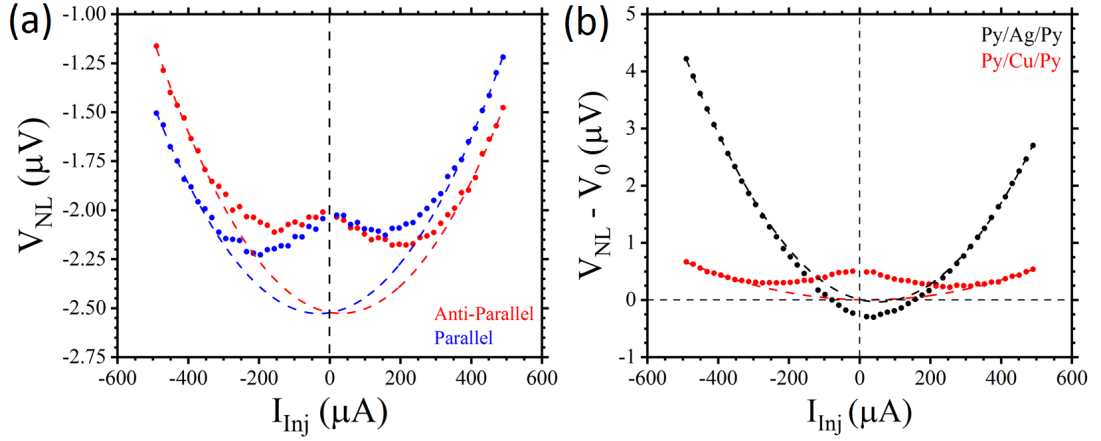


Figure 4.2: **(a)** Two non-local IVs for the Py/Cu LSV with a separation of 550 nm at 5 K, for its parallel (blue) and anti-parallel (red) alignments. The dashed lines are quadratic fits to the voltages for  $|V| > 350 \mu\text{A}$ . **(b)** A comparison of the anti-parallel NLIVs from the Ag device (black) in Fig.4.1(a) and the Cu device (red) in (a). The current independent term has been subtracted from both data sets to allow for a better comparison to be made between the two. The dashed lines are fits to Eq(4.1).

alignment of the detector and injector.

The dominant quadratic term seen in the NLIV has regularly been attributed to Joule heating within the injector, as discussed previously [1, 4–6]. The amount of heat dissipated into the device at the point of injection goes with  $I^2$  according to Eq(2.47), which in turn will diffuse down through the non-magnetic channel. The resulting temperature gradient, with respect to the cooler detector, generates a potential difference through the Seebeck effect, as outlined in Eq(2.61). The stronger the injection current, the more Joule heating, the larger the temperature gradient, the bigger the potential difference. As for the current-independent term -  $C$ , this is also most likely explained by thermoelectric potentials [5], but between the voltmeter and the device and hence are independent of the current applied to the LSV.

In Fig.4.2(a) two NLIVs from one of the Cu devices can be seen. The deviation from the quadratic fit is much more pronounced and in the opposite direction to that seen for the Ag devices. This observation is fairly novel and will be expanded upon greatly in chapter 6.

A comparison between the two materials is shown in Fig.4.2(b) where it is apparent

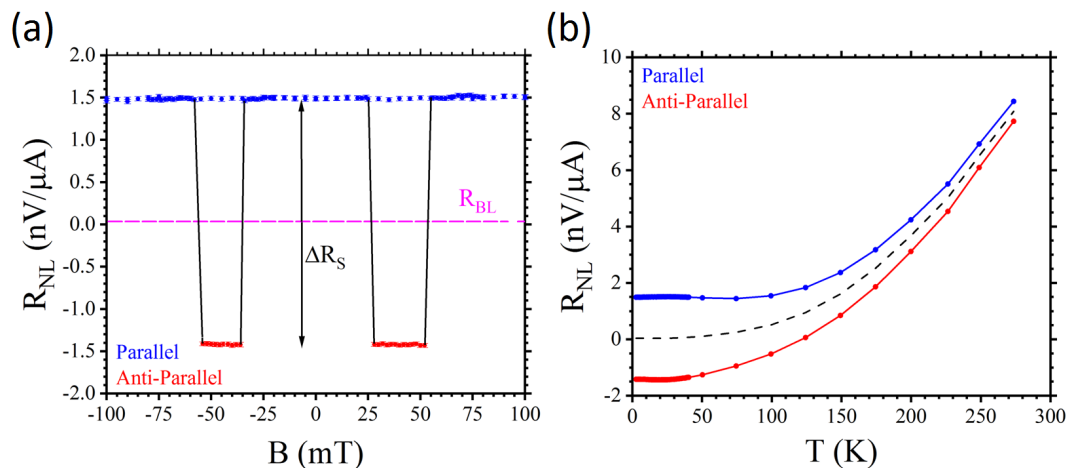


Figure 4.3: **(a)** shows the non-local resistance from the fits to Eq(4.1) across the full range of applied magnetic field strengths, for the Py/Ag device with a separation of 650 nm at 4 K. The two magnetic alignments have been colour-coded as before, with the blue data representing the parallel state and the red data, the anti-parallel. The difference between the two states has been marked with the spin signal ( $\Delta R_S$ ) while the average value of the two states is indicated by the dashed magenta line and labelled with the baseline resistance ( $R_{BL}$ ). The black vertical lines between the two states have been added to indicate more clearly where the spin-switchings occurred. **(b)** shows the average value of  $R_{NL}$  for the parallel (blue) and anti-parallel (red) spin states of the 650 nm Py/Ag device, for a range of temperatures up to 275 K. The lines connecting the data points are added as a guide for the eye. The dashed black line is the value of  $R_{BL}$  at each temperature.

that the both the quadratic and linear components of the NLIV are significantly smaller for the Cu than for the Ag. In order to better compare, the individual components should be examined separately.

## 4.2 Spin Signal

The linear term from Eq(4.1) is often described as a ‘non-local’ resistance ( $R_{NL}$ ) [4–6] because of the resemblance it bears to the IV relationship of Ohmic resistance. Its magnetic dependence is shown more fully for one of the Ag devices in Fig.4.3(a).

The graph shows that  $R_{NL}$  remains constant as the applied field is decreased from

100 mT until, at around -35 mT, it suddenly switches to negative – this occurs when the detector (which realigns at smaller field strengths because of its large nucleation pad) realigns with the field [11, 13]. Then, at roughly -55 mT,  $R_{NL}$  suddenly returns to its original value (when the injector also realigns). The applied field is taken down to -100 mT before being incrementally returned to its initial value of 100 mT. At approximately +30 mT and +55 mT respectively, both the detector and injector flip back to their original alignments.

The difference in  $R_{NL}$  between the parallel and anti-parallel states is  $\Delta R_S$  (as outlined in Eq(2.40)) because it describes the change in potential at the detector, normalised to the injection current [19, 55]. Contrary to initial expectation, the midpoint between the two states is not exactly zero, representing a ‘linear with respect to current’ voltage, that is independent of magnetic alignment – called the baseline resistance ( $R_{BL}$ ) [4, 47].

The temperature dependence of  $R_{NL}$  for both magnetic alignments can be seen in Fig.4.3(b), where it is evident that, despite the non-local resistance increasing with temperature, the difference between the two alignments diminishes as room temperature is approached.  $R_{BL}$  increases with temperature, slowly at first but then quite rapidly above 100 K.

The accepted cause of the non-zero  $R_{BL}$  in recent literature is the Peltier effect [1, 46]. The amount of heat generated or absorbed by the Peltier effect is strongly temperature dependent ( $\Pi = TS$ )[56] and approaches zero at low temperatures. This would explain the behaviour seen in Fig.4.3(b). Additionally, the amount of Peltier heating scales linearly with current (Eq(2.49)) in the same manner as the  $R_{BL}$ .

Peltier heating/cooling occurs when current passes through an interface between two materials and so the most likely site for the signal’s origin is the injection interface. Just as with the Joule heating, thermal gradients arising from the additional heating propagate down the central channel and generate a Seebeck voltage at the interface with the detector.

In Fig.4.4(a) the spin-switchings of the 650 nm device are shown for both 4 K and at room temperature. It can clearly be seen that the spin signal is smaller at higher temperatures, but also that the field strength required to realign the Py electrodes is reduced because, as the ferromagnets begin to approach their Curie temperature, their magnetisation begins to decrease (outlined in Eq(2.2)). Consequently, the magnetic

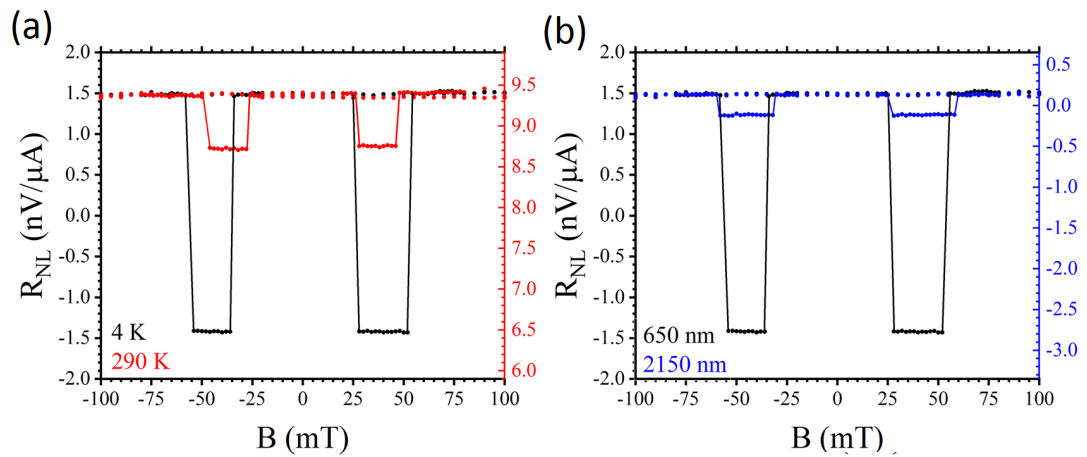


Figure 4.4: **(a)** compares the spin-switching for the 650 nm Py/Ag device at 4 K (black data) and at 290 K (red data). The red y-axis on the right has been shifted down for the data at 290 K to enable a better comparison between the two datasets. The black and red vertical lines have been added as a guide to indicate spin-switching. **(b)** compares the spin-switching for two different Ag devices at 4 K - one with a separation of 650 nm (black data) and the other with a separation of 2150 nm (blue data). Again, the y-axis for the second device has been shifted to more easily compare.

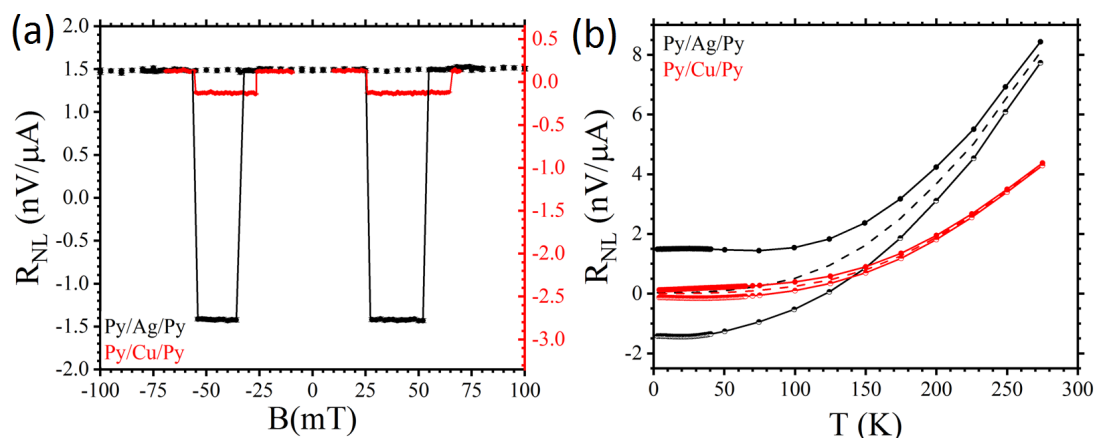


Figure 4.5: **(a)** compares the spin-switching for the 650 nm Py/Ag device at 4 K (black data) and the 550 nm Py/Cu device at 5 K (red data). The red y-axis on the right has been shifted down for the Cu's data to enable a better comparison between the two datasets. The black and red vertical lines have been added as a guide to indicate spin-switching. **(b)** compares the temperature dependence for the two ferromagnetic alignments for both the Ag (black) and Cu (red) devices with separations of 650 and 550 nm respectively. The black and red dashed lines show the value of  $R_{BL}$  for the two different devices at the full range of temperatures measured.

field required to realign the spins within them is also smaller.

Fig.4.4**(b)** shows the change in spin signal when compared to a device with a longer injector-detector separation. For an LSV where the spins had to diffuse roughly  $3\frac{1}{3}$  times further, the  $\Delta R_S$  is  $\sim 15$  times weaker. This demonstrates the significant diminishing of pure spin currents over distance which will be discussed and analysed further in chapter 5.

A comparison of the spin switching between the Ag and Cu can be seen in Fig.4.5**(a)** where it becomes even clearer that the device made from copper has a significantly smaller spin signal than that made from Ag. The fact that the ferromagnets switch at different field strengths for the measurement of the Cu device indicate that the sample may not have been perfectly aligned parallel to the magnetic field.

In Fig.4.5**(b)** the temperature dependence of  $R_{NL}$  for the two different materials is more closely compared. For both materials, the baseline resistance at low temperatures becomes zero, while the Ag exhibits a stronger signal at higher temperatures. The

copper's spin signal is also significantly smaller across the entire range of temperatures, almost disappearing all together towards room temperature.

### 4.3 Quadratic Term

As touched upon before, the quadratic nature of an LSV's NLIV can be explained by the thermoelectric voltage caused by Joule heating within the injector. Stefanou et al. showed using SThM imagery that the hottest spot in a Py/Ag LSV was the very thin, exposed part of the injector (See Fig.4.6(a)) [1]. In their study, they mounted a very temperature-sensitive sensor onto a force-sensitive cantilever which, when scanned across a device, provided a feedback of any temperature differences present on the sample's surface. This enabled them to build a temperature map of an LSV while spin injection took place.

The reason Joule heating dominates in the injector rather than in the non-magnetic material (which also carries part of the injection current) is demonstrated for Ag in Fig.4.7(a).

By combining Eq(2.47) and Eq(2.48), the amount of heat generation through Joule heating, per unit length, of a nanowire can be calculated from its resistivity and cross-sectional area (for an example current magnitude of 500  $\mu\text{A}$ ). It is clear that the amount of Joule heating in the injector completely dominates ( $\sim 40$  times larger) any heat production in the part of the Ag wire that carries away the injection current.

In Fig.4.7(b), a comparison between the average value of the quadratic parameter in a Py/Ag LSV and the resistivity of a Py nanowire is made. The temperature dependencies of the two are strongly correlated apart from a small deviation at low temperatures. The increase in A below 50 K cannot be explained by an increase in Joule heating and therefore must be related to the thermal transport properties of the device.

The quadratic parameters for each of the Ag devices at each temperature can be seen in Fig.4.8(a). Here, the values from each measurement taken during the magnetic field sweep have been averaged together at each temperature. As in Fig.4.7(b) the temperature dependence for each device's quadratic signal is very similar to that of the resistivity of a Py injector, down until 50 K at which point significant deviations occur. Interestingly, the devices with separations of 800 (red) and 900 (orange) nm respectively, both exhibit a significantly different temperature dependence to the rest

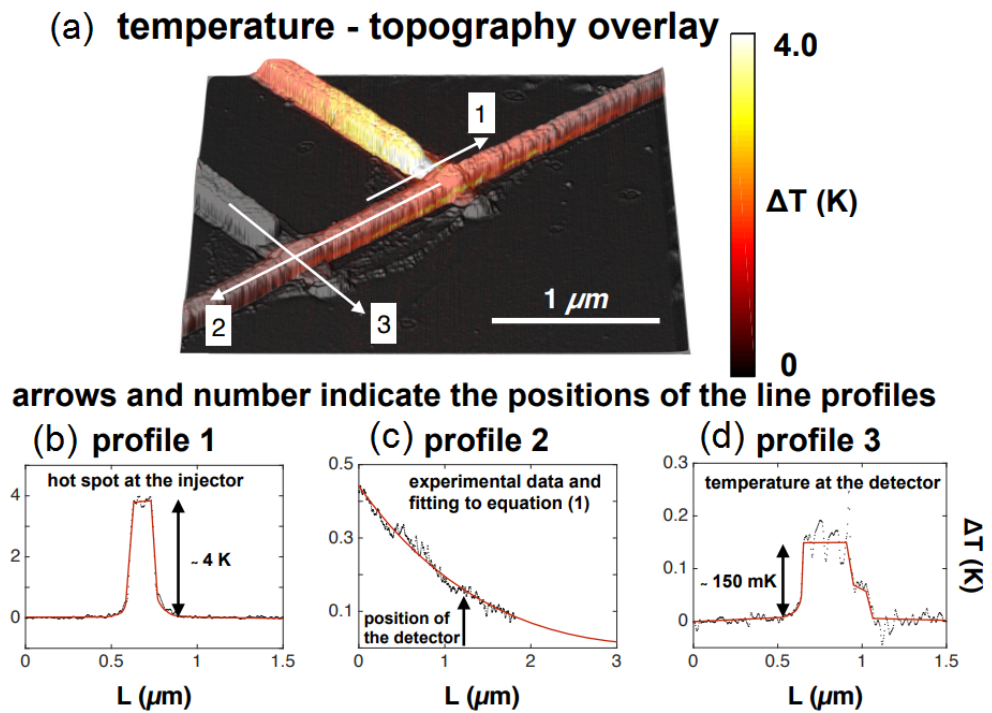


Figure 4.6: Figure taken from Stefanou's study [1]. (a) shows the temperature map of a Py/Ag LSV at room temperature whilst spin injection takes place. (b) is a two-dimensional splice of the temperature data running across the width of the Py injector. The red line is a fit to Eq(2.59). (c) instead shows the temperature gradient down the length of the Ag channel, moving away from the site of current injection. (d) shows the cross sectional data in the region where the Ag channel overlaps the Py detector.

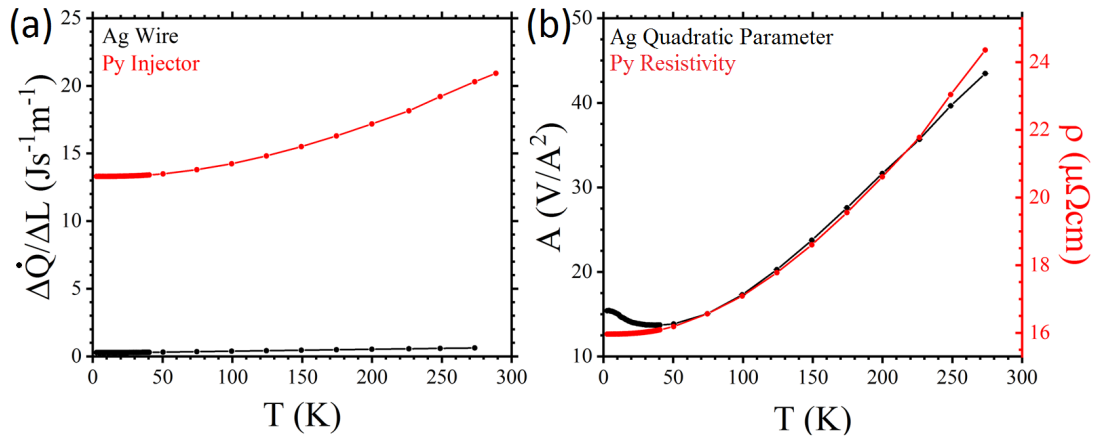


Figure 4.7: **(a)** The amount of heat generated by Joule heating, per unit length, for a current of  $500 \mu\text{A}$  in both a Ag nanowire (black) and a Py injector (red) - based on measurements of their electrical resistance. **(b)** shows the value of the quadratic parameter ( $A$ ) from fitting Eq(4.1) to the NLIVs of the 650 nm Ag device in black. The values of  $A$  from each of the measurements during the magnetic field sweep have been averaged together at each temperature. In red, is the resistivity of a Py nanowire with the same dimensions as the injector, taken from Dr Stefanou's PhD thesis [4]. The lines connecting the data points are merely a guide to the eye.

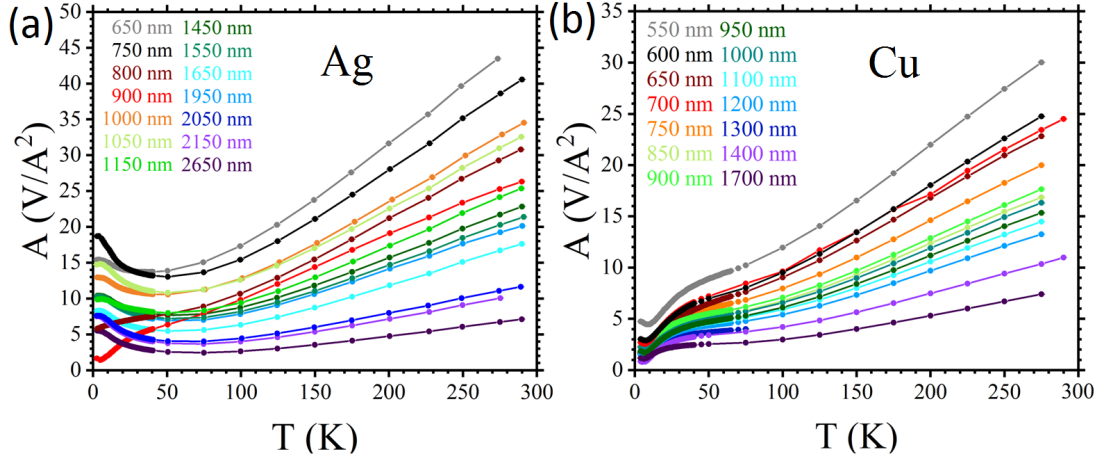


Figure 4.8: (a) The average value of the quadratic parameter at each temperature for each of the Py/Ag devices with their respective separations. The lines connecting the data points are guides for the eye. (b) The same graph but for the Py/Cu devices.

of the group indicating that their thermal properties must be unique.

In Fig.4.8(b) the values for the quadratic parameter for the Cu devices can be seen. The temperature dependence below 50 K is completely different to that seen in the Ag and behaves similarly to the two outliers. In order to better understand the underlying causes of the variation, the thermal properties of the two sets of devices need to be closely examined.

## 4.4 Baseline Resistance

As previously highlighted, the spin-independent component of the linear term of NLIVs is referred to as the baseline resistance.  $R_{BL}$  has been argued to arise from a thermoelectric signal generated by thermal gradients caused by Peltier heating at the point of current injection [4, 46] because the signal is linear with respect to the strength of the injection current, yet independent of the detector's magnetic alignment.

In Fig.4.9(a), the baseline resistance for each of the Ag devices is shown. Consistently,  $R_{BL}$  approaches zero at low temperatures which can be explained by the Peltier coefficient's strong temperature dependence. As  $T$  is increased, the Peltier coefficient becomes larger, resulting in stronger heating within the injector.

Fig.4.9(b) shows the baseline resistances of the Cu devices. The temperature de-

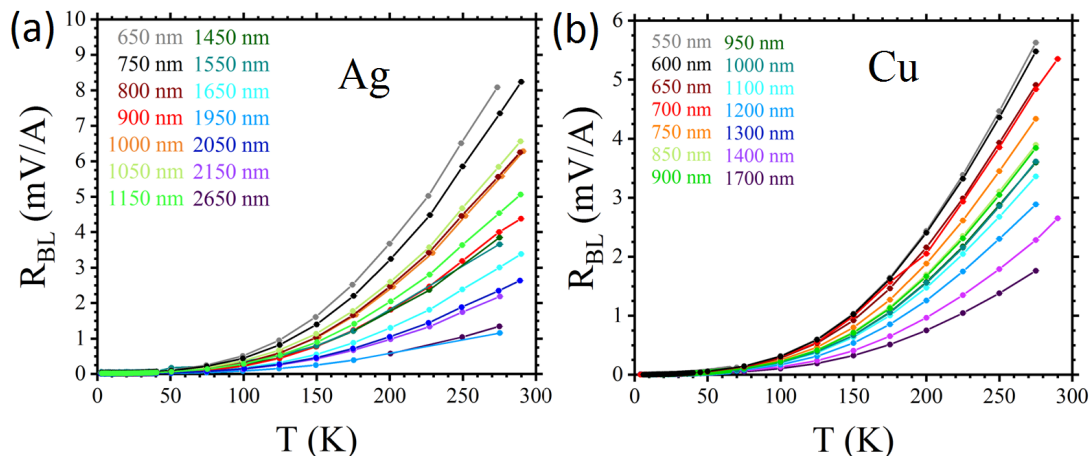


Figure 4.9: (a) shows the baseline resistance for each of the Py/Ag devices with their respective separations, at each temperature measured. The lines connecting the data are simply a guide for the eye. (b) The same graph but for the Py/Cu devices.

pendence looks identical to that seen in the Ag, albeit the magnitude of the signals are roughly half the size. Because the signals for both materials are effectively zero at low temperatures, it cannot be clearly seen whether the different temperature dependencies below 50 K are present.

The model presented by Stefanou et al. [1] outlined in chapter 2 can be utilised to better understand the temperature dependence of the amount of Joule and Peltier heating measured at each of the detectors. To do so, the quadratic parameters and baseline resistances need to first be converted into their respective thermoelectric voltages by multiplying them by the applied injection current.

## 4.5 Thermal Diffusion

In Fig. 4.10, both the quadratic parameters and baseline resistances have been converted into voltages for both the Py/Ag and Py/Cu devices. In the figure, the thermal voltages have been plotted against their injector-detector separations at a temperature of 5 K. In each case, the signals exhibit a strong exponential decay with distance (barring the outliers in red).

In chapter 2, a calculation was presented which allowed for the conversion of a temperature gradient across an LSV's detector into a thermoelectric voltage, using the

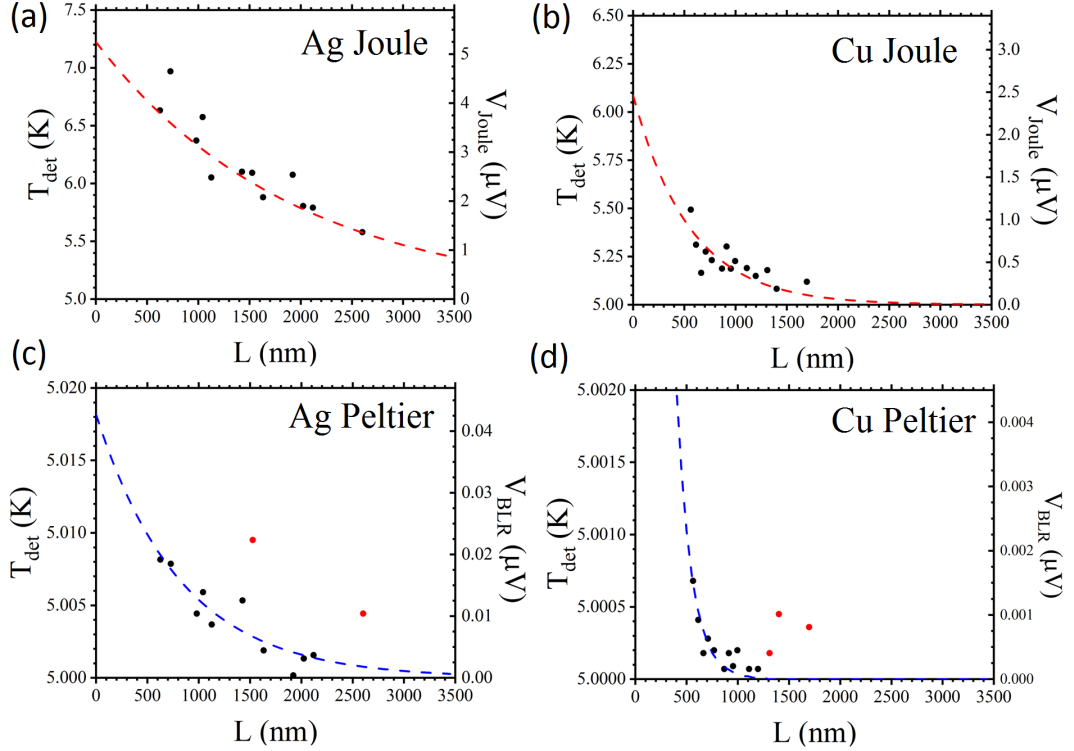


Figure 4.10: **(a)** The right-hand axis shows the total voltage measured across the detectors of the Py/Ag devices at 5 K, that can be attributed to Joule heating in the injector. The left axis shows those same voltages converted into the effective temperatures that would be required to produce them. The dashed red line is a fit to Eq(2.59). **(c)** is the same graph but for the voltages extracted from the baseline resistance instead. The data points in red have not been included in the exponential fit due to their significant deviation from the trend. Additionally, the 800 and 900 nm devices have not been included because of their unique temperature dependence with respect to the rest of the Ag devices. **(b)** and **(d)** are the same two graphs but for the Cu devices.

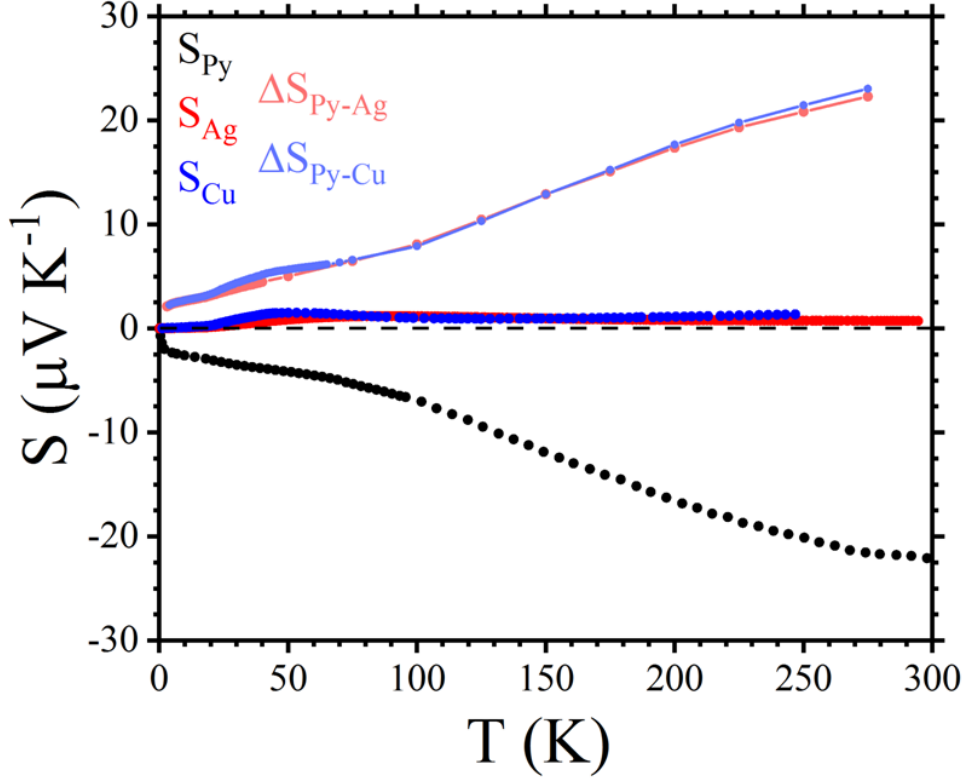


Figure 4.11: Seebeck coefficients for Ag (red), Cu (blue) and Py (black) nanowires for the full range of temperatures. The effective Seebeck combinations for both Py/Ag and Py/Cu interfaces are shown in light red and light blue respectively. The lines connecting the data points are guides to the eye.

difference between the Seebeck coefficients of both the non-magnetic and ferromagnetic materials (Eq(2.62)). The opposite calculation can be performed using the Seebeck coefficients shown in Fig.4.11 allowing the thermal voltages to be converted into effective temperature gradients across the detectors.

The Seebeck coefficients were taken from published values for Ag [57], Cu [58] and Py [59] nanowires. For temperatures beyond that which were available, the data has been linearly extrapolated. It is evident that the thermopower of the Py completely dominates that of the Ag and Cu and as a result, the magnitude of the generated thermal voltages is mostly governed by the ferromagnet.

The resulting temperatures are shown in Fig.4.10 on a separate axis to the voltages

– similar to that seen in Fig.4.6(c). Since the amount of heat reaching the detector appears to decay exponentially with distance, the data can be fitted with Eq(2.59) at each temperature, where  $x$  is the injector-detector separation and  $T_{\text{sub}}$  is the temperature at which the measurement was performed. The temperature of the injector and the thermal diffusion length of the central channel were left as fitting parameters.

The parameters resulting from fitting the thermal decay model can be seen in Fig.4.12. For the Ag, the thermal diffusion length extracted from both thermal signals agree remarkably well down to approximately 50 K, at which point the results from the two different fits diverge from each other. The data from the quadratic parameters doubles in decay length from 1000 nm up towards 2000 nm. Whereas the fits to the baseline resistance show that the diffusion length begins to increase (similarly to the Joule fits) before decreasing linearly down to 750 nm.

The fits to the Joule heating agree very well with those found by Stefanou et al. [1]. The diffusion length in their devices increased from 1000 nm up to 2500 nm below 50 K. Despite this, in their study they found they could not fit the baseline resistances at low temperatures because, they argued, that the signal ceased to be exponential in nature and exhibited a more linear relationship with distance. Their conclusion was that the phonon mean free path in the substrate became similar to the dimensions of the Ag wire at low temperatures, resulting in a transition to ballistic phonon transport as opposed to diffusive. The result of which was a rapid change to the thermal transport properties of the devices.

In the Py/Ag devices presented in this study however, the low temperature baseline resistances were able to be reasonably fit with the exponential model (after omitting outliers), arguably because of the greater number of individual devices measured. As a result the thermal diffusion length of the Peltier heating has been extracted at low temperatures which has not been fully achieved before.

In the Cu, the thermal diffusion lengths agree very well with those returned by fits to the Ag devices except for the fact that the Joule heating signal peaks at 25 K before decreasing back down to 1000 nm. Moran performed the same analysis for CoFe/Cu LSVs and although their results mostly agree with those obtained here, they did not observe the low temperature peak in the thermal diffusion length of their copper.

In Fig.4.12(c) it can be seen that the increase in the thermal diffusion length in the Ag from the Joule heating is reflected in an increase to the temperature of the

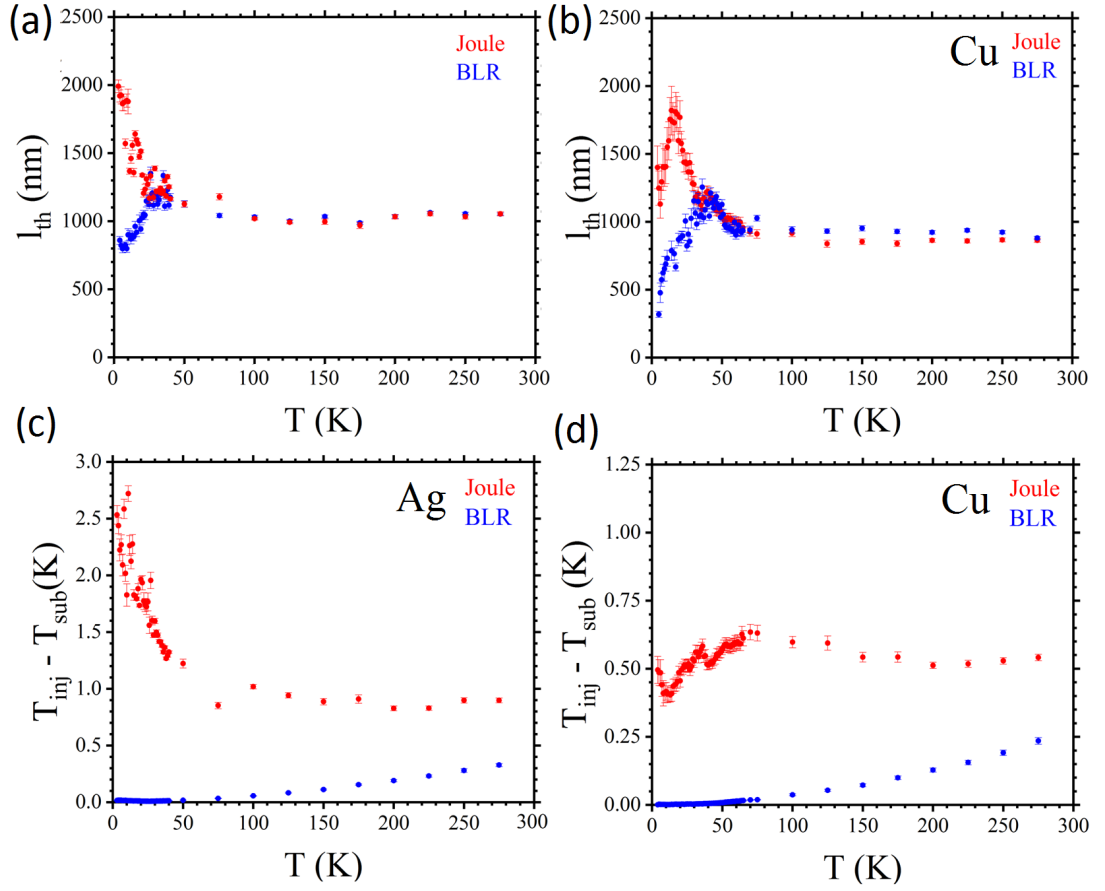


Figure 4.12: **(a)** The thermal diffusion length of the Ag channels from fits with Eq(2.59) to the signals produced by Joule (red) and Peltier (blue) heating at the detector. **(c)** shows the calculated temperature increase at the site of current injection, from the same fits. **(b)** and **(d)** show the same two graphs but for the Cu devices.

injector with respect to the substrate. The fact that the injector is warmer at lower temperatures, despite the fact that the resistance of the Py, and hence the amount of Joule heating, is much lower than at room temperature is not immediately apparent from the results to these fits.

In the baseline resistance signal the temperature increase at the injector is effectively zero at low temperatures due to the Peltier coefficient's strong temperature dependence.

For the Cu devices, the temperature increase due to Joule heating in the injector remains fairly constant across the entire temperature range. Again, as with the Ag devices, the warming of the injector due to the Peltier effect disappears below 50 K.

In order to understand the temperature dependence of the two thermal diffusion lengths, and that of the temperature increase in the injector within the Ag devices, further analysis is required.

## 4.6 Thermal Conductance

According to the model presented by Stefanou et al. [1] the thermal diffusion length can be decomposed in terms of the thermal conductivity of the non-magnetic channel and the thermal conductance of the nanowire's interface with the SiO<sub>2</sub> substrate using Eq(2.58).

The thermal conductivity of a metal can be calculated using the Wiedemann-Franz law [60] which converts the electrical conductivity using the Lorenz number ( $\Phi$ ).

$$\kappa = \frac{\Phi T}{\rho} \quad (4.2)$$

Other studies have utilised a temperature dependent version of the Lorenz number in order to properly account for a nanowire's structural effects on its thermal conductivity [57, 60–62].

$$\frac{\Phi(T)}{L_o} = \frac{\frac{\rho_o}{\rho_{ph}} + \left(\frac{T}{\Theta_D}\right)^5 J_5}{\frac{\rho_o}{\rho_{ph}} \left(\frac{T}{\Theta_D}\right)^5 J_5 \left[1 + \frac{3}{\pi^2} \left(\frac{k_F}{q_D}\right)^2 \left(\frac{\Theta_D}{T}\right)^2 - \frac{1}{2\pi^2} \frac{J_7}{J_5}\right]} \quad (4.3)$$

where  $L_o$  is the Sommerfield value of  $2.44 \times 10^{-8} \text{ V}^2 \text{ K}^{-2}$ ,  $k_F$  is the Fermi wave-vector,  $\Theta_D$  is the Debye temperature,  $q_D$  is the Debye wave-vector and  $J_n$  is given by

$$J_n = \int_0^{\frac{\Theta_D}{T}} dx \frac{x^n e^x}{(e^x - 1)^2} \quad (4.4)$$

The Fermi wave-vector is related to a metal's Fermi energy through an alteration to Eq(2.6)

$$k_F = \frac{\sqrt{2m^*E_F}}{\hbar} \quad (4.5)$$

where  $\hbar$  is the reduced Planck's constant. The Debye wave-vector can be calculated from the Debye temperature and a metal's speed of sound ( $V_s$ ).

$$q_D = \frac{\Theta_D K_B}{\hbar V_s} \quad (4.6)$$

$\Theta_D$  can be obtained by fitting the electrical resistivity of the central channel with the Bloch-Grüneisen formula (Eq(2.9)). The resistivity is found by measuring the electrical resistance between the injector and detector using a four-point 'local' measurement (shown in chapter 3). The resistance can be converted into the resistivity using Eq(2.48), the length of the channel, its width and its thickness (determined using SEM imagery and XRR analysis).

The resistivity of each of the devices used in this study can be seen in Fig.4.13. All the devices exhibit a characteristic resistivity vs temperature profile for non-magnetic metals and their resistivity at low temperatures is reasonable for noble metal nanowires [4, 6].

By averaging together all the individual curves for the two sets of devices, a representative resistivity of the non-magnetic material can be found (seen in Fig.4.13(c) and (d)). The average resistivities were both fitted with Eq(2.9) yielding a Debye temperature of  $191.8 \pm 0.5$  K for the Ag which is within the range of previously published values [63]. A value for  $\rho_o$  of  $1.6874 \pm 0.0005$   $\mu\Omega$  cm was also obtained which is a reasonable value for an Ag nanowire [4, 63].

For the Cu, the Bloch-Grüneisen fit returned a Debye temperature of  $274.4 \pm 0.3$  K and a  $\rho_o$  of  $0.9998 \pm 0.0002$   $\mu\Omega$  cm which are both very close to values previously reported for Cu channels in LSVs [6].

With a value of  $\rho_o$  in place,  $\rho_{ph}$  is trivially found by subtracting the base resistivity from the total. Using this, the value for the Debye temperature, the total resistivity, Eq(4.3), Eq(4.5), Eq(4.6) and published values for  $E_F$  and  $V_s$  the reduced Lorenz factor for the central channels can be calculated.

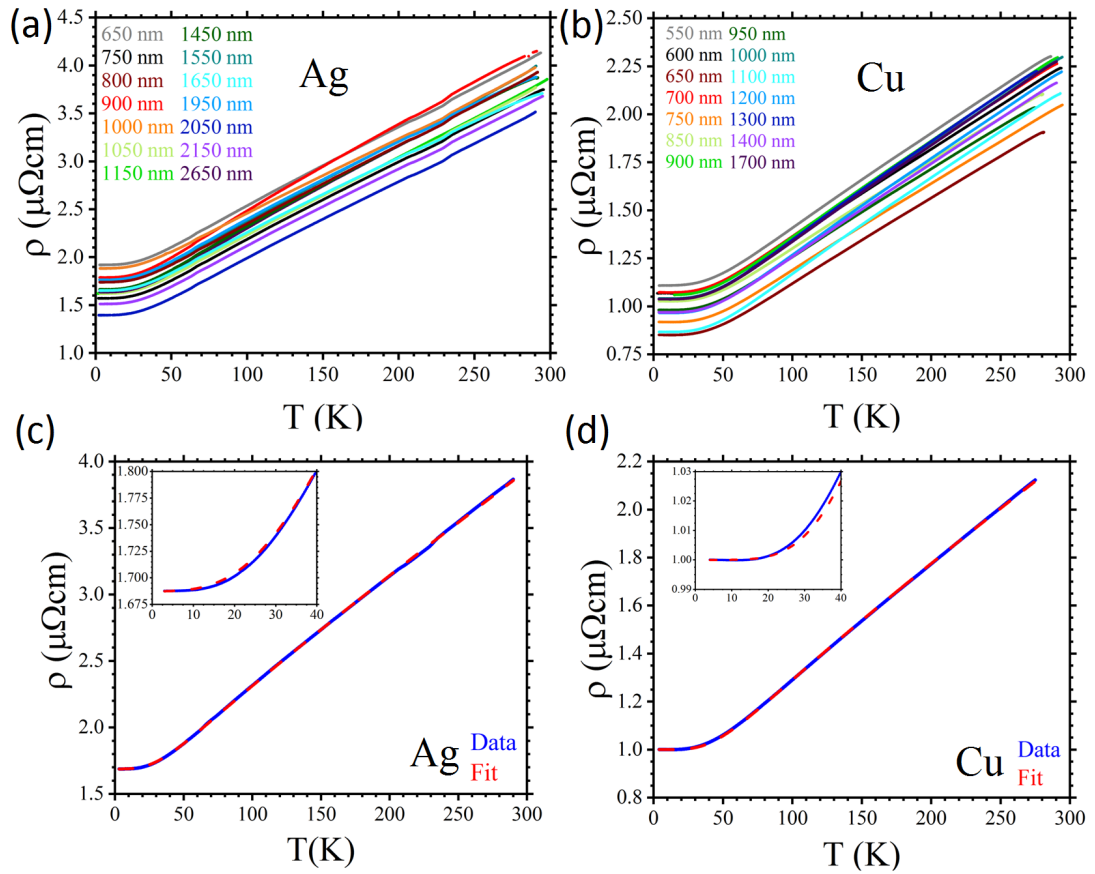


Figure 4.13: (a) The resistivity of each of the Ag channels calculated using Eq(2.48) and their respective dimensions. (c) shows the average resistivity of the Ag in blue. The dashed red line is a fit to Eq(2.9). (b) and (d) show the same two graphs but for the Cu devices.

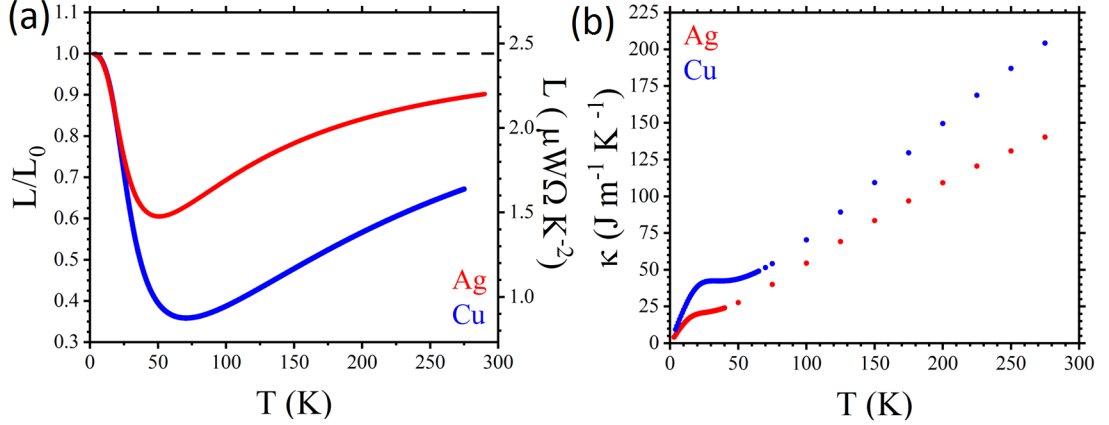


Figure 4.14: **(a)** The reduced Lorenz number for both the Ag (red) and Cu (blue) as calculated using Eq(4.3). On the right-hand axis is the factor multiplied by the Sommerfeld value. **(b)** The thermal conductivity of both the Ag (red) and the Cu (blue) calculated using Eq(4.2). The thermal conductivity data is discrete compared to the more continuous Lorenz number plot because it has only been calculated for temperatures where fits to the thermal data were made.

For the Ag and Cu, an  $E_F$  of 5.49 and 7.00 eV and a  $V_s$  of 2680 and 3810 m s<sup>-1</sup> were used respectively [64]. The resulting Lorenz numbers can be seen in Fig.4.14(a). At low temperatures, the Sommerfeld value is a fairly good approximation however as the temperature increases the Lorenz number rapidly diverges.

With the temperature dependent Lorenz number calculated for both materials, the thermal conductivity can be calculated from the resistivity using the Wiedemann-Franz law which is shown in Fig.4.14(b). For both materials the thermal conductivity decreases linearly from room temperature before plateauing out at around 50 K. Then as the temperature approaches zero, the thermal conductivity rapidly drops to zero. For the Cu, the temperature at which the thermal conductivity flattens out is noticeably higher leading to a larger temperature range of relatively unvarying thermal conductivity.

Using Eq(2.58) and the thermal conductivities of the Ag and Cu, the thermal diffusion lengths from the fits to Eq(2.59) can be converted into the thermal conductances of the substrate-channel interface.

In Fig.4.15 it can be seen for both materials, that the substrate-channel conduct-

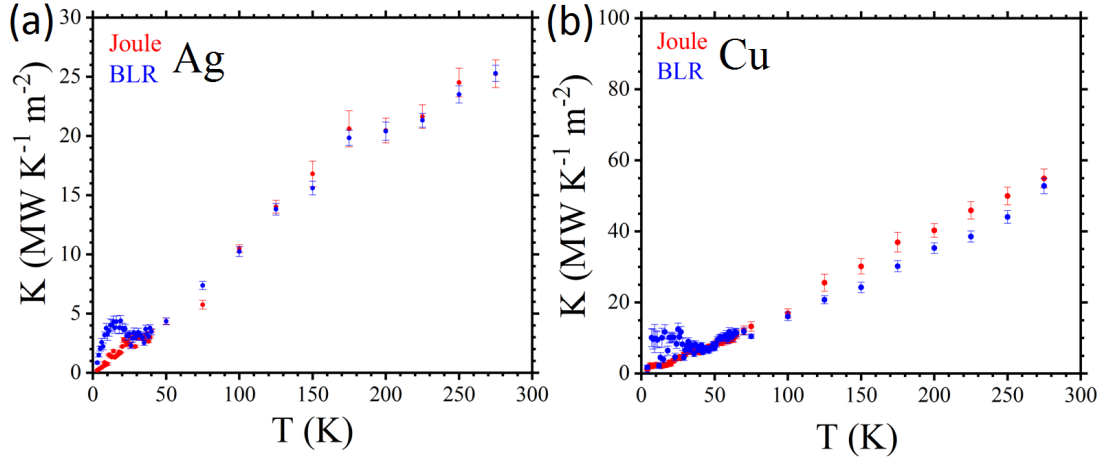


Figure 4.15: **(a)** The thermal conductance of the Ag/SiO<sub>2</sub> interface underneath the central channel as calculated from fits to the Joule heating signal (red) and the baseline resistance (blue). **(b)** The same graph for the Cu devices.

ance decreases linearly with temperature down from room temperature. The Cu-SiO<sub>2</sub> interface is slightly more thermally conductive – most likely due to the Cu’s higher thermal conductivity than the Ag.

Significantly, the results from the fittings to the baseline resistance yield a small peak in the substrate conductance between 10 and 30 K, for both materials. This peak is not reflected in the conductances calculated from the Joule heating signals. In the study by Stefanou et al. [1], it is argued that the unique behaviour of the Peltier signal at low temperatures is due to the phonon mean free path in the SiO<sub>2</sub> matching the dimensions of the non-magnetic channel – resulting in ballistic phonon transport.

By comparing the temperature dependencies of the two different conductances, an attempt can now be made to explain the variation in the quadratic parameter between the two materials. In the Ag, the the thermal diffusion length of the central channel continues to increase as the temperature is dropped below 50 K because the conductance with the substrate approaches zero faster than the thermal conductivity of the Ag itself. As such, more heat reaches the detector resulting in a large quadratic signal. For temperatures below 5 K, the thermal conductivity of the Ag sharply drops which is reflected by a small drop in the magnitude of the quadratic parameter in most of the devices (Fig.4.8(a)).

The temperature of the injector relative to the substrate also increases at low tem-

peratures in the Ag devices since the thermal conductivity of the Ag and the thermal conductance to the substrate both decrease, reducing the overall efficiency with which heat is transported away from the site of current injection.

For the baseline resistance, the reason the thermal diffusion length shortens at low temperatures is because of a small peak in the conductance with the interface, argued to be caused by ballistic phonon transport in the SiO<sub>2</sub> [1].

In the Cu, because the thermal conductivity drops more sharply below 20 K than in the Ag (Fig.4.14(b)), the thermal diffusion length of the central channel stops increasing, and begins to fall at low temperatures. Matched with the higher conductance between the Cu and the substrate, the result is that less of the Joule heating in the injector is able to reach the detector at low temperatures and so the quadratic parameter is lower than expected, as seen in Fig.4.8(b).

As such, the injector does not warm up as much in the Cu devices (Fig.4.12(d)) because comparatively more heat is transferred to the substrate than in the Ag devices. In the signals extracted from the baseline resistance, the same phenomena occurs as in the Ag. A small peak in the thermal conductance with the substrate at low temperatures leads to a rapid drop in the thermal diffusion length. Because of the Peltier coefficient's strong temperature dependence however, the effect is not obvious in the tiny signals observed at low temperatures.

As for the two outliers from the Ag devices (800 and 900 nm separations), the fact that the temperature dependence of their quadratic parameter is similar in shape to that of the Cu devices, indicates that their thermal conductance with the substrate must, for some reason, be more efficient than that seen in the rest of the samples. Further inspection of SEM imagery of the two LSVs did not yield any additional evidence so it is difficult to make a definite conclusion regarding their behaviour.

## 4.7 Conclusions

Two sets of LSVs with Py electrodes were produced, one composed of Ag and the other of Cu. In order to better understand the physics within the devices, large numbers of NLIVs were measured, at very finely controlled temperatures and for a wide range of injector-detector separations.

The NLIVs were decomposed into a quadratic Joule heating parameter, a magnetically dependent non-local resistance, a magnetically independent baseline resistance

and also a small Gaussian deviation from the quadratic.

By converting the voltages produced by both Joule and Peltier heating into effective temperature gradients using previously published values for the Seebeck coefficients of all three materials, the length dependence of the detector's temperature was established for both sets of devices.

A model introduced by Stefanou et al. was applied to the exponential behaviour of the thermal signals which yielded the thermal diffusion length of both the Ag and Cu, for both Joule and Peltier heating. Because of the large amount of data collected, low temperature fits to the baseline resistance were achieved that yielded new information about the temperature dependence of the Peltier-produced heat in LSVs.

The thermal diffusion lengths extracted from the fits agree well with those previously published [1, 6] and also match for both Joule and Peltier heating across both materials (except for below 50 K).

The thermal conductivity of both the Cu and the Ag were calculated using the Wiedemann-Franz law and temperature dependent Lorenz numbers, calculated from parameters obtained by fitting the electrical resistivity of both materials with the Bloch-Grüneisen formula. The Cu was found to have a slightly larger thermal conductivity than the Ag.

The diffusion lengths were then dissected in terms of the thermal conductivities of the non-magnetic materials and their thermal conductances with the substrate. Both materials exhibited an extremely similar temperature dependence to the efficiency of heat flow into the substrate, with the Cu yielding slightly larger conductances.

A small, low temperature peak in the thermal conductance with the interface was observed for both materials in the results to fitting the baseline resistance. This peak has been previously argued to be caused by ballistic phonon transport in SiO<sub>2</sub>. A possible explanation for the effect only arising in the baseline resistance is that the much smaller amounts of heat produced by the Peltier effect at low temperatures, possess much longer phonon wavelengths than those produced by Joule heating.

The temperature dependence of the quadratic parameter in both Ag and Cu nanowires has been explained in terms of the relative conductivities of the central channel and the substrate interface. In the Ag, the rapidly falling conductance of the interface leads to more efficient heat flow to the detector at low temperatures and hence a larger quadratic signal. In the Cu however, its sharply decreasing thermal conductivity leads to a

reduction in the flow of heat to the detector resulting in a reduced quadratic signal.

Overall, the veracity of the model presented by Stefanou et al. has been reinforced. Both sets of devices have yielded excellent agreement with the model. The large amount of data at low temperatures has shown that exponential decay-with-distance of thermal signals can be demonstrated and that reliable fits can be achieved to as low as 3 K.

Careful calculation of the relative thermal conductivities can explain the difference in temperature dependence between the two materials; however, the anomaly that the heat produced by the Peltier effect, conducts differently than that produced by Joule heating at low temperatures, is very interesting and deserves further study.

---

# CHAPTER 5

---

Spin-Flip Scattering in ‘Dirty’ Noble Metals

In the previous chapter, the spin signals in Py/Ag and Py/Cu nanowires were measured by looking at the magnetic field dependence of the NLIVs. In many measurements of noble metal devices, it has been observed that the spin diffusion length, which is a measure of the efficiency with which non-equilibrium spin currents can travel through a medium, follows the same temperature dependence of the electrical mean free path [2–4, 44, 53, 55, 65]. The Elliot-Yafet (EY) theory of spin-flip scattering, which describes a temperature independent spin-flip probability for each electron scattering event [23, 38, 39], predicts such observations.

However, on closer inspection, it was often also observed in these studies that at the lowest temperatures, a ‘downturn’ appeared in the measurements of  $l_{sf}$  that was not reflected in the mean free path, thus suggesting a breakdown in the EY model.

Two main camps have emerged in response, in an attempt to explain the low-temperature anomalies observed in  $l_{sf}$ . One argues that scattering with the surfaces of the non-magnetic channels introduces an additional source of spin-flip scattering [44, 55, 66]. The other posits that magnetic impurities diffuse from the ferromagnets into the central channel, resulting in Kondo scattering at low temperatures [2, 3, 20, 67].

## 5.1 A Literature Review

In 2008, Kimura et al. [55] performed a study to determine whether the unexpected downturn was caused by the emergence of more dominant surface scattering at low temperatures caused by an increase in the mean free path ( $\lambda$ ). They varied the thickness of the central channel in Py/Cu LSVs and observed that, as they decreased the thickness, the temperature at which the peak in  $l_{sf}$  occurred increased. This, they claimed, provided key evidence that the downturn was due to surface scattering of the pure spin currents, which became more noticeable at low temperatures.

Expanding on this, Zou and Yi [66] looked into the effects of gradually oxidising the surface of the Cu channel in their Py/Cu LSVs. They found that over time, as the surface became more oxidised, the downturn diminished. They argued that the oxidation of the structure’s surface reduced the amount of spin flip scattering by isolating the pure spin currents from magnetic impurities ‘trapped’ at the surface.

Another experiment by Idzuchi et al. in the same year [44] added MgO caps to their Cu channels and found that a previously measured downturn disappeared. They concluded that the amount of surface scattering was suppressed by the MgO because

of a change to the amount of SOC.

In 2013, Villamor et al. performed another study on Py/Cu LSVs [2], in which they found no discernible correlation between the thickness of their Cu and the behaviour of the downturn – in direct contrast to Kimura’s study. They did, however, determine that the dominant process for spin-flip scattering in their devices was through EY-led grain-boundary scattering. This however, failed to explain the downturn at low temperatures which, they hypothesised, potentially originated from magnetic impurities diffusing from the ferromagnets into the Cu during deposition.

One of the reasons why scattering with magnetic impurities was a popular suggestion, is that the Kondo effect results in a very distinctive curve in  $\rho$  at low temperatures; the shape of which was very similar to that seen in  $l_{sf}$ .

A paper by O’Brien et al. put this to the test in 2014 [20]. They grew sets of both Cu and Al LSVs with various different ferromagnetic electrodes. According to their findings, the temperatures at which the downturns occurred were very close to the Kondo temperatures of the respective ferromagnetic impurities in Cu. For Al on the other hand, which is argued to not exhibit Kondo scattering[68], no downturn was observed in the spin signals. This, according to their study, was clear evidence that the downturn could be explained by Kondo scattering from diffusive magnetic impurities.

In 2015 Batley et al. performed an additional study [3], testing the difference between devices made with four 9s or six 9s Cu. They found that, while a clear downturn was measured for the LSVs made from less pure Cu, it was significantly diminished in the six 9s devices. It was also observed that, in the four 9s Cu, a Kondo upturn was present in the measurements of  $\rho$  – seen to a lesser extent in the more pure Cu. Batley et al. concluded, therefore, that the larger amounts of magnetic impurities in the less pure Cu led to a much more significant downturn, reinforcing O’Brien’s findings.

This was supported by O’Brien et al. in 2016 [67] when they purposefully annealed Fe/Cu LSVs in an attempt to increase the diffusion of magnetic material from the Fe into the Cu. They observed that, as they increased the temperature of annealing, the downturn in their samples became more prominent – coinciding with an increase in the Kondo signature in their measurements of  $\rho$ . Thus, they again concluded that the downturn could be entirely explained by the diffusion of magnetic impurities.

The problem plaguing the magnetic impurity argument is that a corresponding

Kondo upturn has not universally been observed in devices exhibiting the  $l_{sf}$  downturn. This was addressed in a theoretical study by Kim et al. in 2017[69], in which they presented a model for the Kondo suppression of spins in LSVs. They argued that, because of the magnetic nature of Kondo scattering, the effect upon spin transport measurements was much more significant than on purely electrical observations (at least  $1000 \times$  more sensitive); which would explain the prevalence of the downturn.

A barrier to resolving the apparent discrepancy has been the tendency for studies to discuss the behaviour of the downturn in terms of the spin signal, rather than the spin diffusion length. The problem with this inconsistency is that  $\Delta R_S$  is a less intrinsic property than  $l_{sf}$  and has many more contributing factors such as: the polarisation of the injection current, the efficiency of the injection interfaces etc. This makes it much harder to isolate the root cause of the downturn. The  $l_{sf}$ , on the other hand, is a purer reflection of the spin transport properties of the non-magnetic material and should be the focus when analysing the origins of spin-flip scattering.

More recently, a study by Stefanou [4] tried to pick apart the magnetic impurity argument by looking instead at Py/Ag LSVs. In a 2015 paper by Isasa et al. [70], the crystal structure of Ag nanowires was shown to play a huge part in the spin transport properties of their LSVs. They observed that epitaxially-grown Ag exhibited far less spin-flip scattering than polycrystalline Ag. Stefanou subsequently grew two sets of Py/Ag LSVs using the same six 9s source material: one with an Ag deposition rate of  $0.2 \text{ \AA s}^{-1}$  and the other with a rate of  $0.4 \text{ \AA s}^{-1}$ . Stefanou measured the size of the Ag grains using X-ray diffraction to show that, when grown more quickly, the grains were 50 % larger.

When Stefanou measured the spin transport properties of the two sets of devices, it was observed that the Ag with fewer grain boundaries exhibited no discernible downturn, while the slowly-grown Ag had one that was very distinct. In electrical measurements, the slowly-grown Ag was found to be more resistive and yet, neither set of devices yielded a Kondo upturn. This suggested that the downturn could be ascribed to large amounts of spin-flip scattering at grain boundaries (previously highlighted in Villamor's 2013 study), since the source material and dimensions of the Ag were the same.

One potential counter argument, is that the slower deposition of Ag in Stefanou's study allowed for a greater diffusion of magnetic impurities from the Py into the main

channel – thus introducing more Kondo scattering. This could be tested however, by initially growing Py/Ag LSVs at  $0.4 \text{ \AA s}^{-1}$  (recreating the conditions from Stefanou’s devices), but then disrupting the Ag’s crystal structure higher up the nanowire’s cross-section (for example, by doping with non-magnetic impurities). If a downturn was observed in such a device it would lend much more weight to the conclusion that crystal structure, and not magnetic impurities, plays the dominant role in the introduction of a downturn.

## 5.2 Non-Magnetic Impurities In Py/Ag LSVs

As described in chapter 4, a set of Py/Ag LSVs were purposefully doped with non-magnetic impurities (inherent to the deposition chamber) during their fabrication. This was achieved by growing six 9s Ag quickly ( $0.4 \text{ \AA s}^{-1}$ ), a method shown by Stefanou to produce a good crystal structure [4], but by pausing the growth midway for 25 minutes – before finishing the deposition.

A second reason for this methodology was to act as a control for a technique of doping, in which a small layer of impurities (called a delta layer) is purposefully deposited into a host material, midway through its growth [4]. Twenty-five minutes was chosen as the length of delay through personal experience of attempting to purposefully dope Ag nanowires with delta layers of Pt through e-gun deposition.

Under UHV conditions, gas molecules present within deposition chambers will bind to cold, clean surfaces through van der Waal’s interactions [71], forming a monolayer of condensed particles. The rate at which this occurs is driven by the partial pressures of the molecules in question as well as their temperature (a higher kinetic energy results in a larger chance of binding). Such adsorption of gaseous material during deposition acts to disrupt the crystal structure of the grown material and hence increases the amount of scattering that occurs in devices produced under UHV conditions.

While the growth was paused, the pressure in the deposition chamber according to an ion-gauge filament located in situ was, on average,  $8 \times 10^{-9}$  mbar. At such pressures, a monolayer of gaseous material is predicted to form within a few minutes [71]. The main contributors to the pressure are listed in Table 5.1, which shows that the most dominant contaminant will have been  $\text{N}_2$ .

To ensure that the attempted method of disrupting the Ag’s crystal structure did not increase the diffusion of magnetic impurities into the central channel, the resistivity

## 5.2 Non-Magnetic Impurities In Py/Ag LSVs

---

| Constituent Gases       |          |                         |
|-------------------------|----------|-------------------------|
| Molecular Weight (amu ) | Molecule | Partial Pressure (mbar) |
| 2                       | $H_2$    | $2 \times 10^{-9}$      |
| 18                      | $H_2O$   | $2 \times 10^{-9}$      |
| 28                      | $N_2$    | $6 \times 10^{-9}$      |
| 44                      | $CO_2$   | $5 \times 10^{-10}$     |

Table 5.1: A table of the partial pressure measurements taken during the deposition of the Ag from the mass spectrometer. The molecules responsible for the peaks at each molecular weight have been assumed, based on the most common naturally occurring gases . The pressures represent an average over the entire deposition.

of the Ag can be closely inspected. In Fig.5.1 it can be seen in the inset that even below 4 K, the resistivity of the Ag shows no evidence of increasing as it is cooled – to a precision of 0.002 %. It has to be concluded, therefore, that within the accuracy of the measurements made, the Ag within these devices contained an insignificant amount of impurities with Kondo moments.

In order to obtain the spin diffusion length of the Ag, the spin signals from each of the devices grown have to be compared. The complete set of spin signal measurements for the Ag devices can be seen in Fig.5.2(a), where each value of  $\Delta R_S$  has been calculated by finding the difference between the average values of  $R_{NL}$  for the two distinct spin states. It can be seen that generally speaking, as T increases the spin signal decreases. This can be explained by an increase in the amount of spin-flip scattering in the Ag caused by an increased number of phonons at higher temperatures. The downturn discussed in the literature review can be clearly seen below 30 K.

As with the thermal signals in chapter 4, the trend shows that for devices with longer separations, a smaller spin signal is observed. This is more clearly shown in Fig.5.2(b), where at each temperature, the spin signal exhibits an exponential decay with distance.

This phenomenon can be explained by the Valet-Fert model [21, 35] for spin diffusion, as derived in section 2.3.5. The data in Fig.5.2(b) were fitted with Eq(2.41) to find the spin diffusion length.

Eq(2.42) was used to calculate  $R^{F1}$ ,  $R^{F2}$  and  $R^N$  for Eq(2.41).  $w^{F1}$ ,  $w^{F2}$  and  $w^N$

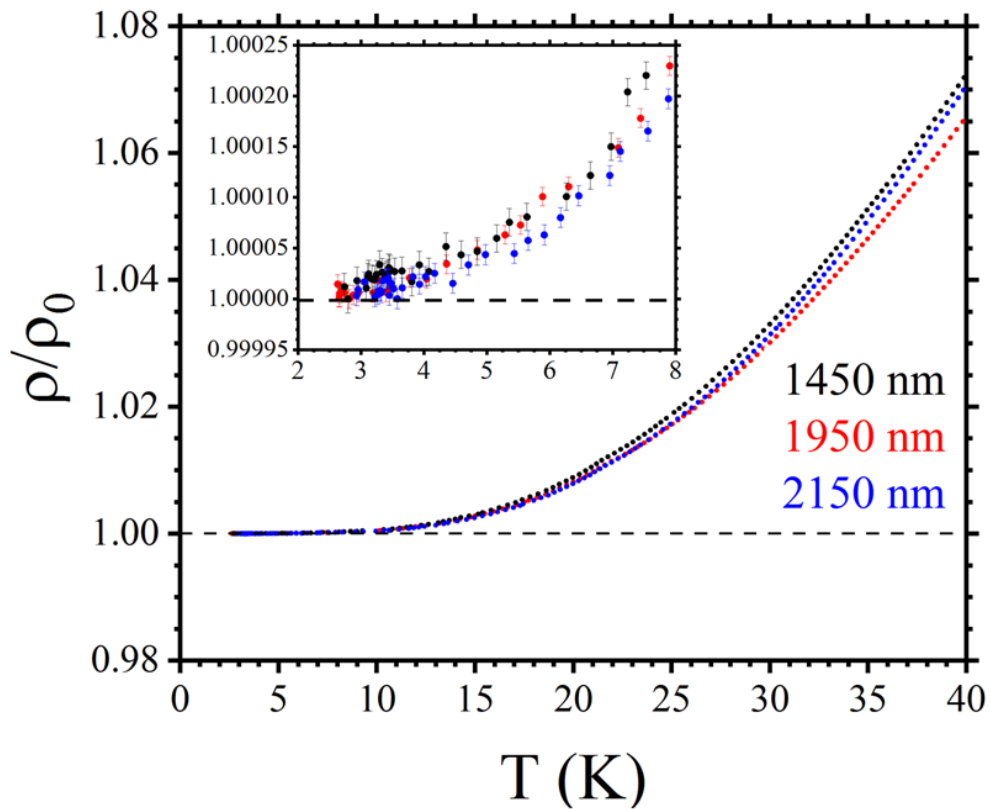


Figure 5.1: The values of  $\rho$  for three of the Py/Ag devices, normalised to their minimum resistivity ( $\rho_0$ ), which was found by fitting the data with Eq(2.9). The inset shows a much closer inspection of the low temperature data.

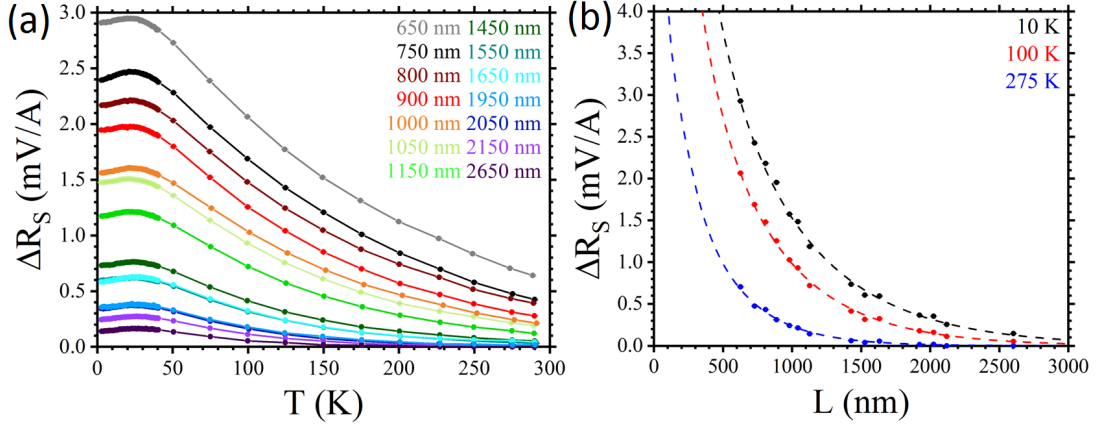


Figure 5.2: (a) The difference in  $R_{NL}$  for the parallel and anti-parallel states ( $\Delta R_S$ ), for each of the devices with different separations, at each temperature measured. The lines connecting the data points are guides for the eye. (b) shows the spin signal of the devices plotted against their separations at three different temperatures. The dashed lines are fits to Eq(2.41) at each of the corresponding temperatures.

were determined by averaging the values from each of the LSVs, obtained through SEM imagery:  $w^{F1} = 190 \pm 10$  nm,  $w^{F2} = 120 \pm 10$  nm and  $w^N = 160 \pm 7$  nm.  $t^N$  was calculated from an XRR measurement of a thin film grown at the same time as the devices – with a value of  $100 \pm 10$  nm.

It should be noted that the averaging of the physical dimensions of multiple LSVs, in order to attempt to fit their respective spin signals, is one of the key challenges in characterising spintronic devices. Since each device’s unique physical attributes will affect the spin signal yielded at its detector, by averaging out the different widths and thicknesses, a large amount of uncertainty is introduced to the model.

In Py,  $\rho$  and  $l_{sf}$  have been shown to be strongly related [72] and the product of the two is regularly assumed to be a constant [5] equal to  $6.73 \times 10^{-16} \Omega \text{ m}^2$  which was used at all temperatures in the calculation of  $R^{F1}$  and  $R^{F2}$ .

For the fits to the Valet-Fert model of spin diffusion, all that remain from Eq(2.41) as fitting parameters are the spin diffusion length of the non-magnetic channel and the spin polarisation of the injector. The resultant values for  $l_{sf}^N$  can be seen in Fig.5.3.(a).

As expected, the spin diffusion length decreases at higher temperatures due to increased spin-flip scattering from phonons in the Ag. However, just as with the spin

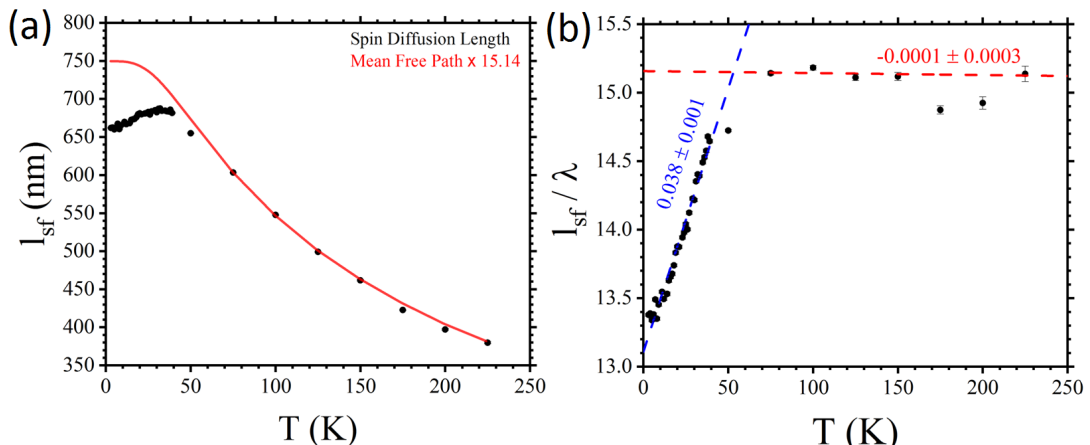


Figure 5.3: **(a)** The spin diffusion length of the Ag (black), calculated from fits to Fig.5.2**(b)** using Eq(2.41). In red is the electrical mean free path of the Ag, calculated using Eq(5.1) and the resistivity shown in Fig.4.13**(c)**, multiplied by 15.14 to allow for a better comparison of the temperature dependence. **(b)** The spin diffusion length from **(a)** divided by the mean free path. The dashed blue line is a linear fit to the data below 50 K, while the red dashed line is a linear fit to the data above 50 K. The gradients of the two lines have been marked.

signals and in other studies, it decreases below  $\sim 45$  K despite the apparent lack of Kondo scattering in the resistivity.

According to the theory attributing the downturn in the spin diffusion length to magnetic impurities, the signal should at least be somewhat reflected in the  $\lambda$  of the non-magnetic channel. For the Ag, this can be calculated from the average resistivities in Fig.4.13**(c)** and using

$$\lambda = \tau V_F = \frac{m^* V_F}{ne^2 \rho} \quad (5.1)$$

by combining Eq(2.7) and Eq(2.5). The parameters used during calculations in this study are listed in Table 5.2.

According to the EY model of spin-flip scattering, the ratio of the spin diffusion length to the mean free path should be constant with temperature[2] (defined by a constant spin-flip probability) and yet, when this ratio is calculated for the Ag devices (see Fig.5.3**(b)**), the prediction clearly does not hold at all temperatures.

For temperatures above 50 K, it can be seen that the gradient of the ratio between

## 5.2 Non-Magnetic Impurities In Py/Ag LSVs

---

|                        | Ag                    | Cu                    |
|------------------------|-----------------------|-----------------------|
| $m^*/m_e$              | 0.99                  | 1.01                  |
| $n$ ( $m^{-3}$ )       | $5.80 \times 10^{28}$ | $8.49 \times 10^{28}$ |
| $V_F$ ( $km\ s^{-1}$ ) | 1390                  | 1570                  |

Table 5.2: A table of calculated parameters for Ag and Cu [7], which are required for some of the calculations made in this study.  $m_e$  ( $9.1094 \times 10^{-31}$  kg) is the mass of a free electron.

the two is, within the uncertainty, zero – indicating an independence from temperature. However, below 50 K there is a significant linear temperature dependence to the ratio of the two parameters, which represents a deviation from the EY model. The  $\chi^2$  residuals of the linear fit to the low temperature data (blue dashed line) yielded an adjusted  $R^2$  value (which is an indication of goodness of fit) of 97.3% supporting the conclusion that the deviation from EY scattering is linear with temperature.

The value of the ratio at higher temperatures gives a scaling factor which can be applied to the mean free path to predict what the spin diffusion length ‘should’ have looked like, had purely EY scattering been maintained. This can be seen in Fig.5.3(a) where the mean free path has been multiplied by 15.14 (taken from Fig.5.3(b)). At temperatures above 50 K there is an extremely strong correlation between the temperature dependence of the two length scales. However, below 50 K the spin diffusion length starts to shorten while the mean free path plateaus.

There is a much more significant downturn than that observed by Stefanou [4] in their Ag LSVs grown with the same source material and at the same deposition rate. This is a strong indication that, purely by disrupting the crystal structure of the Ag midway up the diffusion channel, a breakdown in EY scattering has been introduced at low temperatures – there is no evidence here that the downturn could have been caused by magnetic impurities.

In order to more thoroughly discredit the magnetic impurity argument, the temperature dependence of the ‘unexplained’ scattering can be calculated [2]. The spin diffusion length and mean free path can be used to calculate the spin-flip scattering rate ( $\tau_{sf}^{-1}$ ) using Eq(2.29), Eq(2.21), Eq(2.3), Eq(2.6) and Eq(5.1)

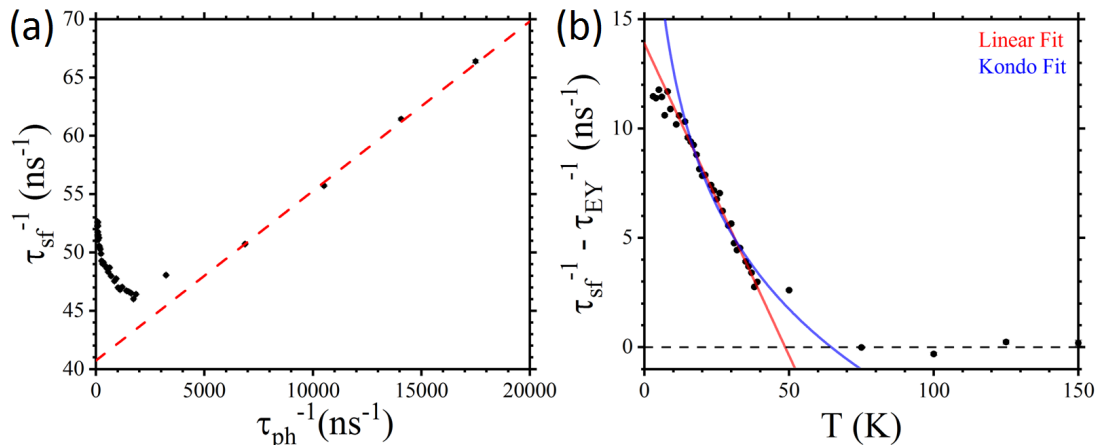


Figure 5.4: **(a)** The spin-flip scattering rate at each temperature calculated using Eq(5.2) versus the electron-phonon scattering rate calculated using Eq(5.3). The dashed red line is a linear fit to the data above  $5000 \text{ ns}^{-1}$ . **(b)** shows the difference between the spin-flip scattering rate from **(a)** minus the EY-predicted spin-flip scattering rate from Eq(5.4) – as a function of temperature. The red line is a linear fit to the data below 50 K, while the blue line is the same data fitted with  $\ln(T_K/T)$  from Eq(2.10).

$$\tau_{sf}^{-1} = \frac{D}{l_{sf}^2} = \frac{1}{e^2 g(E_F) \rho l_{sf}^2} = \frac{2E_F}{3ne^2 \rho l_{sf}^2} = \frac{m^* V_F^2}{3ne^2 \rho l_{sf}^2} = \frac{\lambda V_F}{3l_{sf}^2} \quad (5.2)$$

which is a measure of the number of spin-flip scattering events per second. The EY model tells us that  $\tau_{sf}^{-1}$  should be linear with respect to  $\tau_{ph}^{-1}$  [2], which is the number of electron-phonon and electron-electron scattering events per second (Eq(2.44)).  $\tau_{ph}^{-1}$  can be calculated using Eq(2.5) and Matthiessen's Rule

$$\tau_{ph}^{-1} = \frac{ne^2 \rho_{ph}}{m^*} = \frac{ne^2 (\rho - \rho_o)}{m^*} \quad (5.3)$$

For each of the temperatures at which spin signal measurements were made, both  $\tau_{sf}^{-1}$  and  $\tau_{ph}^{-1}$  can be calculated, as is shown in Fig.5.4(a).

The downturn from the  $l_{sf}$  can now be seen as an upturn in the spin-flip scattering rate as the amount of electron-phonon and electron-electron diminishes. By fitting the linear regime with a straight line, we can extract the spin-flip probabilities from Eq(2.44)[2]. The line of best fit, shown in Fig.5.4(a), is described by

## 5.2 Non-Magnetic Impurities In Py/Ag LSVs

---

$$\tau_{sf}^{-1} = (0.00147 \pm 0.00003) \tau_{ph}^{-1} + (4.05 \pm 0.03) \times 10^{10} s^{-1} \quad (5.4)$$

which gives  $a_{ph}$  as  $0.147 \pm 0.003$  % and the spin-flip probability from temperature independent scattering ( $a_0$ ) as  $0.145 \pm 0.003$  %. Here,  $a_0$  has been calculated by multiplying the y-intercept of the line of best fit with  $\tau_0$ , which was calculated to be  $3.58 \pm 0.06 \times 10^{-14}$  s, using Eq(2.5) and  $\rho_0$ .

In the study by Idzuchi et al. [44] spin-flip probabilities of 0.261 % and 0.403 % for phonons and defects respectively, were measured for Py/Ag LSVs capped with MgO. The values they obtained are significantly larger than those calculated here; however, the dimensions of their Ag channels were different (50 nm  $\times$  150 nm) and the Ag was also annealed post-fabrication, which would lead to a significantly different crystal structure.

It is also important to note that the spin-flip probabilities obtained for silver in this study are, within the uncertainty, identical for phonons and defects. There is no evidence that this should be the case and therefore further experimentation is required to verify that it was not coincidental.

There is another, simpler method for calculating the spin-flip probabilities, which can be found by rearranging Eq(5.2) and substituting in Eq(2.43) and Eq(2.7) to get

$$l_{sf} = \sqrt{\frac{\tau_{sf} \lambda V_F}{3}} = \sqrt{\frac{\tau \lambda V_F}{3a}} = \sqrt{\frac{\lambda^2}{3a}} = \frac{\lambda}{\sqrt{3a}} \quad (5.5)$$

which, when applied to the ratio between  $l_{sf}$  and  $\lambda$  from Fig.5.3(a) of 15.14, gives a spin-flip probability of  $0.145 \pm 0.001$  %, in agreement with the previous method.

The temperature dependence of the scattering, not explained by the EY mechanism, can be found by subtracting Eq(5.4) from the spin-flip scattering rate in Fig.5.4(a) – shown in Fig.5.4(b). For temperatures above 50 K there is effectively no non-EY scattering, but at lower temperatures there is a clear and steady increase.

Fits for two different relationships have been applied to the low temperature data. If the deviation from the mean free path was caused by magnetic impurities, then the temperature dependence would be expected to be logarithmic [69] (as seen with Kondo scattering). The Kondo fit in Fig.5.4(b) returned a Kondo temperature of  $64 \pm 2$  K which is significantly different to the value of 5 K mentioned for Fe impurities in Ag nanowires in [20]. Interestingly, a straight line fits the data below 50 K remarkably well (similar to that seen in Fig.5.3(b)). The adjusted  $R^2$  value for the Kondo fit was

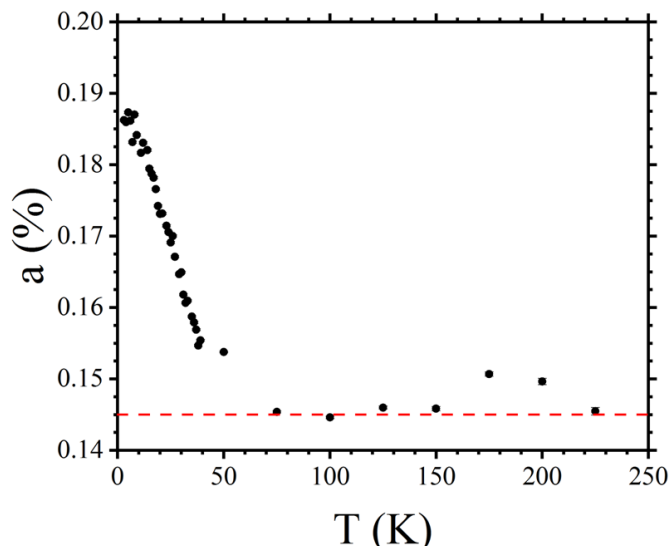


Figure 5.5: The approximate spin-flip probability as a percentage chance, for scattering events in the Ag devices at each temperature as calculated using Eq(5.5). The dashed red line is to mark the previously calculated value ( $a = 0.145\%$ ).

96.6% while for the linear fit a value of 98.8% was obtained, demonstrating that the linear fit in fact predicted the distribution of the data more reliably.

This observation lends even more weight to the argument that the deviation is not caused by the Kondo effect. A different possible explanation is that there is no ‘additional’ source of scattering, but that the spin-flip probability has transitioned from being temperature independent to temperature dependent below 50 K.

To test this, Fig.5.3(b) can be converted into a spin-flip probability using Eq(5.5), which can be seen in Fig.5.5. It is immediately apparent that the temperature dependence of the spin-flip probability is identical in shape to that of the ‘unexplained’ scattering rate in Fig.5.4(b). Consequently, an argument could be made that deviations from EY spin-flip scattering could be described just as well, by a temperature dependent spin-flip probability.

### 5.3 Non-Magnetic Impurities In Py/Cu LSVs

The same analysis can be performed for the spin signals of the Py/Cu LSVs produced for this study. The same six 9s Cu source material was used as by Batley for their

### 5.3 Non-Magnetic Impurities In Py/Cu LSVs

| Constituent Gases       |          |                         |
|-------------------------|----------|-------------------------|
| Molecular Weight (amu ) | Molecule | Partial Pressure (mbar) |
| 2                       | $H_2$    | $2 \times 10^{-8}$      |
| 18                      | $H_2O$   | $9 \times 10^{-9}$      |
| 28                      | $N_2$    | $5 \times 10^{-8}$      |
| 44                      | $CO_2$   | $8 \times 10^{-10}$     |

Table 5.3: A table of the partial pressure measurements taken during the deposition of the Cu, from the mass spectrometer. The values of the pressures have been averaged over the entire deposition.

Py/Cu LSVs [3, 5], in order to enable a comparison to their findings. Most of the studies arguing for the role of magnetic impurities in the downturn focus on devices made with Cu, while the more recent studies that cast doubt on such a conclusion use Ag. It would be useful, therefore, to make a more direct comparison between the two.

One difference to note between the two growths was that, while a very fast deposition rate was maintained for the Ag ( $0.4 \text{ \AA s}^{-1}$ ), a slower rate was used for the Cu ( $0.12 \text{ \AA s}^{-1}$ ). The reason the Cu was grown more slowly was that it was found through x-ray analysis that Cu grown at  $0.4 \text{ \AA s}^{-1}$  from the thermal-effusion cell had a very irregular crystal structure and electrical measurements indicated a much larger base resistance than that expected for Cu nanowires. After repeated growths, it was determined that the slower rate resulted in a much better crystal structure and lower base resistance.

Apart from the growth rate, every other aspect of the device fabrication was kept the same as for the Ag. Again, the growth of the central channel was paused midway for 25 minutes to allow ambient impurities to accumulate within the structure. The pressure was, on average,  $7 \times 10^{-8}$  mbar during the growth and pause – higher than for the Ag devices because of Cu’s higher melting point, which led to more out-gassing from the effusion cell during deposition.

As such, it is fair to assume that the disruption to the crystal structure of the Cu would have been greater than that imposed on the Ag devices. It can be seen in Table 5.3 that, just as for the Ag, the most dominant impurity will have been  $N_2$ .

A closer look at the low-temperature resistivities in Fig.5.6 shows that, for temperatures below 13 K, there is a small but measurable Kondo upturn in some of the

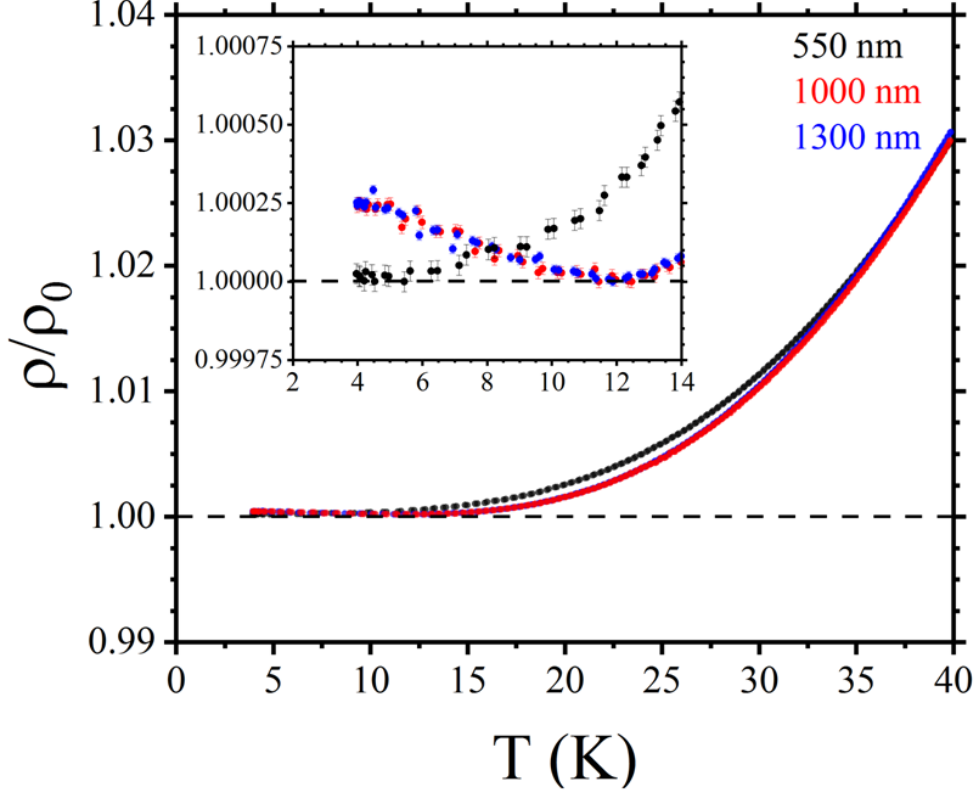


Figure 5.6: The values of  $\rho$  for three of the Py/Cu devices, normalised to their minimum resistivity ( $\rho_0$ ), which was found by fitting the data with Eq(2.9). The inset shows a much closer inspection of the low temperature data.

Cu devices (1000 and 1300 nm shown). This is a strong indicator of the presence of magnetic impurities within the non-magnetic channel.

Significantly, there is no discernible Kondo upturn in the 550 nm device, which suggests that the magnetic impurities present in the other devices must have diffused into the Cu from the Py electrodes, as opposed to being present in the source material. This is in agreement with other studies which observed diffusion of Py into Cu during deposition [2, 20, 67]. Closer inspection of the resistivities shown in Batley’s study [3] hints at a very small Kondo upturn in their six 9s Cu. However, because of the small size of the figures, it is hard to make a direct comparison with the upturns seen in this study. In total, over the 14 Py/Cu devices measured, 13 contained a similarly sized Kondo upturn (with only the 550 nm device being ‘Kondo free’).

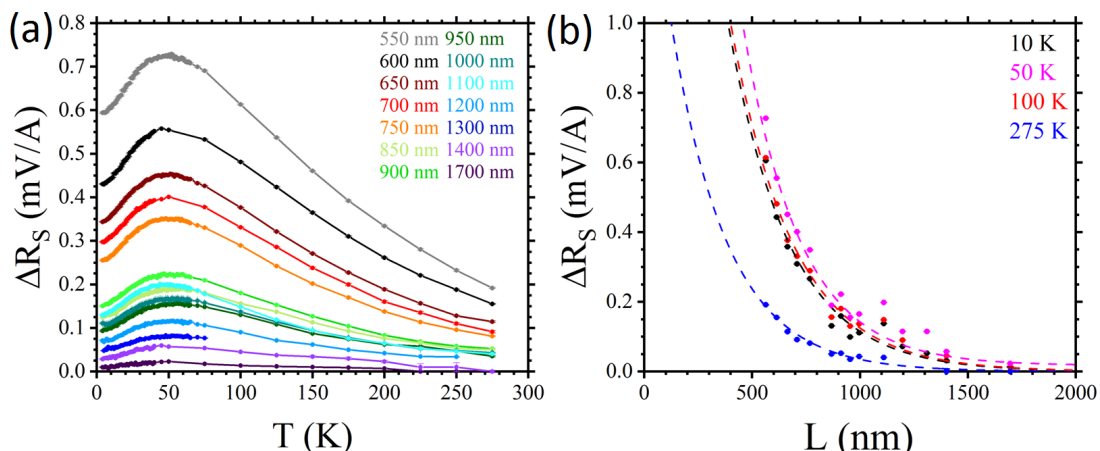


Figure 5.7: **(a)** The spin signals for each of the Py/Cu devices plotted against temperature. The lines connecting the data points are guides for the eye. **(b)** shows the spin signal for each injector-detector separation for four different temperatures. The dashed lines are fits to Eq(2.41).

The spin signals for each of the Cu devices can be seen in Fig.5.7(a). After the first few devices were measured it became apparent that the peak in the spin signal occurred at a much higher temperature than it did in the Ag – and so the spin signals were measured at every 1 K up until 75 K.

Importantly, the reduction of the spin signal at low temperatures occurs for all of the devices, including the 550 nm device which did not exhibit a Kondo upturn. If the downturn were due solely to magnetic impurities, then it would be expected that the 550 nm device would have a much less apparent peak than the rest of the dataset.

In Fig.5.7(b), the decay of spin signal over distance is more clearly shown. Just as with the Ag devices, the spin signal decays exponentially with injector-detector separation – in accordance with the Valet-Fert model for spin diffusion. Unlike the Ag devices, however, the spin signals at 100 K are almost identical to those at 10 K, which demonstrate the extent to which the spin signal is suppressed at low temperatures in the Cu devices.

The fits to Fig.5.7(b) return the spin diffusion length for the Cu devices, which can be seen in Fig.5.8(a). The spin diffusion length is much shorter than that measured in the Ag ( $\sim 325$  nm versus  $\sim 650$  nm for the Ag at 50 K) despite the resistivity being lower. The significant downturn at low temperatures is also present, but the peak

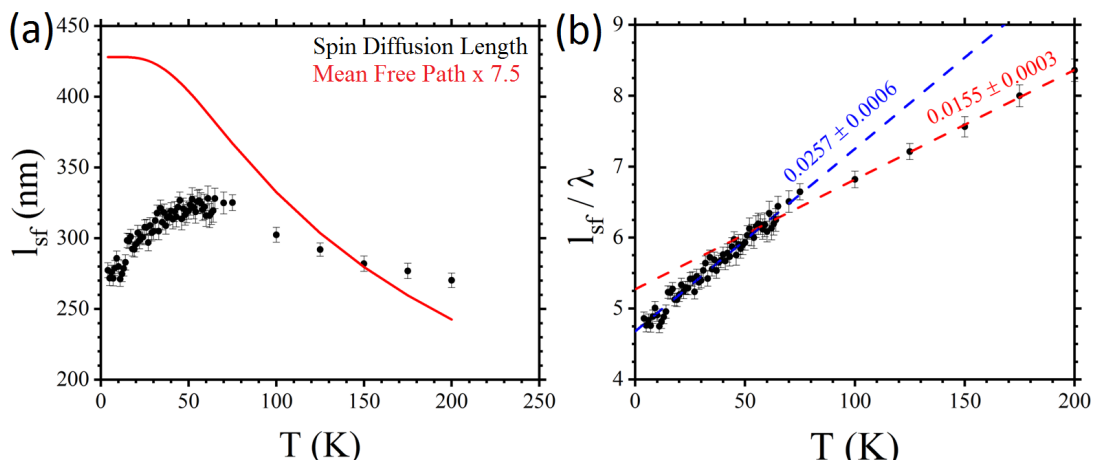


Figure 5.8: (a) shows the spin diffusion length for the Py/Cu LSVs in black, as determined by fitting Eq(2.41) at each temperature. In red is the mean free path of the Cu, determined by converting the average resistivities from Fig.5.6(a) using Eq(5.1), multiplied by 7.5. (b) The ratio of the spin diffusion length and mean free path. The red dashed line is a linear fit to the data above 75 K while the blue dashed line is a linear fit to the data below 75 K.

temperature is significantly higher - around 60 K in the Cu as opposed to 35 K for the Ag. It should be noted that in Fig.5.6(b) the observed Kondo upturn began at around 12 K – significantly lower than the point at which the spin diffusion length peaks.

As for the Ag, Eq(2.42) was used to calculate the spin resistances in order to apply the Valet-Fert fit. Again,  $w^{F1}$ ,  $w^{F2}$  and  $w^N$  were determined by averaging the values from each of the devices, obtained by SEM imagery:  $w^{F1} = 160 \pm 10$  nm,  $w^{F2} = 130 \pm 10$  nm and  $w^N = 170 \pm 9$  nm.  $t^N$  was again determined by XRR analysis of a thin film grown at the same time, with a value of  $110 \pm 10$  nm.

Just as with the Ag devices, the spin diffusion length decayed at higher temperatures once electron-phonon scattering began to dominate; however, in Fig.5.8(b), it is evident that, in contrast to the Ag, the ratio of the spin diffusion length to the mean free path is, at no temperature range, temperature independent.  $\chi^2$  analysis of the linear fits to the low and high temperature regimes yielded adjusted  $R^2$  values of 96.1% and 99.9% respectively.

This demonstrates that the Cu nanowires grown in this study do not exhibit EY spin-flip scattering at any point – in direct contrast to the observations made by Vil-

lamor [73]. The discrepancy is most likely caused by the pause during the growth of the Cu in this study and the relatively high pressures during deposition. The crystal structure has been disrupted to such an extent that the assumptions made in the EY model are no longer valid.

As a result, there is no single value with which the mean free path can be reasonably scaled, to map onto the spin diffusion length for a comparison of the two - they do not have the same temperature dependence at any point. An arbitrary value of 7.5 has been used to scale the mean free path in Fig.5.8(a) so that the shapes of the two curves can be compared. It is not possible with the Cu devices, to calculate a single value for the spin-flip probability.

Moran also observed a significant deviation between the spin diffusion length and mean free path in their CoFe/Cu LSVs [6], grown on the same deposition system as those in this study and in Batley's study [5] – suggesting that Cu is much less likely to obey EY scattering than Ag.

## 5.4 Conclusions

Two sets of lateral spin valves were grown, Py/Ag and Py/Cu, in an attempt to resolve an ongoing dispute in the field of spintronics, about whether a low-temperature decrease in the spin diffusion length within some noble metals could be explained by Kondo scattering induced by magnetic impurities [2–4, 20, 44, 55, 67, 69]. Both sets of devices were grown with six 9s pure source material in an attempt to reduce the amount of inherent magnetic impurities as much as possible.

In light of Stefanou's study [4], the silver was grown at a rate of  $0.4 \text{ \AA s}^{-1}$  which had been shown to almost completely eradicate the low temperature downturn because of a reduction in grain boundary scattering, while the Cu devices were grown using the same source material as in Batley's study [3] which they had found resulted in a much smaller downturn than in other Cu LSVs.

The original hypothesis was that an alternative explanation for a reduction in spin diffusion at low temperatures could be given; that an increase in low temperature spin-flip scattering was caused by a less ordered crystal structure within the non-magnetic channel. Such disorder could be introduced by grain boundaries [4], surface scattering [44, 55] magnetic [3, 67] and also non-magnetic impurities.

In order to test this hypothesis, both sets of lateral spin valves were purposefully

doped with gaseous impurities, ambient to the deposition chamber, by pausing the evaporation of each respective noble metal midway through deposition. Mass spectrometry indicated that the most dominant impurity at the time of growth was  $N_2$  for both sets of devices.

Close inspection of the electrical resistivity yielded no measurable Kondo scattering in the Ag to a precision of 0.002 %, while measurements of the Cu indicated inconsistent levels of Kondo scattering - up to 0.02 % increase in the resistivity in most, as opposed to no discernible increase in the 550 nm device. It has to be concluded, therefore, that the Ag channels contained insignificant numbers of magnetic impurities while the Cu channels varied from device to device. The variance in the Cu suggests that the magnetic impurities must have originated during the deposition process rather than being native to the source material, in agreement with Villamor [2] and O'Brien [20].

According to the argument that Kondo scattering can fully explain the downturn observed in  $l_{sf}$ , the Ag devices should not have exhibited a downturn, whereas a minor downturn would be expected in the Cu devices. In fact, a significant deviation from the expected spin diffusion length was observed in both sets of devices – more so in the Cu, which is not unexpected since the pressures were higher during deposition.

Additionally, the fact that a downturn was observed equally in all of the Cu devices' spin signals while, in contrast, one exhibited no Kondo effect in its resistivity measurements, further reinforces the idea that the reduction in spin diffusion cannot be explained by Kondo scattering alone. Additionally, the temperature at which the downturn started in the Cu ( $\sim 60$  K) was significantly higher than the temperature at which the Kondo upturn began in the measurements of  $\rho$  ( $\sim 12$  K).

Furthermore, an analysis of the temperature dependence of the spin-flip scattering in the Ag devices showed that it closely followed the EY model at higher temperatures but that below 50 K, the spin-flip scattering deviated from that predicted by the mean free path measurements. The temperature dependence of the deviation could be equally fitted with a linear or logarithmic shape, with the Kondo shaped fit yielding a Kondo temperature of  $64 \pm 2$  K – significantly different to the accepted value for Fe impurities in Ag.

In the Cu, however, comparison of the spin diffusion length with the mean free path yielded no agreement with the EY model, suggesting that the spin-flip probability of scattering was heavily-temperature dependent, in contrast with previous studies [73].

Such a temperature dependence to the spin-flip probability could explain the origin of the downturn in the spin diffusion length measurements.

Although other studies have demonstrated reliable adherence to the EY model in noble metals [2, 44], these two sets of devices demonstrate that for Ag and Cu, when the crystal structure is disrupted by the introduction of ambient impurities, the assumption that the spin-flip probability remains temperature independent does not hold. This is in agreement with the initial boundaries set by Elliott and Yafet in their original works [23, 38, 39]. It was outlined from the start that the more disordered a metal, the less valid the EY approximations became [11].

In each of the studies mentioned in the literature review, the variations between devices almost always involved a reduction in the quality of the non-magnetic channel's crystal structure, which then resulted in a downturn in the spin diffusion length. This study has provided very strong evidence that it is the crystal structure as a whole which is responsible, and that the EY model cannot be wholly relied upon in more disordered devices – as originally predicted. It has also shown that the downturn can just as easily be explained by introducing a temperature dependence to the spin-flip probability, as by claiming suppression by some otherwise unobserved magnetic impurities.

It is also interesting to observe that deviations to the expected thermal signals presented in chapter 4, occurred at a similar temperature range to the deviations observed in the spin transport measurements discussed here. It seems a strong coincidence that both the thermal and spin transport properties of both Cu and Ag independently diverge from original expectations for temperatures below 50 K. It is possible that the central channels in both sets of devices undergo a transition from 3-dimensional to 1-dimensional systems once their temperature is reduced sufficiently. Such a transition would change the transport mechanisms for both phonons and electrons within the nanowires and could explain the varying temperature dependencies. A detailed study into varying both the widths and thickness of the central channels in LSVs would be a prudent investigation.

Finally, the pause introduced midway through the evaporation of the non-magnetic channels has been shown to significantly diminish the spin-transport properties of both sets of devices – most likely by disrupting the crystal structure through the binding of ambient impurities such as  $N_2$  to the metallic lattice. This raises issues for the ‘delta layer’ doping technique seen in studies such as Stefanou’s [4], in which the growth of the

main material is paused while a doping material is added. This study shows that the surrounding gaseous molecules can significantly effect the spin-flip scattering observed in the non-magnetic channel, if allowed to settle during a pause to deposition – further highlighting the sensitivity of spintronic devices to their growth conditions.

---

# CHAPTER 6

---

Novel Deviations to Low Temperature DC NLIVs

## 6.1 Gaussian Peaks Centred At Zero Current

---

As demonstrated in previous chapters, the non-local measurements of the two sets of LSVs returned IV curves that were mostly quadratic in nature. The measurements were subsequently fitted with Eq(4.1) and further analysis showed that the quadratic term most likely represented a Seebeck signal caused by Joule heating in the Py injector.

The linear term could be separated into magnetically dependent and independent constituents, the first of which represented the accumulation of spins at the detector's interface due to spin diffusion from the site of spin injection. The field-independent component was argued to be caused by Peltier heating at the injection interface.

However, closer inspection of the NLIVs revealed that there was an additional signal in the voltage, centred at zero applied current, that was not described by the quadratic model. Few available studies reference this signal – partly because many studies into LSVs utilise AC measurements.

Stefanou's study does, however, touch upon the issue [4]. It was observed that when Py/Ag LSVs were purposefully doped with Fe impurities, a significant deviation from the quadratic shape was observed, centred at zero applied current, for temperatures below 25 K. They argued that, because the signal was so prominent in Fe doped devices, it was most likely related to the Kondo effect caused by small amounts of Fe in the Ag. In order to adjust for the deviation, they separated out their fits for positive and negative applied currents. Stefanou described the signals as 'W' shaped NLIVs because of their appearance.

In a study by Moran [6], a different deviation was observed. They grew CoFe/Cu LSVs and found that, close to zero applied current, an additional negative signal was observed - opposite to that seen in Stefanou's study. They argued that because the shape of the IV could be better fit with higher order polynomials, the signal was most likely caused by additional self-interacting thermal signals (i.e. that the heat produced in the injector was changing the properties of the device mid-measurement). The appearance of the IVs in Moran's study was closer to that of a letter 'V'.

The apparent differences between the observations found in the two studies mentioned shows that a more thorough and comprehensive study of the signal is required.

## 6.1 Gaussian Peaks Centred At Zero Current

In Fig.6.1(a), NLIVs for both a Cu and Ag device can be seen. The quadratic fits have been applied as before and it can be clearly seen that close to zero applied current,

## 6.1 Gaussian Peaks Centred At Zero Current

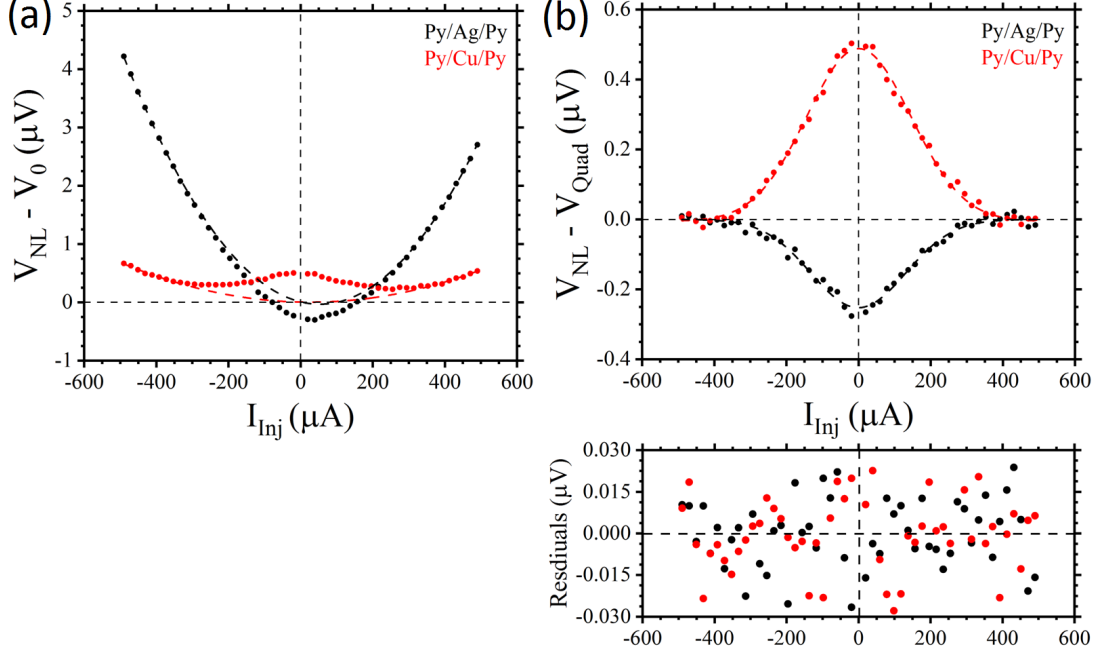


Figure 6.1: **(a)** Two non-local IVs for the 650 nm Py/Ag device at 4 K (black) and the 550 nm Py/Cu device at 5 K (red), both in the anti-parallel spin state. The dashed black and red lines are fits to Eq(4.1). Both signals have had the current-independent term from those fits subtracted to allow for a closer comparison of the two. **(b)** shows the same two IVs, but with the entire quadratic fit subtracted. The dashed lines are fits to Eq(6.1). Beneath, are the regular residuals to both the fits in the same colours.

the voltages differ significantly from the purely quadratic shape. Significantly, here the Ag's IVs are 'V' shaped while the Cu has a characteristic 'W' shape; in direct contrast to Stefanou's and Moran's findings, which indicates that the direction of the signal is not material dependent and instead must have a different root cause.

Fig.6.1**(b)** shows the difference between the observed voltages and those predicted by the quadratic model. Both deviations have the appearance of a Gaussian peak and as a result, have been fitted with

$$V = h e^{-(I-I_0)^2/2w^2} \quad (6.1)$$

where  $h$  is the height of the peak,  $I_0$  is the current-offset of the peak's centre and  $w$  is the width of the peak.  $\chi^2$  analysis of the two fits yielded adjusted  $R^2$  values of 97.9%

## 6.1 Gaussian Peaks Centred At Zero Current

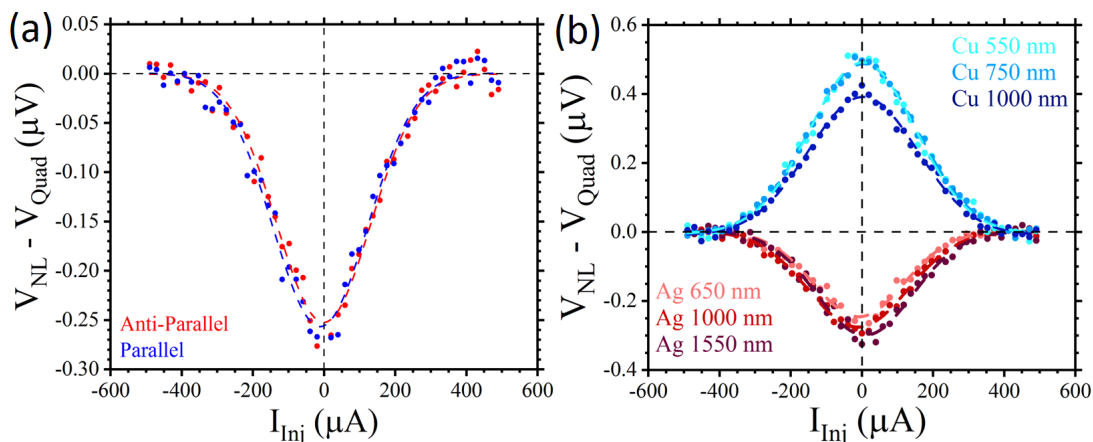


Figure 6.2: (a) The deviation from the quadratic model for the 650 nm Ag device at 4 K, for both the parallel (blue) and anti-parallel (red) spin states. The dashed blue and red lines are fits to Eq(6.1). (b) shows the signal for both the Cu and Ag devices for a selection of their respective device separations (the Ag at 4 K, the Cu at 5 K).

and 99.3 % for the Ag and Cu respectively.

The residuals left over from the two fits show that although the peaks may not physically represent a normal distribution, the Gaussian formula statistically explains the distribution of the two datasets well. The description of these peaks as Gaussian in this study merely refers to their appearance and does not imply anything with regards to their physical nature.

The peak's dependence on an applied magnetic field is shown in Fig.6.2(a). When the Ag LSV switches from its parallel spin state to anti-parallel, there is no visible change in the zero-current signal. A fair conclusion to make therefore, is that the peak does not originate from the movement of spins within the device.

In Fig.6.2(b), the effect of injector-detector separation on the signal is explored. Data for both the Cu and Ag devices are shown and neither set shows a clear or obvious trend with respect to length.

Fig.6.3(a) and Fig.6.3(b) demonstrate the temperature dependence of the signal. In the Ag, the non-quadratic voltage has almost entirely disappeared by 30 K, and similarly so in the Cu. However, as the devices are warmed towards room temperature, a very small peak, positive in amplitude for both materials, forms. Additionally, the current at which the high-temperature peak is centred appears to move to a more

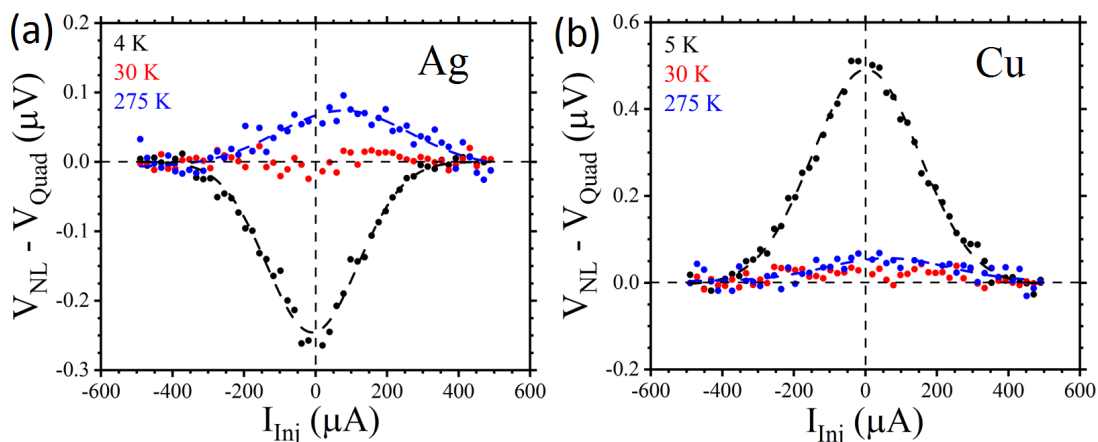


Figure 6.3: (a) The Gaussian signal for a range of temperatures for the Ag device with a separation of 650 nm. The dashed black and blue lines are fits to Eq(6.1), while the 30 K data could not be properly fitted. (b) is the same graph but for the Cu device with a separation of 550 nm.

positive current bias in both cases.

The temperature dependence at low temperatures can be more clearly seen in Fig.6.4(a) and Fig.6.4(b) for the two sets of devices. Generally, the peaks are at low temperatures, decaying to effectively zero by 25 K. As seen in Fig.6.1(a) and Fig.6.1(b), the direction of the peaks for the Cu and the Ag are opposite in magnitude; that is, except for the 800 nm and 900 nm Ag devices which behave drastically different to the rest of their dataset.

The 800 nm and 900 nm Ag devices exhibit a positive Gaussian signal, similar to that seen in the Cu, further evidence that the direction of the peak is not material dependent. In Fig.6.5 the uniqueness of the two outliers can also be seen. Here, the peak height for all of the devices has been plotted at 5 K versus their device separation. While the peak height in the Ag devices appears to be independent with regards to distance from the injector, the Cu devices exhibit a strong length dependence – with the signal getting weaker at longer distances.

It may be inferred that the mechanisms behind the positive and negative peaks are different. The behaviour of the Ag devices suggests that the Gaussian peak originates at the site of detection, since the length of the Ag channel has no effect on the size of the signal measured. In contrast, the Cu devices behave in a manner more indicative

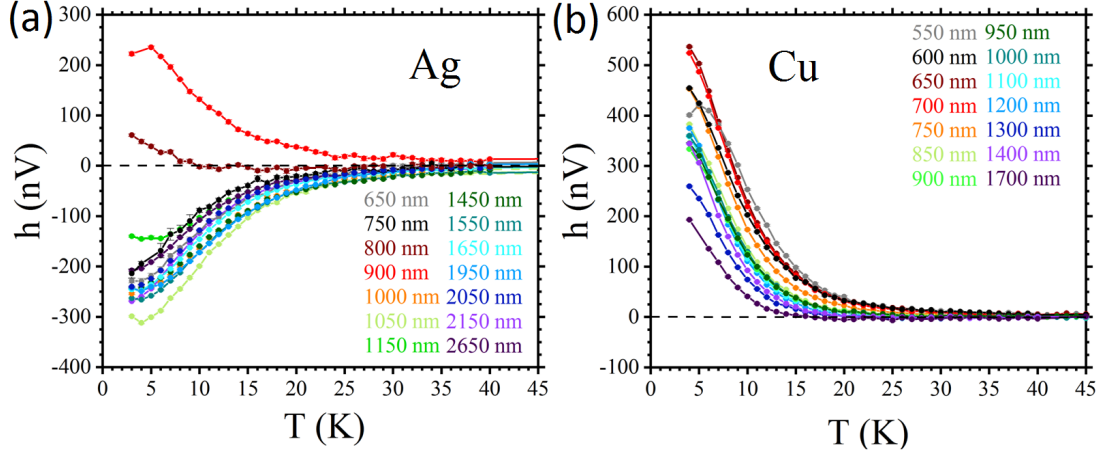


Figure 6.4: (a) shows the height of the Gaussian peak for each of the Ag devices, as calculated from fits to Eq(6.1) for temperatures up to 45 K. The lines connecting the data points are simply guides for the eye. (b) is the same graph but for the Cu devices.

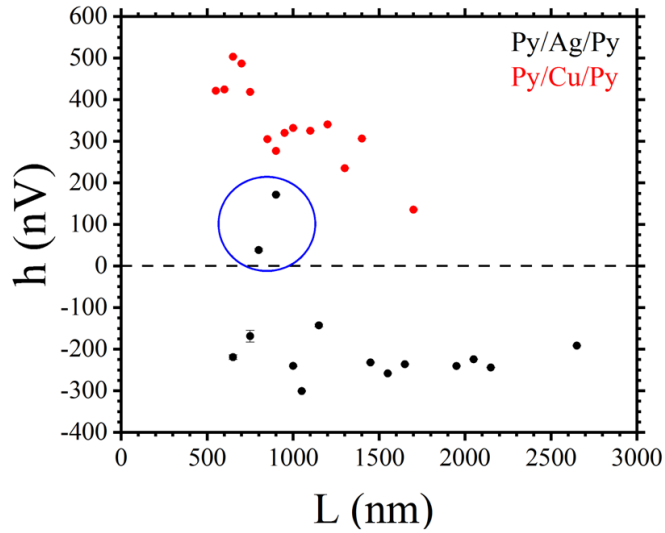


Figure 6.5: The average height of the Gaussian peak as found from fits to Eq(6.1), for each device at 5 K. The black data are the Ag devices and the red data the Cu. The blue circle highlights the two outliers from the Ag dataset.

## 6.1 Gaussian Peaks Centred At Zero Current

---

of the signal being produced at the site of injection, since the signal gets smaller with distance from the injector.

These two observations together suggest that both signals are originating at the interfaces between ferromagnet and non-magnet, as opposed to within the central channel. However, reference back to Fig.4.8(a) and Fig.4.8(b) casts doubt on this proposition.

Fig.4.8(a) and Fig.4.8(b) showed the quadratic parameter from fitting Eq(4.1), for each of the Ag and Cu LSVs which was attributed to Joule heating in the Py injectors. It was found that the Ag and Cu displayed contradicting temperature dependencies below 50 K because of the relative thermal conductivities of the central channels and the conductance of the interface with the substrate.

The Ag devices exhibited an increase in the amount of Joule heat that reached the detector below 50 K, despite the injector's resistivity remaining constant, because the efficiency of heat transfer into the substrate all but disappeared – resulting in a considerably warmer injector.

In the Cu, on the other hand, the rapid decrease of the Cu's thermal conductivity meant that below 50 K, relatively more heat was lost to the substrate and thus less reached the detector. As a result, the Joule heating signal fell at low temperatures.

It is therefore significant that the 800 and 900 nm Ag devices behave completely different to the rest of the samples from their fabrication, in regards to both their quadratic parameter AND their Gaussian peak height.

The temperature dependence of every single device's quadratic parameter, from both materials, maps onto the direction of its deviation from a quadratically shaped IV. i.e. when the amount of heat that reaches the detector increases at low temperatures, a negative deviation is observed, and vice versa for a reduction in the amount of heat at the detector.

From these observations it is concluded that the mechanisms leading to the Gaussian peaks are closely related to the thermal properties of the non-magnetic channels, despite the length dependence of the signals pointing towards an interfacial effect. Additionally, Stefanou's conclusion that the effect was dependent on the presence of magnetic impurities [4] can be now discounted, since the 800 and 900 nm Ag devices, which exhibited 'W' shaped IVs, exhibited no measurable Kondo effect in their resistivity.

## 6.2 Measurement Artefacts

One confusing aspect about the Gaussian signal is that it is, for the most part, centred at zero applied current. A more intuitive expectation would be for the effect to grow as more current is injected (as seen with the other extracted signals). A possible explanation for the peak is that it is a measurement artefact – for example, if the potential difference exists externally to the devices, such as in the wiring or electrical contacts for the measurement. This would explain why, as more current is applied to the devices, the effect becomes negligible with respect to the other signals.

A simple experiment was conducted to measure the same device with a variety of different wiring configurations, such that any voltages external to the LSV could be isolated and accounted for. The Py/Cu device with a separation of 700 nm was used for such a test.

In Fig.6.6(a), the NLIVs for four different measurement configurations, at 7 K, are shown. A measurement was made as normal, followed by another with which the voltage terminals were switched. Next, a measurement was made where the injector and detector were swapped and then, finally, a standard measurement was performed with a larger injection current.

One source of suspicion is that the ‘V’ shaped deviation looks almost identical to the ‘W’ signal, except flipped. A possible reason for measuring the exact same signal, but with a negative sign, would be if the terminals of the voltmeter are attached the opposite way round. Now, despite great care being taken when setting up measurements, to always wire up the voltmeter the same way, it is not inconceivable that occasionally, on a late evening, the positive and negative terminals of the voltmeter were attached the wrong way round.

As a result, it was of importance to check that, when the voltage terminals were intentionally switched, the overall shape of the NLIV remained the same. In Fig.6.6(a) and Fig.6.6(b) it can be seen that the red data for Config B (once multiplied by -1) has exactly the same shape as the original measurement in black. As a result, the signal being an artefact originating at the voltmeter can be discounted.

Another possible experimental mistake that could be made, would be to accidentally pass the current through the detector instead of the injector (i.e. to switch the two Py electrodes) which, because of their different geometries, would lead to a change in the thermal signals produced. This could be a possible explanation for some of the devices

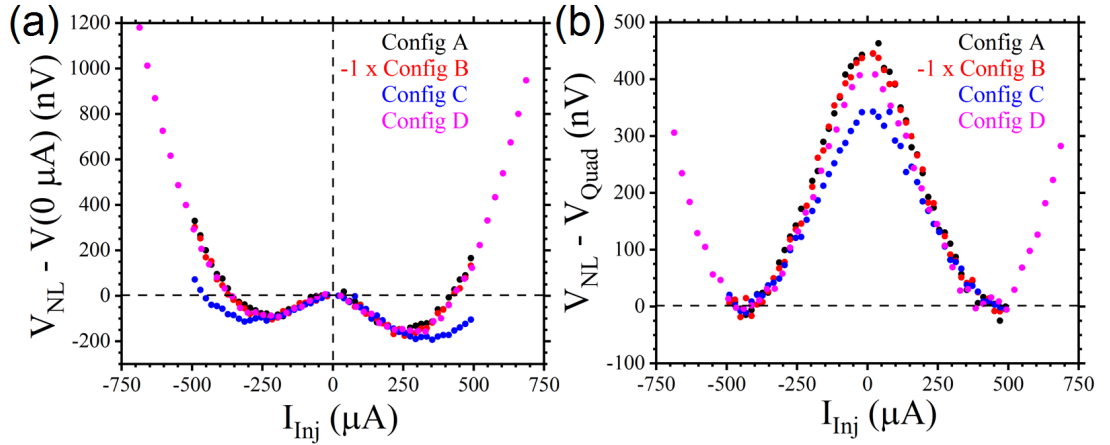


Figure 6.6: **(a)** Four NLIVs for the 700 nm copper device at 7 K. Config A is the same wiring configuration as the rest of the NLIV measurements from this study. The current is passed from the injector into the Cu channel, while the voltage is measured across the detector's interface. Config B is the same measurement, but with the positive and negative terminals of the voltmeter switched. Since this results in a negative voltage, the signal has been multiplied by -1 for comparison. Config C is the same as Config A, except that the current has been injected into the Cu from the detector (which is larger than the injector), while the voltage was measured across the injector's interface. Config D is the same as Config A, except that larger currents were injected; the current was swept between  $\pm 700 \mu A$ . For all four measurements, the voltage at zero current has been subtracted to provide better comparison. **(b)** here, quadratic fits to the four IVs in **(a)** have been subtracted, leaving only the Gaussian signal.

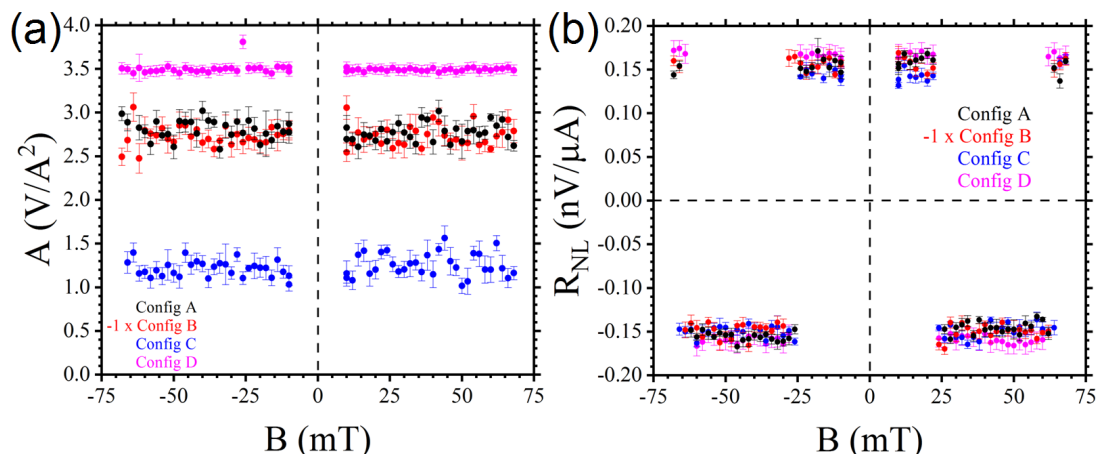


Figure 6.7: **(a)** The quadratic parameter from fits to Eq(4.1) for each of the four configurations outlined in Fig.6.6(a), for the full range of applied magnetic field strengths. **(b)** The values of the linear parameter from the same quadratic fits.

exhibiting wildly different deviations relative to others from the same fabrication.

This was intentionally recreated with Config C (blue data). In Fig.6.6(a) and Fig.6.6(b) it can be seen that switching the injector and detector does indeed lead to a differently shaped NLIV. The quadratic term is smaller, and therefore the resulting Gaussian deviation is also less apparent. In Fig.6.7(a) it can be more clearly seen, where for each of the applied field strengths, the quadratic parameter is noticeably smaller for Config C.

This can be explained by the fact that the detector is larger than the injector and will result in a smaller current density and less electrical resistance. According to Eq(2.47), less resistance leads to less Joule heating and, consequently, a smaller Seebeck signal.

However, it should be noted that switching the injector and detector did not completely reverse the sign of the Gaussian deviation and, as a result, cannot explain the anomalous behaviour of the 800 and 900 nm Ag devices. Additionally, in Fig.6.7(b) it is clear that switching the two ferromagnets did not result in any change to the spin switching when compared to the normal measurement – which is a useful observation with regards to future experiments.

Finally, it was tested to see whether the amount of current injected would affect the Gaussian signal in any way. For Config D (in magenta)  $\pm 700 \mu A$  was applied instead

of  $\pm 500 \mu\text{A}$  and it can be seen in Fig.6.6(a) that the shape of the NLIV remains very similar. However, closer inspection of Fig.6.6(b) shows that, for currents larger than  $500 \mu\text{A}$ , the measured voltage begins to deviate from that predicted by Eq(4.1).

This deviation at larger currents agrees with Moran’s hypothesis that when the amount of heating within the device increases to significant levels, higher order polynomials begin to dominate [6]. For currents above  $500 \mu\text{A}$ , the device is no longer in thermal equilibrium and its thermal properties begin to change mid-measurement. Notably, the non-equilibrium heating during the Config D measurements, appear to have had little to no effect on the spin switching of the device. In Fig.6.7(b), the switches with larger injection currents behave identically.

### 6.3 Non-Equilibrium Heating

In order to test Moran’s theory that non-equilibrium heating within LSVs leads to higher polynomial terms in the NLIVs, a simple test can be performed. To account for the device warming up during each measurement a slower sample rate can be used, which should allow the device to sufficiently cool in between each current injection.

In Fig.6.8(a), the effect of varying the sample rate on the shape of the NLIV is explored. Firstly, the measurements were taken at a rate three times slower (red data), yielding no visible change to the shape of the zero-current centred peak, suggesting that the unexplained signal is not related to warming within the device.

This is reinforced by the blue data. Here, the usual current sweep has been repeated four times (back to back) and yet for each sweep, the same Gaussian peak is observed. If the signal were due to heating within the device, it would be expected that, as each sweep was performed, the shape of the NLIV would adjust as it warmed.

For the magenta data, the injection current was held at a constant value for 150 s, while the voltage was measured every 3 s for a total of 51 measurements per current value. Apart from an apparent outlier at  $250 \mu\text{A}$ , the shape traced out by the voltages is the same as those made by sweeping the current. Even when the voltage is measured for individual current values, the distinctive Gaussian peak is present in the signal drawn out. Therefore, it cannot be related to non-equilibrium heating within the device.

In Fig.6.8, the change in the measured voltage over time, while held at the same current, is shown. Although there is a slight upwards trend to the data (which suggests that the device is warming up over time), the change is roughly  $0.1 \text{ nV per s}$ . The

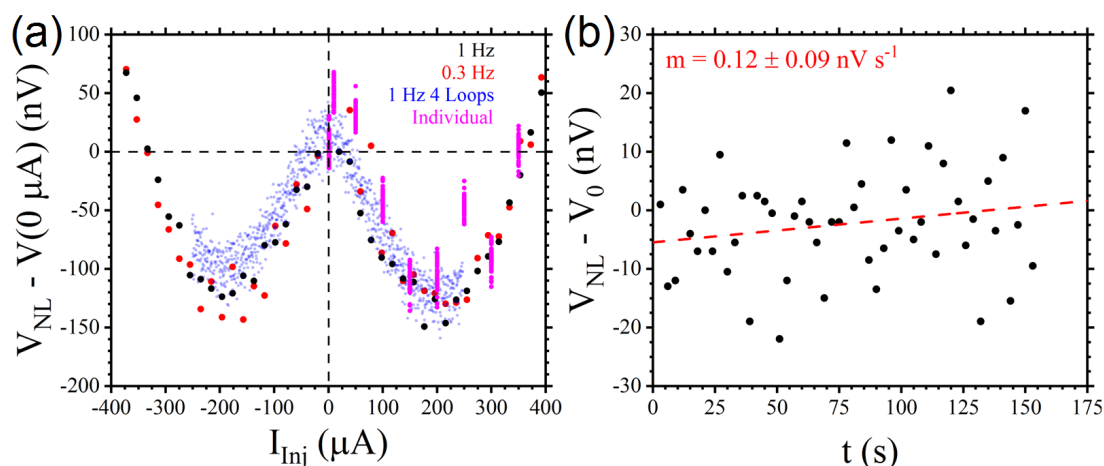


Figure 6.8: **(a)** Four NLIVs of the 700 nm copper device at 7 K. For the black data, a measurement was made every second for the full 51 current-value sweep. For the red, a measurement was made every 3 s. The blue data were taken at the same speed as the black data, but the sweep was looped four times for a total of 204 measurements. The magenta data were measured at individual current values, rather than sweeping through a range. At each current value, 51 measurements were made (once every 3 s). The device was then allowed to thermally settle for one minute, before the next measurement at the next current was made. For all of the NLIVs, the voltage at zero applied current has been subtracted to allow for better comparison. **(b)** shows the voltage as a function of time, during the measurement at  $350 \mu\text{A}$  from the magenta dataset. The dashed red line is a straight-line fit to the data and its gradient has been marked in the top-left.

Gaussian peak in Fig.6.8 has an amplitude of approximately 250 nV, which would equate to around 40 minutes of heating. It is fair to say then, that the rate of warming within the device when injecting 350  $\mu\text{A}$  is negligible with respect to the magnitude of the other signals measured.

An additional test can be performed with regards to non-equilibrium heating within the devices: to gradually ramp up the injection current as high as possible, to see whether the Gaussian peak at zero current changes shape. Fig.6.9 shows the relevant results.

For the 700 nm copper device, at 7 K, the maximum current of each sweep was increased, after each measurement, in increments of 50  $\mu\text{A}$ , until the magnitude of the current density became so great that the device was irreversibly damaged. A sample of sweeps has been shown in Fig.6.9 to demonstrate how the behaviour of the NLIVs within the device changed as more current was applied. A quadratic fit to the 750  $\mu\text{A}$  measurement has been included, to allow for better comparison between the different measurements at large currents.

In the inset, the low-current behaviour of each measurement is the same between  $\pm 0.5$  mA, demonstrating that, even after the measurement taken preceding the 5.300 mA sweep, the behaviour of the device had not changed. This indicates that large current densities do not lead to permanent structural changes (that result in a change to the thermal properties) within the devices which is of use to further studies regarding LSVs.

In addition, there is significance in the deviation from the quadratic at currents larger than  $\sim 1$  mA. Both the blue and magenta sets disagree with the dashed red quadratic fit at larger currents, demonstrating that the device is no longer in thermal equilibrium and that higher order polynomials have begun to play a significant role. However, this contradicts with Moran's conclusion that higher-order terms played an important role at lower injection currents.

## 6.4 Conclusions

A deviation from the expected quadratic-shaped NLIVs for two sets of noble metal lateral spin valves (Py/Ag and Py/Cu) was closely studied. Both sets of devices had been purposefully doped with ambient impurities during deposition - mostly  $\text{N}_2$ .

In the Ag devices a negative, Gaussian-shaped peak was observed between  $\pm 400$   $\mu\text{A}$ , while in the Cu devices an almost identical, but positive, Gaussian peak was meas-

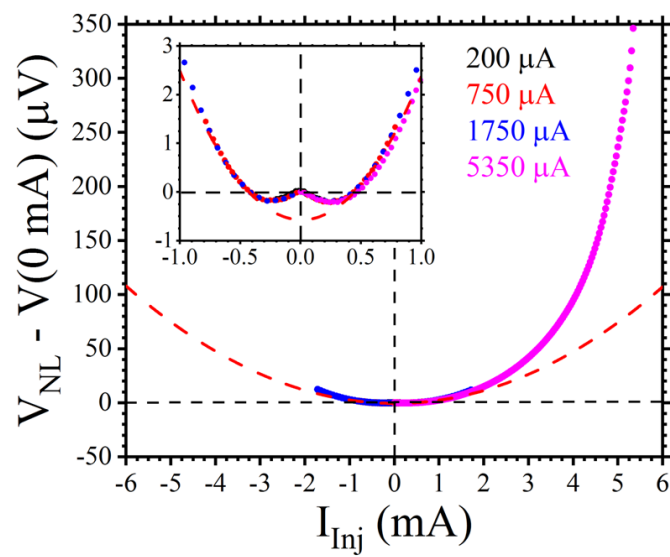


Figure 6.9: Four NLIVs of the 700 nm copper device at 7 K. For the black, red, blue and magenta data, the current sweeps were applied between  $\pm 200$ ,  $\pm 750$ ,  $\pm 1750$  and  $\pm 5350$   $\mu\text{A}$  respectively. During the  $5350$   $\mu\text{A}$  measurement, electrical contact was lost with the device and the negative part of the sweep could not be completed. The dashed red line is a fit to Eq(4.1) for the  $750$   $\mu\text{A}$  data. The inset shows a closer look at the signals measured for low currents. For each of the NLIVs, the voltage at zero applied current has been subtracted.

ured. The Gaussian signal demonstrated zero magnetic-field dependence, indicating that it was not caused by spin accumulation within the LSVs. In both materials, the deviations disappeared rapidly as the temperature increased from 3 K up to 30 K. At temperatures closer to room temperature, a small positive peak was observed in both sets of devices.

By looking carefully at the size of the peak heights with respect to temperature and separation, it was shown that two of the Ag devices (800 and 900 nm respectively) exhibited a positive peak (identical to the Cu), unlike the rest of the devices from the same fabrication. This was reflected in the behaviour of their quadratic parameters. Both devices' quadratic term diminished at low temperatures instead of increasing, unlike the rest of the Ag LSVs.

In this study there was a 100 % correlation between the temperature dependence of the quadratic term below 50 K and the direction of the Gaussian deviation from the quadratic fit. A low-temperature rise in the quadratic parameter was always reflected by a negative Gaussian peak and vice-versa, suggesting that the origin of the signal is related to the thermal conductivity of the central channel.

Importantly, there was no correlation between the direction of the Gaussian peak and whether the resistivity measurements of each device demonstrated Kondo scattering from magnetic impurities – in direct disagreement with Stefanou's conclusion [4].

Strangely, a significant length dependence was found in the height of the Cu's signal, while no measurable dependence was seen with the Ag. This observation suggests a conclusion that the signals originate at the interfaces between the non-magnet and ferromagnet since, if the signal were being produced in the central channel, a longer injector-detector separation would yield a stronger deviation.

Further tests were performed in which the wiring arrangement, measurement speed and injection current were varied. It was found that the arrangement of the positive and negative terminals of the voltmeter had no effect on the shape of the NLIVs, confirming that the signal originated within the device itself.

There was an observable change, however, when the injector and detector were swapped, which adds more weight to the argument that the signal is thermal – because of the detectors' different thermal properties.

When a larger injection current was applied, an additional deviation from the quadratic term was observed, which initially agreed with Moran's theory that non-

equilibrium heating from large current densities was leading to higher-order polynomial terms. By varying the measurement speed, it was shown however, that even when the device was given time to cool between individual voltage measurements, the same Gaussian peak was observed. It is hard then, to justify the idea that the peak is caused by rapidly changing thermal properties within the device.

Additionally, when significantly larger currents were injected (over 5 mA), the behaviour of the Gaussian peak remained identical until the moment the device was irreversibly damaged. So, according to the evidence put forward in this study, it can be concluded that the deviations seen at low currents cannot be explained as measurement artefacts, magnetic effects, or as originating from non-equilibrium heating within the devices.

The most significant evidence comes from the relation between the Gaussian deviation and the temperature dependence of the thermoelectric voltage at low temperatures. The fact that a 100 % correlation between the two was observed is a clear indication that the signal seen at low injection currents is dependent on the thermal properties of the central channel and substrate.

---

# CHAPTER 7

---

Final Conclusions

---

Two sets of LSVs were fabricated: Py/Ag and Py/Cu. For the first time, a direct comparison has been made between the two most widely used combinations of constituent materials in LSVs. The fabrication process was consistent between the two sets of devices and they were measured in exactly the same way.

A case has been put forward in chapter 4 that the key to understanding some of the more unintuitive observations within LSVs, is to take significantly larger numbers of data points per sample set than have been made in previous studies.

By performing 10s of thousands of DC IV sweeps, at hundreds of magnetic field strengths, at temperature intervals of only 1 K, for at least 15 separate devices per fabrication, a much clearer picture of the behaviour of the spin valves has been revealed.

A model for thermal diffusion within LSVs, presented by Stefanou et al., has been applied to the thermal voltages measured within this study's devices and found to have applied well to the data. Exponential fits were obtained for both quadratic Joule heating term and the linear Peltier heating term down to as low as 4 K – where previous studies had failed to obtain low temperature fits to the minute Peltier signals [1, 6].

Through application of the model, an explanation for the low temperature variation to the amount of Joule heating measured at the detector between Cu and Ag was formed. The relatively higher thermal conductivity of the Cu when compared to the Ag, led to a much sharper decrease at low temperatures, shortening the Cu channel's thermal diffusion length and reducing the magnitude of the thermal voltage seen at the detector.

Despite this, there is still some uncertainty pertaining to the fact that the model predicts a different thermal conductance between the central channel and the SiO<sub>2</sub> substrate for Joule and Peltier heating respectively. Although a previous study has argued this is because of ballistic phonon transport there is little additional evidence from this study to support such a conclusion [1].

With regards to spin transport, arguably the most complete temperature dependence of the spin diffusion length for two sets of lateral spin valves has also been presented, by application of the 1-dimensional Valet-Fert model to the decay of the device's spin signals over distance.

In chapter 5, it was shown that, in carefully grown Ag, the presence of magnetic impurities can be completely negated. The resistivity measurements of the Ag presented an extremely clear absence of Kondo scattering.

---

Furthermore, clear evidence has been presented that when ambient, gaseous, non-magnetic impurities are allowed to accumulate in the middle of the central channel of noble metals, the spin transport properties are significantly altered. Comparison with the devices grown by Stefanou [4] and Batley [5] show a clear and obvious downturn in the spin diffusion length.

The inconsistency that one of the Cu devices exhibited zero Kondo scattering adds weight to previous studies claiming that Py impurities could diffuse into the central channel during deposition [20]. However, it also significantly hampers the argument that those magnetic impurities cause a downturn in the spin signal, since even the Cu device void of any Kondo signal, demonstrated a very similarly-sized downturn to the spin signal at low temperatures.

The low temperature downturn has been shown to equate to a linear increase in spin-flip scattering with temperature below 50 K. Arguments have been put forward that, instead of assigning the increase to some unexplained scattering mechanism, the deviation is more easily described by a change in the behaviour of the spin-flip probability described by the Elliott-Yafet model.

A previous study that argued that the downturn could be caused by magnetic impurities, too weak to introduce a Kondo upturn [69] is contradicted because the downturn in the spin diffusion length has been shown to have a linear temperature dependence rather than the logarithmic nature predicted by the Kondo effect. Even if a Kondo fit is forced upon the data, it predicts a Kondo temperature significantly higher than that accepted for Fe impurities in Ag nanowires.

Ag has been shown to, for the most part, obey the EY model for temperatures above 50 K, while the Cu has indicated zero evidence for a temperature-independent spin-flip probability – most likely due to the disorder brought about by the gaseous impurities.

As an aside, it has become apparent that the method of intentional doping of metallic nanowires by pausing the growth midway, in order to evaporate the desired impurity, cannot be relied upon. The disruption of the growth of the non-magnetic material, even when no other impurity is purposefully introduced, has very significant implications for the spin transport properties within.

A deviation from the quadratic shape expected in NLIVs, also seen by Stefanou [4] and Moran [6], has been more closely scrutinised than ever before. The fact that

identically-shaped, but opposite in magnitude, deviations were observed in both the Ag and Cu devices, when their crystal structures had been disrupted, demonstrates that it is not a material dependent phenomena.

After fitting the deviations with the equation of a Gaussian peak and then carefully comparing the behaviour of the peak height with temperature and distance, it was observed that two outliers from the Ag LSVs (whose peaks were in the opposite direction to the rest of the Ag) also behaved drastically different with regards to the amplitude of the quadratic signal in their NLIVs.

The 100 % correlation that observed between the direction of the Gaussian deviation and the temperature dependence of the Joule heating term at low temperatures, shows that the deviation must be related to the thermal conductivity of the non-magnetic channel (since the Py injectors for the two sets of devices were the same).

Furthermore, a comparison of the NLIVs observed for a wide range of measurement techniques was put forward. The Gaussian peak was not significantly altered by rearranging the measurement configuration, nor did the supplied injection current drastically affect its behaviour. Even an attempt to permanently alter the structure of the devices with 5 mA of applied current, only managed to destroy the device before the shape of the Gaussian deviation changed.

These observations lead to the conclusion that the signal is not some side-effect or unwanted measurement artefact, but an actual, important thermal process within the central channel of lateral spintronic devices.

## 7.1 Outlook

Ever since their initial development 20 years ago, LSVs have provided an important new tool in the arsenal of the condensed matter physicist. They give a key insight into the behaviour of electrons as magnetic particles and open the way for the next generation of devices that will store data magnetically.

However, this study makes it clear that, while significant progress has been made, an understanding of the mechanisms at play within spintronic devices is far from complete. For the last 10 years, it has been widely accepted within the field that magnetic impurities define spin transport properties at low temperatures and yet, in this study, the evidence presented severely weakens most of the arguments put forward in previous studies.

The reliance on the EY model to describe the spin transport properties of metallic spin valves should be questioned, especially in devices where the crystal structure of the non-magnetic channel is not pristine. However, this offers an exciting opportunity to explore why the spin-flip probability could have such a strong linear temperature dependence at low temperatures.

The idea that there is a Gaussian signal present in the voltages measured across lateral spintronic devices which, as yet, remains unexplained, opens the door to a large amount of study across multiple combinations of ferromagnetic and non-magnetic materials.

Finally, the fact that low temperature anomalies are observed for a similar temperature range within: the thermal parameters of both Cu and Ag, the spin transport properties of both materials and deviations to the accepted quadratic nature of NLIVs, hints to the possibility that each of the phenomena explored in this study are intrinsically linked and may all originate from the same root cause – potentially providing a clue for future studies to build upon.

# BIBLIOGRAPHY

- [1] Stefanou G.K., Menges F., Boehm B., Moran K.A., Adams J., Ali M., Rosamond M.C., Gotsmann B., Allenspach R., Burnell G., and Hickey B.J. Scanning thermal microscopy and ballistic phonon transport in lateral spin valves. *Phys. Rev. Lett.*, 127(035901):1–6, 2021.
- [2] Villamor E., Isasa M., Hueso L.E., and Casanova F. Contribution of defects to the spin relaxation in Cu nanowires. *Phys. Rev. B*, 87(9):1–5, 2013.
- [3] Batley J.T., Rosamond M.C., Ali M., Linfield E.H., Burnell G., and Hickey B.J. Spin relaxation through Kondo scattering in Cu/Py lateral spin valves. *Phys. Rev. B*, 92(22):1–5, 2015.
- [4] Stefanou G.K. *Transport properties of lateral spin valves*. PhD thesis, University of Leeds, 2018.
- [5] Batley J.T. *Spin transport in lateral spin valves*. PhD thesis, University of Leeds, 2015.
- [6] Moran K. *Spin and thermal transport in lateral spin valves*. PhD thesis, University of Leeds, 2021.
- [7] Ashcroft N.W. and Mermin N.D. *Solid state physics*. Saunders College Publishing, College edition, 1976 (3-27).
- [8] Bader S.D. and Parkin S.S.P. Spintronics. *Ann. Rev. of Condensed Matter Phys.*, 1(1):71–88, 2010.
- [9] Johnson M. and Silsbee R.H. Coupling of electronic charge and spin at a

- ferromagnetic-paramagnetic metal interface. *Phys. Rev. B*, 37(10):5312–5325, 1988.
- [10] Johnson M. and Silsbee R.H. Spin-injection experiment. *Phys. Rev. B*, 37(10):5326–5335, 1988.
- [11] Jedema F.J., Nijboer M.S., Filip A.T., and van Wees B.J. Spin injection and spin accumulation in all-metal mesoscopic spin valves. *Phys. Rev. B*, 67(8):1–16, 2003.
- [12] Filip A.T., Jedema F.J., van Wees B.J., and Borghs G. Direct experimental comparison between the electrical spin injection in a semiconductor and in a metal. *Physica E*, 10(1-3):478–483, 2001.
- [13] Caballero J.A., Moreau C.E., Pratt W.P., and Birge N.O. Magnetoresistance of a planar spin valve with single-domain ferromagnetic probes. *IEEE Transactions on Magnetics*, 37(4):2111–2113, 2001.
- [14] Brataas A., Nazarov Y.U.V., and Bauer G.E.W. Finite-element theory of transport in ferromagnet-normal metal systems. *Phys. Rev. Lett.*, 84(11):2481–2484, 2000.
- [15] Pareek T. Pure spin currents and the associated electrical voltage. *Phys. Rev. Lett.*, 92(7):1–4, 2004.
- [16] Datta S. and Das B. Electronic analog of the electro-optic modulator. *App. Phys. Lett.*, 56(7):665–667, 1990.
- [17] Behin-Aein B., Datta D., Salahuddin S., and Datta S. Proposal for an all-spin logic device with built in memory. *Nat. Nanotech.*, 5(4):266–270, 2010.
- [18] Niknov D.E., Bourianoff G.I., and Gargini P.A. Power dissipation in spintronic devices out of thermal equilibrium. *Journ. of Superconductivity and Novel Magnetism*, 19(6):497–513, 2006.
- [19] Kimura T. and Otani Y. Large spin accumulation in a Py-Ag lateral spin valve. *Phys. Rev. Lett.*, 99(19):1–4, 2007.
- [20] O’Brien L., Erickson M.J., Spivak D., Ambaye H., Goyette R.J., Lauter V., Crowell P.A., and Leighton C. Kondo physics in non-local metallic spin transport devices. *Nat. Comm.*, 5(3927):1–9, 2014.

- [21] Maekawa S., Valenzuela S.O., Saitoh E., and Kimura T. *Spin current*. Oxford University Press, 1st edition, 2012 (15-24).
- [22] Coey J.M.D. *Magnetism and magnetic materials*. Cambridge University Press, 1st edition, 2009 (5-6).
- [23] Elliott R.J. Theory of the effect of spin-orbit coupling on magnetic resonance in some semiconductors. *Phys. Rev.*, 96(2):266–279, 1954.
- [24] Jakubovics J.P. *Magnetism and magnetic materials*. CRC Press, 2nd edition, 1994 (1-7).
- [25] Kittel C. *Introduction to solid state physics*. John Wiley & Son, 7th edition, 1996 (297-357).
- [26] Berry M.V. and Geim A.K. Of flying frogs and levitrons. *Euro. Journ. Phys*, 18: 307, 1997.
- [27] Skomski R. *Simple models of magnetism*. Oxford Graduate Texts, 1st edition, 2008 (15-72).
- [28] Stoner E.C. Collective electron ferromagnetism. *Proc. of the royal soc. of London series A*, 165(A922):372–414, 1937.
- [29] Ziman J.M. *Electrons and phonons*. Oxford Classic Texts, 1st edition, 1960 (334-420).
- [30] Kondo J. Resistance minimum in dilute magnetic alloys. *Progress of Theoretical Phys.*, 32(1):37–49, 1964.
- [31] Davies J.H. *The physics of low dimensional semiconductors*. Cambridge University Press, 2012 (290-328).
- [32] Mott N.F. The electrical conductivity of transition metals. *Proc. of the Royal Soc. A*, 153(880):699–717, 1936.
- [33] Baibich M.N., Broto J.M., Fert A., Nguyen van Dau F., Petroff F., Eitenne P., Creuzet G., Friederich A., and Chazelas J. Giant magnetoresistance of (001)Fe/(001)Cr magnetic superlattices. *Phys. Rev. Lett.*, 61(21):2472–2475, 1988.

- [34] Binasch G., Grünberg P., Saurenbach F., and Zinn W. Enhanced magnetoresistance in layered magnetic structures with antiferromagnetic interlayer exchange. *Phys. Rev. B*, 39(7):4828–4830, 1989.
- [35] Valet T. and Fert A. Theory of the perpendicular magnetoresistance in magnetic multilayers. *Phys. Rev. B*, 48(10):7099–7113, 1993.
- [36] Johnson M. and Silsbee R.H. Interfacial charge-spin coupling: injection and detection of spin magnetisation in metals. *Phys. Rev. Lett.*, 55(17):1790–1793, 1985.
- [37] Schrefl T., Fidler J., Kirk K.J., and Chapman J.N. Domain structures and switching mechanisms in patterned magnetic elements. *Journ. of Magnetism and Magnetic Mat.*, 175(1-2):193–204, 1997.
- [38] Yafet Y. g Factors and spin-Lattice relaxation of conduction electrons. *Solid State Phys.*, 14:1–98, 1963.
- [39] Yafet Y. Conduction-electron spin relaxation by transition-element impurities in copper. *Journ. of App. Phys.*, 39(2):853–854, 1968.
- [40] Beuneu F. and Monod P. The Elliot relation in pure metals. *Phys. Rev. B*, 18(6):2422–2425, 1978.
- [41] Monod P. and Schultz S. Conduction electron spin-flip scattering by impurities in copper. *Journ. de Phys.*, 43(2):393–401, 1982.
- [42] Kiss A., Szolnoki L., and Simon F. The Elliott-Yafet theory of spin relaxation generalized for large spin-orbit coupling. *Sci. Rep.*, 6(22706):1–10, 2016.
- [43] Bass J. and Pratt W.P. Spin-diffusion lengths in metals and alloys, and spin-flipping at metal / metal interfaces: An experimentalist’s critical review. *Journ. of Phys.: Condensed Matter*, 19(183201):1–41, 2007.
- [44] Idzuchi H., Fukuma Y., Wang L., and Otani Y. Spin relaxation mechanism in Ag nanowires covered with MgO protection layer. *Phys. Rev. Lett.*, 101(2):1–4, 2011.
- [45] Kojda D., Mitdank R., Handweg M., Mogilatenko A., Albrecht M., Wang Z., Ruhhammer J., Woias M., Kroener P., and Fischer S.F. Temperature dependent thermoelectric properties of individual Ag nanowires. *Phys. Rev. B*, 91(024302):1–13, 2015.

- [46] Bakker F.L., Slachter A., Adam J.P., and van Wees B.J. Interplay of Peltier and Seebeck effects in nanoscale nonlocal spin valves. *Phys. Rev. Lett.*, 105(136601): 1–4, 2010.
- [47] Johnson M. and Silsbee R.H. Calculation of nonlocal baseline resistance in a quasi-one-dimensional wire. *Phys. Rev. B*, 76(153107):1–4, 2007.
- [48] Kasai S., Hirayama S., Takahashi Y.K., Mitani S., Hono K., Adachi H., Ieda J., and Maekawa S. Thermal engineering of non-local resistance in lateral spin valves. *Appl. Phys. Lett.*, 104(162410):1–5, 2014.
- [49] Joule J.P. *The scientific papers of James Prescott Joule*. Cambridge University Press, 2012 (1-50).
- [50] Peltier J.C.A. New experiments on the heat effects of electric currents. *Annales de Chimie et de Phys.*, 56, 1834.
- [51] Fukuma Y., Wang L., Idzuchi H., Takahashi S., Maekawa S., and Otani Y. Giant enhancement of spin accumulation and long-distance spin precession in metallic spin valves. *Nat. Materials*, 10:527–531, 2011.
- [52] Rosamond M.C., Batley J.T., Burnell G., Hickey B.J., and Linfield E.H. High contrast 3D proximity correction for electron-beam lithography: an enabling technique for the fabrication of suspended masks for complete device fabrication within an UHV environment. *Microelectronic Eng.*, 143:5–10, 2015.
- [53] Casanova F., Sharoni A., Erekhinsky M., and Schuller I.K. Control of spin injection by direct current in lateral spin valves. *Phys. Rev. B*, 79(184415):1–6, 2009.
- [54] Brataas A., Bauer G.E.W., and Kelly P.J. Non-collinear magnetoelectronics. *Phys. Reports*, 427(4):157–255, 2006.
- [55] Kimura T., Sato T., and Otani Y. Temperature evolution of spin relaxation in a NiFe/Cu lateral spin valve. *Phys. Rev. Lett.*, 100(6):1–4, 2008.
- [56] Bilotti E., Fenwick O., Schroeder B.C., Baxendale M., Taroni-Junior P., Degousee T., and Liu Z. Organic thermoelectric composites materials. *Comprehensive Composite Mat. II*, 6:408–430, 2018.

- [57] Kockert M., Kojda D., Mitdank R., Mogilatenko A., Wang Z., Ruhhammer J., Kroener M., Woias P., and Fischer S.F. Nanometrology: Absolute Seebeck coefficients of individual Ag nanowires. *Sci. Rep.*, 9(20265):1–10, 2019.
- [58] Mason S.J., Hojem A., Wesenberg D.J., Avery A.D., and Zink B.L. Determining absolute Seebeck coefficients from relative thermopower measurements of thin films and nanostructures. *Journ. App. Phys.*, 127(085101):1–10, 2020.
- [59] Avery A.D., Pufall M.R., and Zink B.L. Determining the planar Nernst effect from magnetic-field-dependent thermopower and resistance in Ni and Py thin films. *Phys. Rev. B*, 86(184408):1–5, 2012.
- [60] Avery A.D., Mason S.J., Bassett D., Wesenberg D., and Zink B.L. Thermal and electrical conductivity of approximately 100-nm Py, Ni, Co, Al, and Cu films and examination of the Wiedemann-Franz law. *Phys. Rev. B*, 92(214410):1–10, 2015.
- [61] Tritt T.M. *Thermal conductivity*. Kluwer, New York, 2004 (21-91).
- [62] Makinson R.E.B. The thermal conductivity of metals. *Math. Proc. Cambridge Phil. Soc.*, 34(474), 1938.
- [63] Cheng Z., Liu L., Xu S., Lu M., and Wang X. Temperature dependence of electrical and thermal conduction in single Ag nanowire. *Nat. Sci. Rep.*, 5(10718):1–12, 2015.
- [64] Lide D.R. *CRC handbook of chemistry and physics*. CRC Press, 84th edition, 2003 (229-240).
- [65] Mihajlovic G., Pearson J.E., Bader S.D., and Hoffmann A. Surface spin flip probability of mesoscopic Ag wires. *Phys. Rev. Lett.*, 104 (237202):1–4, 2010.
- [66] Zou H. and Ji Y. The origin of the high surface spin-flip rate in metallic nonlocal spin valves. *App. Phys. Lett.*, 101(8):1–4, 2012.
- [67] O’Brien L., Spivak D., Jeong J.S., Mkhoyan K.A., Crowell P.A., and Leighton C. Interdiffusion-controlled Kondo suppression of injection efficiency in metallic nonlocal spin valves. *Phys. Rev. B*, 93(1):1–7, 2016.
- [68] Kondo J. *The physics of dilute magnetic alloys*. Cambridge University Press, 2012 (69-119).

- [69] Kim K.W., O'Brien L., Crowell P.A., Leighton C., and Stiles M.D. Theory of Kondo suppression of spin polarization in nonlocal spin valves. *Phys. Rev. B*, 95(10):1–14, 2017.
- [70] Isasa M., Villamor E., Fallarino L., Idigoras O., Suszka A.K., Tollan C., Berger A., Hueso L.E., and Casanova F. Spin transport enhancement by controlling the Ag growth in lateral spin valves. *Journ. Phys. D*, 48(215003):1–4, 2015.
- [71] Umrath W. *Fundamentals of vacuum technology*. Oerlikon Leybold Vacuum, 2007 (56-60).
- [72] Sagasta E., Omori Y., Isasa M., Otani Y., Hueso L.E., and Casanova F. Spin diffusion length of Py using spin absorption in lateral spin valves. *App. Phys. Lett.*, 111(8):1–7, 2017.
- [73] Villamor E.L. *Injection, transport and manipulation of pure spin currents in metallic lateral spin valves*. PhD thesis, University of the Basque Country, 2014.